学位論文（要約）

Direct mass measurements of neutron-rich Ca isotopes
（中性子過剰Ca同位体の直接質量測定）

平成28年12月　博士（理学）申請

東京大学大学院理学系研究科
物理学専攻

小林　幹

Direct mass measurements of neutron-rich Ca isotopes

Doctoral Dissertation

by

Motoki Kobayashi

December, 2016

Department of Physics,
Graduate School of Science,
The University of Tokyo

Abstract

We have performed the first direct mass measurements of neutron-rich calcium isotopes beyond neutron number $N = 34$ at the RIKEN Radioactive Isotope Beam Factory using the time-of-flight magnetic-rigidity (TOF–$B\rho$) technique. The masses of very neutron-rich nuclei in the vicinity of ^{54}Ca have been measured with precisions almost as high as the best previously reached by TOF–$B\rho$ mass spectrometry.

The mass of atomic nuclei is a fundamental quantity as it reflects the sum of all interactions within the nucleus. Changes in the shell structure in nuclei far from stability, called "shell evolution", can be probed by mass measurements. Particularly, the presence of subshell gaps at $N = 32$ and 34 around calcium isotopes has attracted much attention over recent years. Mass measurements of neutron-rich nuclei in the vicinity of $N = 32$ and 34 provide pivotal information for investigating the shell evolution at $N = 32$ and 34.

The masses of 21 nuclei including $^{55–57}$Ca, ^{54}K, and $^{50–52}$Ar were determined for the first time. In addition, the uncertainties of 10 masses were reduced by more than 100 keV. The deduced atomic mass excesses of $^{55–57}$Ca, ^{54}K, and $^{50–52}$Ar are $-18650(160)$ keV, $-13510(250)$ keV, $-7370(990)$ keV, $-5730(400)$ keV, $-13040(120)$ keV, $-6740(280)$ keV, and $-1590(900)$ keV, respectively. The experimental results provide strong evidence for the onset of an appreciable $N = 34$ subshell gap in ^{54}Ca comparable to that for $N = 32$. In contrast, for the argon isotopes, there is no significant increase in the subshell gap at $N = 32$ relative to $N = 30$, and a weakening of the $N = 32$ gap is indicated below the calcium and potassium isotopes.

Contents

1 Introduction **1**

1.1 Nuclear mass . . . 1

1.2 Magic number . . . 1

1.2.1 Shell model . . . 1

1.2.2 Occurrence and disappearance of magic numbers . . . 2

1.3 Overview of direct mass measurements . . . 6

1.3.1 Frequency-based mass spectrometry . . . 6

1.3.2 Time-of-flight mass spectrometry . . . 7

1.3.3 Comparison of the various techniques . . . 8

1.4 Thesis objectives . . . 11

2 Experiment **13**

2.1 Experimental overview . . . 13

2.1.1 Overview of the experimental setup . . . 13

2.1.2 Expected mass uncertainty . . . 14

2.2 Experimental facilities . . . 16

2.2.1 Accelerators . . . 16

2.2.2 BigRIPS fragment separator . . . 16

2.2.3 High-Resolution Beam Line and SHARAQ spectrometer . . . 17

2.3 Ion optics . . . 18

2.4 Detectors . . . 20

2.4.1 Beam-line detectors . . . 20

2.4.2 Gamma-ray detector array . . . 29

2.5 Data acquisition . . . 31

2.5.1 Data acquisition system . . . 31

2.5.2 Triggers . . . 31

2.6 Summary of experimental conditions . . . 32

3 Data analysis **35**

3.1 Particle identification . . . 35

3.1.1 Method of particle identification . . . 35

3.1.2 Confirmation of PID . . . 35

3.1.3 Determination of Z and A/Q . . . 38

3.2 Analysis of beam-line detectors . . . 42

3.2.1 LP-MWDC . . . 42
3.2.2 S0PPAC . . . 48
3.2.3 Diamond detector . . . 49
3.2.4 SSD . . . 55
3.2.5 Plastic scintillator . . . 55
3.3 Mass calibration in ^{55}Ca setting . . . 58
3.3.1 Procedure for mass calibration . . . 58
3.3.2 Reference nuclei . . . 58
3.3.3 Fitting function . . . 62
3.3.4 Correction for time dependence (Step 1 and Step 2) . . . 64
3.3.5 Mass calibration to deduce the final mass values (Step 3) . . . 67
3.3.6 Measurement uncertainty . . . 74
3.4 Mass calibration in ^{52}Ca setting . . . 77
3.4.1 Reference nuclei . . . 77
3.4.2 Mass calibration . . . 77
3.4.3 Measurement uncertainty . . . 80
3.4.4 Consistency between two measurements . . . 80

4 Results **83**
4.1 Mass spectrum . . . 83
4.1.1 PID plot after mass calibration . . . 83
4.1.2 Deduced A/Q spectrum . . . 83
4.1.3 Mass resolution . . . 88
4.2 Atomic mass excess . . . 89
4.2.1 Mass table . . . 89
4.2.2 Contamination of isomeric states . . . 89
4.2.3 Comparison with predicted values in AME2012 . . . 95

5 Discussion **97**
5.1 Two-neutron separation energy . . . 97
5.2 Shell gaps from mass measurements . . . 101
5.2.1 Empirical shell gap . . . 101
5.2.2 Three-point mass difference . . . 104
5.3 Subshell gap at $N = 34$ in Ca and K isotopes . . . 110
5.4 Subshell gap at $N = 32$ in Ar isotopes . . . 111
5.5 Performance of the present mass measurements . . . 111
5.6 Perspectives . . . 112

6 Conclusion **115**

A Time resolution of the TOF measurement system **117**

B Atomic and nuclear masses **119**

C Derivation of the mass fitting functions **121**
C.1 Derivation of Eq. (3.28) 122
C.2 Derivation of Eq. (3.29) 122

D Shape of the mass distribution **127**

E Shift of deduced mass values **131**

F Uncertainties related to the fitting **135**
F.1 Expression of δ_{fit} 135
F.2 Evaluation of δ_{fit} values in the present measurements 137

G Uncertainties related to the Z correction **139**

H A/Q spectrum for each Z **141**

Bibliography **145**

Acknowledgments **157**

List of Figures

1.1 Single particle energies in the shell model. 3
1.2 Two-neutron separation energies S_{2n} for neutron-rich isotopes from neon ($Z = 10$) to nickel ($Z = 28$). 4
1.3 Schematic illustration of changes in the shell structure at $N = 32$ and 34. 5
1.4 Relative mass uncertainty versus isobaric distance from stability ($Z_0 - Z$) for different nuclear mass measurement facilities. 10
1.5 Nuclear chart in the vicinity of neutron-rich Ca isotopes. 11

2.1 Schematic view of the BigRIPS separator, the High-Resolution Beam Line, and the SHARAQ spectrometer. 14
2.2 Overview of the RIBF facility. 16
2.3 Dispersion-matching beam transport from F3 to S2. 18
2.4 Layouts of the beam-line detectors in the F3 and S2 chambers from the top view. 21
2.5 Picture and schematic view of the diamond detector used in the present experiment. 23
2.6 Electronic circuit for the diamond detector. 23
2.7 Electronic circuit for the plastic scintillator. 24
2.8 Schematic view of the LP-MWDC (XUY configuration) [73]. 25
2.9 Electronic circuit for the LP-MWDC. 27
2.10 Schematic view of the PPAC [79]. 27
2.11 Electronic circuit for the PPAC. 28
2.12 Schematic view of the SSD used in the present experiment. 28
2.13 Electronic circuit for the SSD. 28
2.14 Electronic circuit for the γ-ray detector array. 29
2.15 Experimental setup at S2+ [80]. 30
2.16 Experimental setup at S2 and S2+ from the top view [80]. 30
2.17 Schematic diagram of the electronics for the S2 window trigger. 31

3.1 PID plot shown as ΔE in S2Si1 versus TOF(F3–S2) in the ^{55}Ca setting. 36
3.2 PID plot shown as ΔE in S2Si1 versus TOF(F3–S2) in the ^{52}Ca setting. 37
3.3 Energy spectra of delayed γ rays from the prompt γ-ray emission in (a) ^{54}Sc and (b) ^{59}Ti. 37
3.4 Two dimensional plots of Z_{Si} and Z_{Pla} (a) without and (b) with the condition of $Z_{\mathrm{Si}} = Z_{\mathrm{Pla}}$. 39
3.5 PID plot shown as Z versus A/Q in the ^{55}Ca setting. 40

3.6 PID plot shown as Z versus A/Q in the ^{52}Ca setting. 41
3.7 Correlation between the drift time and the pulse width without the PID gate. . . 42
3.8 Correlations between the drift time and the pulse width before and after the correction of the drift time origin. 44
3.9 (a) Distribution of the drift time, (b) distribution of the drift distance, and (c) mapping from the drift time to the drift distance. 45
3.10 Distributions of the uncertainties of the ray parameters for ^{55}Sc. 47
3.11 Spectra of (a) $T_{X_1} + T_{X_2}$ and (b) $T_{Y_1} + T_{Y_2}$ for S0PPAC. 48
3.12 Examples of signals from the strips in the diamond detector. 49
3.13 Time difference $T(\text{StripL}) - T(\text{StripR})$ in a strip in (a) F3Dia and (b) S2Dia. . . 50
3.14 Charge of the signal from a strip in (a) F3Dia and (b) S2Dia. 50
3.15 Correlations between $T(\text{Pad})$ and $T(\text{StripL})$ or $T(\text{StripR})$ in F3Dia (a)(b) without and (c)(d) with the limitation of the time difference $T(\text{StripL}) - T(\text{StripR})$. 52
3.16 ID distributions of the hit strip in (a) F3Dia and (b) S2Dia. 53
3.17 Correlations between the time difference in the strip and the position in (a) F3Dia Strip 4 and (b) S2Dia Strip 2 for ^{54}Ca. 53
3.18 Spectra of the time difference in the strip corrected for the position dependence in (a) F3Dia Strip 4 and (b) S2Dia Strip 2 for ^{54}Ca. 54
3.19 Correlation between the energy loss and time resolution in the diamond detector. 54
3.20 Energy calibration of the SSD. 55
3.21 Correlations between the energy loss in the plastic scintillator (S2Pla) and the beam position at S2 (a) before and (b) after the correction for the position. . . . 56
3.22 Energy calibration of S2Pla. 57
3.23 Map of the nuclei observed in the present measurements in the ^{55}Ca setting in terms of A/Z and Z. 61
3.24 Correlations between a_{F3} and x_{S2} at (a) $z_{\text{S2}} = 0$ and (b) $z_{\text{S2}} = 550$, gated by $|x_{\text{F3}}| < 0.3$. 63
3.25 Shift of the difference between the deduced mass (m_{exp}) and the literature value (m_{ref}) for ^{44}Cl (red), ^{45}Cl (black), and ^{46}Cl (blue), as a function of the experimental run number. 64
3.26 Shift of the difference between the deduced mass (m_{exp}) and the literature value (m_{ref}) for ^{45}Cl as a function of the experimental run number. 65
3.27 Contours of $\Delta t - \Delta t_0$ [ps] calculated with different $B\rho$ and L values around $B\rho_0 = 7.0$ Tm and $L_0 = 104206$ mm. 66
3.28 Correlations between Q in the diamond detectors at F3 and S2 and ΔTOF. . . . 68
3.29 Differences between the mass-to-charge ratios deduced in the mass fitting in which the weight is not taken into account and the literature values. 69
3.30 Differences between the deduced mass-to-charge ratios in the ^{55}Ca setting and the literature values before the correction for the Z dependence as a function of Z. 71
3.31 Differences between the deduced mass-to-charge ratios in the ^{55}Ca setting and the literature values after the correction for the Z dependence as a function of Z. 71

3.32 Differences between the deduced mass-to-charge ratios in the ^{55}Ca setting and the literature values after the correction for the Z dependence as a function of A/Q. 72
3.33 Differences between the deduced masses in the ^{55}Ca setting and the literature values after the correction for the Z dependence as a function of A/Q. 72
3.34 Correlation between the A/Q value deduced from the present experiment in the ^{55}Ca setting and the horizontal position at S0 (x_0) for ^{36}Si. 73
3.35 The same as Fig. 3.34, but for ^{59}Sc. 73
3.36 Map of the nuclei observed in the ^{52}Ca setting in terms of A/Z and Z. 78
3.37 Differences between the deduced mass-to-charge ratios in the ^{52}Ca setting and the literature values after the correction for the Z dependence as a function of A/Q. 79
3.38 Differences between the deduced masses in the ^{52}Ca setting and the literature values after the correction for the Z dependence as a function of A/Q. 79
3.39 Differences of the deduced masses in the ^{52}Ca setting to those in the ^{55}Ca setting for ^{55}Sc, ^{58}Ti, ^{59}Ti, and ^{62}V. 81

4.1 PID plot shown as Z versus A/Q deduced from the experiment in the ^{55}Ca setting. 84
4.2 The same as Fig. 4.1, but for in the ^{52}Ca setting. 85
4.3 A/Q spectrum deduced from the present experiment in the ^{55}Ca setting. 86
4.4 A/Q spectrum deduced from the present experiment in the ^{52}Ca setting. 87
4.5 A/Q spectrum deduced from the present experiment in the ^{55}Ca setting for $Z = 20$ (Ca) isotopes. 87
4.6 A/Q spectrum for ^{55}Ca. 88
4.7 Comparisons of the new mass values obtained in the present experiment to the predicted masses tabulated in AME2012 [65]. 96

5.1 The two-neutron separation energies S_{2n} plotted for neutron numbers $N = 27$–41 from P ($Z = 15$) to V ($Z = 23$) isotopes. 98
5.2 The two-neutron separation energies S_{2n} for (a) Ca, (b) K, and (c) Ar isotopes as a function of neutron number. 100
5.3 The empirical shell gaps Δ_N for the (a) Ca, (b) K, and (c) Ar isotopes as a function of neutron number. 102
5.4 Naive pictures of the nuclei used for the calculation of the empirical shell gap $\Delta_N(A, Z)$ at (a) even-N and (b) odd-N. 103
5.5 The three-point mass differences $\Delta_3(N)$ for the (a) Ca, (b) K, and (c) Ar isotopes as a function of neutron number. 105
5.6 Naive picture of the nuclei used for the calculation of $\Delta_3(N)$ at (a) odd-N and (b) even-N. 107
5.7 The shell gaps $\delta e^-(N) \equiv 2(\Delta_3(N) - \Delta_3(N-1))$ for the (a) Ca, (b) K, and (c) Ar isotopes as a function of neutron number. 108
5.8 The shell gap $\delta e^-(N) \equiv 2(\Delta_3(N) - \Delta_3(N-1))$ at $N = 34$ as a function of proton number Z. 109

5.9 The shell gap $\delta e^{-}(N) \equiv 2(\Delta_3(N) - \Delta_3(N-1))$ at $N = 32$ as a function of proton number Z. 109
5.10 Relative mass uncertainty versus isobaric distance from stability for different nuclear mass measurement facilities together with the new results from the present mass measurements. 112

A.1 Measured time resolution of the TOF measurement system versus length of the optical fiber. 118

B.1 Total electron binding energy B_e as a function of proton number Z. 120

D.1 Distributions of the probability density functions $f_1(x)$ (black), $f_2(x)$ (red), $f_3(x)$ (green), and $f_4(x)$ (blue) with $\mu = 1.0$ and $\sigma = 0.1$. 129

E.1 Shift of the TOF values for ^{45}Cl as a function of the run number in the experiment. 132
E.2 Temperature change in the SHARAQ DAQ area as a function of the run number in the experiment. 132
E.3 Change of the magnetic field at SD2. 133

F.1 Evaluated δ_{fit} values as a function of A/Q. 137

H.1 A/Q spectrum deduced from the present experiment in the ^{55}Ca setting from $Z = 20$ (Ca) to $Z = 23$ (V) isotopes. 141
H.2 The same as Fig. H.1, but from $Z = 14$ (Si) to $Z = 19$ (K) isotopes. 142
H.3 A/Q spectrum deduced from the present experiment in the ^{52}Ca setting from $Z = 20$ (Ca) to $Z = 23$ (V) isotopes. 143
H.4 The same as Fig. H.3, but from $Z = 20$ (Ca) to $Z = 23$ (V) isotopes. 144

List of Tables

1.1 Relative mass uncertainties $\delta m/m$ required to investigate the physical topics [62]. 9

2.1 Expected mass uncertainties for different numbers of events. 15
2.2 Ion-optical design of the HRB in the dispersion-matching mode. 17
2.3 Specifications of the SHARAQ spectrometer. 17
2.4 Transfer matrix of the SHARAQ spectrometer from S0 to S2. 19
2.5 Transfer matrix of the beam line from F3 to S0. 20
2.6 Transfer matrix of the whole system from F3 to S2. 20
2.7 List of the beam-line detectors used in the present experiment. 20
2.8 Comparison of diamond and silicon properties. 22
2.9 Readouts in the diamond detectors and used preamplifiers. 24
2.10 Specifications of the LP-MWDCs used in the present experiment. 26
2.11 List of the data sets stored in the present experiment. 32
2.12 Summary of the experimental conditions. 33

3.1 Known γ-ray energies from the isomeric states in ^{54}Sc and ^{59}Ti. 38
3.2 Position and angular resolutions in the LP-MWDCs at F3 and S2 for the nuclei ranging from $Z = 16$ to $Z = 23$. 47
3.3 List of atomic mass excesses (AME) of the reference nuclei in the ^{55}Ca setting. . 59
3.4 List of the known isomeric states in the region covered by the present mass measurements. Values are taken from the compilation in Ref. [87]. 60
3.5 Data sets of the reference nuclei in the ^{55}Ca setting. 60
3.6 Standard deviation (StdDev) of the deduced mass distribution for each reference nuclide obtained by the fitting in which weight is not considered. 70
3.7 Uncertainties of the masses deduced from the present experiment in the ^{55}Ca setting for the reference nuclei. 75
3.8 Uncertainties of the masses deduced from the present experiment in the ^{55}Ca setting for the nuclei that were not used for the mass calibration. 76
3.9 List of atomic mass excesses (AME) of the reference nuclei in the ^{52}Ca setting. . 77
3.10 Data set of the reference nuclei for the mass calibration in the ^{52}Ca setting. . . . 78
3.11 Uncertainties of the masses deduced from the present experiment in the ^{52}Ca setting for the reference nuclei. 80
3.12 Uncertainties of the masses deduced from the present experiment in the ^{52}Ca setting for the nuclei that were not used for the mass calibration. 80

4.1 Number of the observed nuclides that were not used for the mass calibration in the ^{55}Ca setting. 84
4.2 Number of the observed nuclides that were not used for the mass calibration in the ^{52}Ca setting. 85
4.3 Atomic mass excesses (in keV) obtained in the present experiment. 91
4.4 Adopted atomic mass excesses (in keV) in the present work 93
4.5 Comparisons of the new atomic mass excess values (in keV) obtained in the present experiment to the predicted masses tabulated in AME2012 [65]. 95

G.1 Uncertainties originating from the Z correction for each Z number in the ^{55}Ca setting. 140
G.2 Uncertainties originating from the Z correction for each Z number in the ^{52}Ca setting. 140

Chapter 1

Introduction

1.1 Nuclear mass

The mass of an atomic nucleus is a fundamental quantity as it reflects the sum of all interactions within this quantum many-body system comprised of two kinds of fermions, protons and neutrons. The importance of the mass in nature is expressed in Albert Einstein's famous energy-mass relation [1], $E = mc^2$, which states that energy is equivalent to mass. The mass of an atomic nucleus is less than the sum of the individual masses of its constituent free nucleons, and this missing mass is known as the mass defect, which was discovered by F. W. Aston by means of his mass spectrograph [2]. The energy required to disassemble an atomic nucleus into its constituent protons and neutrons is called as the binding energy, which is expressed by

$$B(Z, N) = Zm_H c^2 + Nm_n c^2 - M(Z, N)c^2, \tag{1.1}$$

where m_H and m_n are the masses of the hydrogen and the neutron, respectively, and $M(Z, N)$ is the atomic mass of a nuclide with proton number Z and neutron number N. The binding energy is responsible for the stability of the nucleus. Thus, measurements of nuclear masses provide fundamental information on nuclear stability.

1.2 Magic number

1.2.1 Shell model

In 1933, from the ensemble of masses obtained by Aston, W. Elsasser discovered the existence of "special numbers" of neutrons and protons at which the corresponding nuclei form particularly stable configurations [3]. This is the early idea of what are usually called "magic numbers". Later, in 1948, the study of nuclear shell structure regained interest through Maria Göppert-Mayer's review in which she examined available experimental facts and pointed to particular stability of shells at numbers 20, 50, 82 and 126 [4]. However, the numbers 50, 82, and 126 could not be explained from solutions of simple potential wells. Finally, in 1949, the observed shell gaps, or so-called nuclear "magic numbers", were reproduced by introducing a strong spin-orbit interaction by Mayer [5], and independently by Haxel, Suess, and Jensen [6]. The conventional

magic numbers for nuclei are 2, 8, 20, 28, 50, 82, and 126.

The nuclear shell model is an analogue of the atomic shell model describing the arrangement of electrons around the nucleus of an atom, in which the closure of an electron shell is marked by the occurrence of a noble-gas atom. The basic idea of the nuclear shell (or independent-particle) model is that individual nucleons move in a mean field with no interactions with other nucleons. The proposed spherical mean field consists of an isotropic harmonic oscillator potential, an orbit-orbit term, and a strongly attractive spin-orbit term. A single particle orbital is characterized by the quantum numbers N, l, and j, which are the major quantum number, orbital angular momentum, and total angular momentum, respectively, and is denoted by the notation Nl_j. Figure 1.1 shows single particle energies in the shell model. The energy levels with and without a spin-orbit potential are shown in the right and left, respectively. As seen in Fig. 1.1, the spin-orbit potential lowers the energies of the $j = l + 1/2$ orbits, and gives rise to the nuclear magic numbers (2, 8, 20, 28, 50, 82, and 126).

Experimentally, several quantities are measured as a signature for a shell closure. One important observable is the energy of the first 2^+ excited state $[E(2_1^+)]$ in even-even nuclei. A high $E(2_1^+)$ value is associated with a particularly stable configuration of the ground state. Evidence for a shell closure is also provided by measurements of the reduced transition probability between the ground state and the 2_1^+ state $[B(E2)]$ in even-even systems. A small $B(E2)$ value indicates a near spherical nucleus, while a large $B(E2)$ corresponds to a deformed nucleus. Thus, nuclei with a closed-shell configuration have a small $B(E2)$ value. Besides these observables reflecting the nuclear quadrupole collectivity, mass differences are employed as a signature for the presence of a shell gap, as the closed-shell nuclei with enhanced stability have more binding energies. In particular, the two-neutron separation energy

$$S_{2n}(Z, N) = B(Z, N) - B(Z, N - 2), \tag{1.2}$$

which is the required energy to remove two neutrons from a nucleus, is often used. Figure 1.2 shows the systematics of the two-neuron separation energies for neutron-rich isotopes from neon ($Z = 10$) to nickel ($Z = 28$). One can see some kinks at $N = 20$ and 28 in Fig. 1.2. A sudden decrease in the two-neutron separation energies indicates the existence of a shell gap.

1.2.2 Occurrence and disappearance of magic numbers

The robustness of the traditional magic numbers suggested by Mayer and Jensen ($N, Z = 2$, 8, 20, 28, 50, 82, and 126) has been well demonstrated for stable nuclei, which are on or near the β-stability line in the nuclear chart. During the last three decades, the exotic nuclei far from the valley of stability towards the limit of existence have been explored with the advent of radioactive isotope (RI) beam facilities. Changes in the shell structure far away from stability, often called "shell evolution", have been intensively investigated in the fields of experimental and theoretical nuclear physics. In exotic nuclei far from the β-stability, some of the traditional magic numbers disappear, while other new ones arise [7, 8]. For instance, the weakening of the conventional magic numbers was observed at $N = 8$ in ^{12}Be [9–12], $N = 20$ in ^{32}Mg [13], which lies inside a region of deformed nuclei commonly referred to as the "island of inversion" [14],

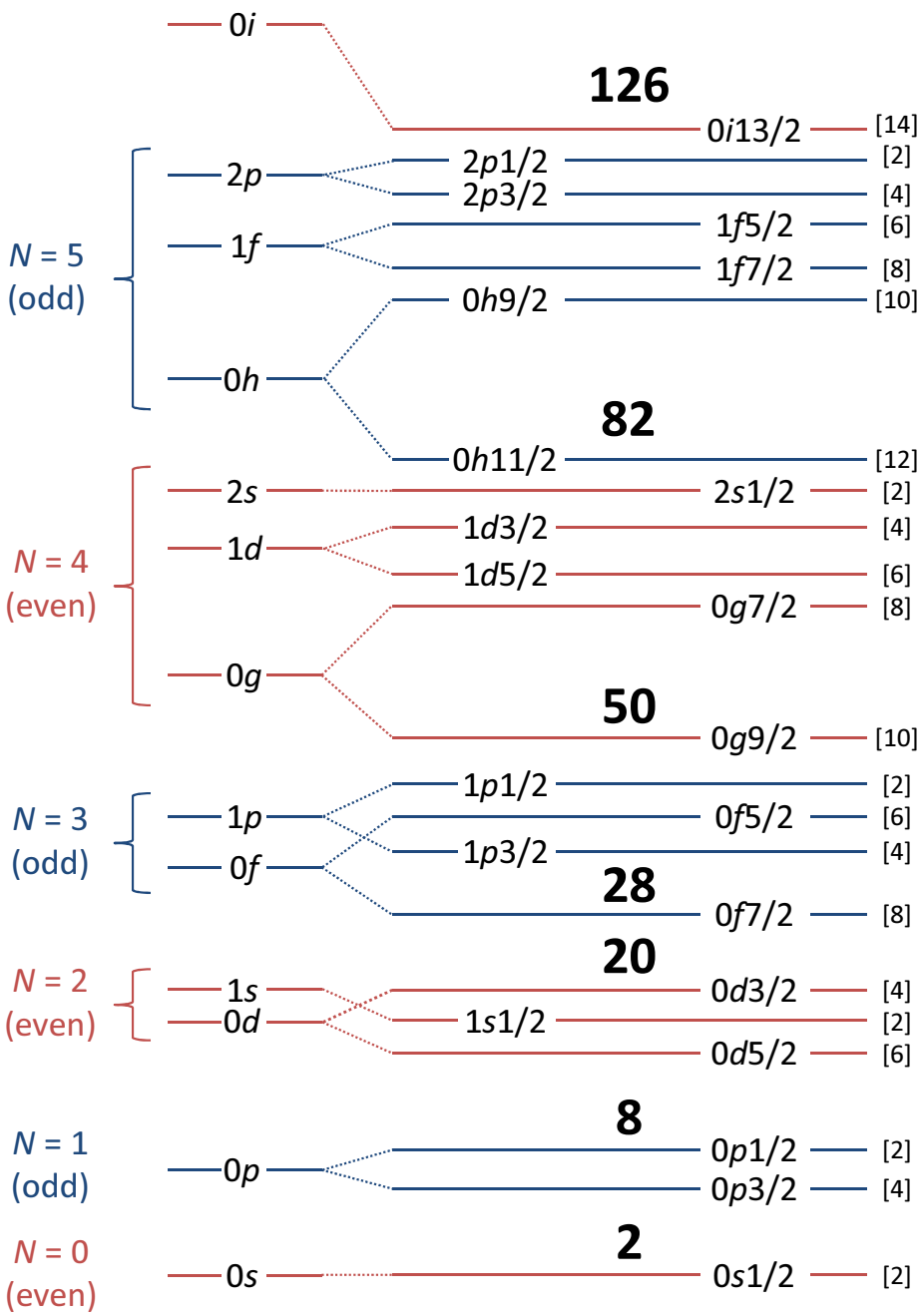

Figure 1.1: Single particle energies in the shell model. The number in a bracket denotes the maximum occupation for a given orbital. The magic numbers are shown in bold.

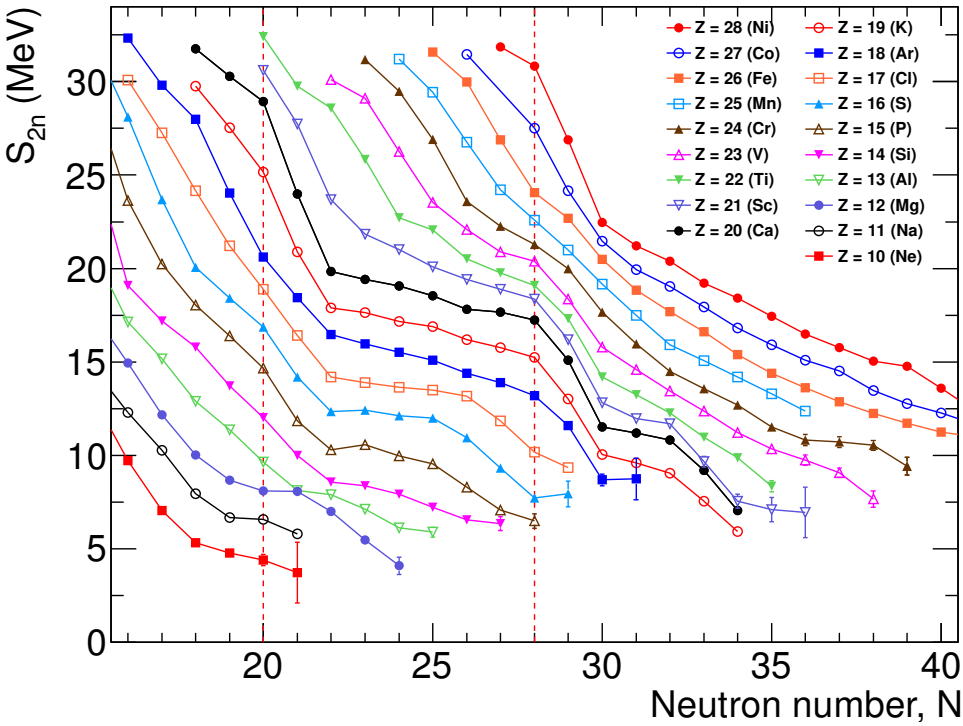

Figure 1.2: Two-neutron separation energies S_{2n} for neutron-rich isotopes from neon ($Z = 10$) to nickel ($Z = 28$). Dashed lines indicate the magic numbers $N = 20$ and 28.

and $N = 28$ in the well-deformed nucleus ^{42}Si [15, 16]. In contrast, the emergence of a new magic number $N = 16$ was observed in exotic oxygen isotopes [17, 18]. For the proton shells, the breakdown of the shell closure at $Z = 8$ was reported in the proton-rich unbound nucleus ^{12}O, which is the mirror nucleus of ^{12}Be [19]. This demonstrated the persistence of mirror symmetry in the shell quenching at the magic number 8.

The shell evolution in neutron-rich nuclei in the pf shell ($1p_{1/2}$, $1p_{3/2}$, $0f_{5/2}$, and $0f_{7/2}$) has attracted much attention over recent years. A subshell closure at $N = 32$ was confirmed in ^{52}Ca [20, 21], ^{54}Ti [22, 23], and ^{56}Cr [24, 25] by measurements of $E(2_1^+)$ or $B(E2)$. The observations for ^{52}Ca were complemented by high-precision Penning-trap mass measurements on ^{51,52}Ca using the TITAN system at TRIUMF, which revealed a flat behavior of S_{2n} in the Ca isotopic chain from $N = 30$ to $N = 32$ [26]. The ^{51}K mass was also measured for the first time in the same high-precision mass measurements, in which the similar flat behavior was observed for the K chain. Recently, the masses of exotic isotopes ^{53,54}Ca were measured for the first time using the multiple-reflection time-of-flight (MR-TOF) device at ISOLTRAP at the ISOLDE/CERN facility [27]. This high-precision mass measurement confirmed the presence of a subshell gap at $N = 32$ in ^{52}Ca. Furthermore, similar mass measurements of ^{52,53}K at ISOLTRAP revealed a sizable shell gap slightly lower than for ^{52}Ca, showing that there exists the $N = 32$ subshell gap below the proton magic number $Z = 20$ [28]. For argon isotopes, the recent measurement of $E(2_1^+)$ in ^{50}Ar at RIBF/RIKEN suggested the $N = 32$ subshell gap in ^{50}Ar similar in magnitude to those in ^{52}Ca and ^{54}Ti [29].

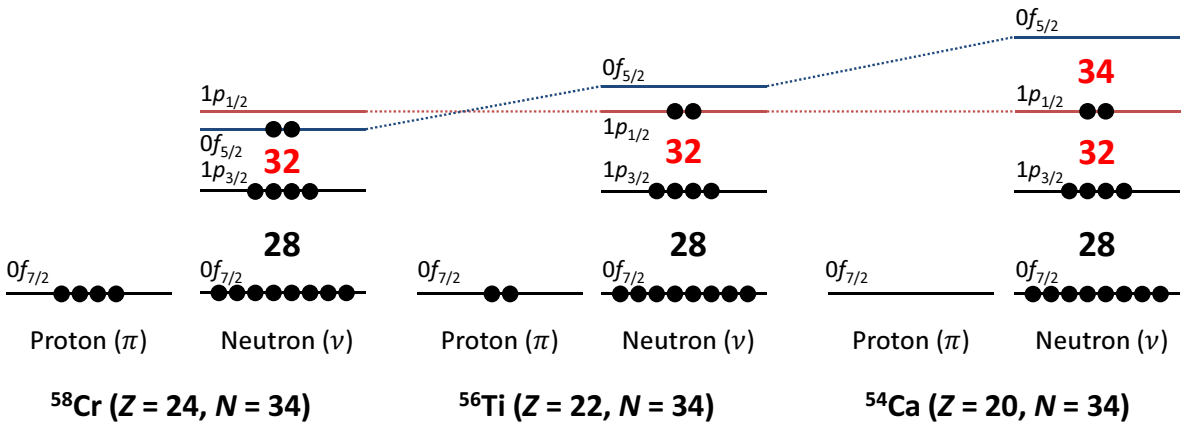

Figure 1.3: Schematic illustration of changes in the shell structure at $N = 32$ and 34.

As well as the $N = 32$ subshell closure, the presence of a large subshell gap at $N = 34$ between the $1p_{1/2}$ and $0f_{5/2}$ neutron orbits in the neutron-rich Ti and Ca isotopes was theoretically predicted [30, 31]. However, no $N = 34$ subshell closure was reported in the measurements on ^{56}Ti [23, 32] and ^{58}Cr [24, 25]. Some doubts regarding the $N = 34$ subshell closure in calcium were raised [33–35], and different theoretical predictions were made. Recently, the measurement of $E(2_1^+)$ in ^{54}Ca at RIBF/RIKEN suggested the possible onset of a sizable subshell closure at $N = 34$ [36]. For establishment of existence of the subshell gap at $N = 34$, mass measurements on the exotic Ca isotopes beyond $N = 34$ are essential.

The shell evolution has been under intensive theoretical studies on the basis of the general properties of nuclear forces, such as tensor interactions and three-body forces. The tensor interactions play a significant role in describing several experimental observations [37]. In the framework of tensor-force-driven shell evolution, the appearance of the new subshell gaps at $N = 32$ and 34 is accounted for as follows. Figure 1.3 shows a schematic illustration of changes in the shell structure at $N = 32$ and 34. As protons are removed from $\pi 0f_{7/2}$, the strength of the attractive nucleon-nucleon interaction between $\pi 0f_{7/2}$ and $\nu 0f_{5/2}$ decreases, resulting in the upward shift of $\nu 0f_{5/2}$ in energy with respect to the $\nu 1p_{1/2}$–$\nu 1p_{3/2}$ spin-orbit partners. Consequently, the drastic change in the spin-orbit splitting caused by the π–ν tensor force gives rise to the sizable gaps at $N = 32$ and 34, as the number of protons in $\pi 0f_{7/2}$ is reduced to $Z = 20$ (Ca). Three-body forces are also important in calculations of very neutron-rich systems based on nuclear forces [38, 39]. Recently, calculations with the three-body forces have been carried out for the Ca isotopes, which is the heaviest chain for such calculations (for example, Refs. [40, 41]). The $N = 28$ standard magic number in ^{48}Ca can be reproduced in microscopic theories by introducing the three-body forces [42]. The importance of the three-body forces has been discussed in the recent mass measurements on ^{51,52}Ca [26] and ^{53,54}Ca [27].

1.3 Overview of direct mass measurements

Since the discovery of two isotopes of neon by J. J. Thomson in 1913 with his famous positive-ray parabola apparatus [43], mass spectroscopy has been developed up to the present. There is a wide range of mass measurement techniques applied worldwide. In this section, an overview of various mass measurement methods for unstable nuclei is provided.

Mass measurements consist of two types of methods: direct and indirect measurements. In the direct methods, which include those based on Penning traps and storage rings, unknown masses are directly determined by calibrators with well-known masses. On the other hand, in the indirect methods, unknown masses are indirectly calculated by means of mass differences obtained as Q values from nuclear decays or reactions.

The experimental methods of the direct mass measurements of exotic nuclei can be divided into two groups: frequency-based mass spectrometry and time-of-flight (TOF) mass spectrometry. Various techniques of the direct mass measurements and the experimental facilities in operation are summarized as follows:

Frequency-based mass spectrometry:

- Penning trap: ISOLTRAP (ISOLDE) [44], LEBIT (NSCL) [45], JYFLTRAP (JYFL) [46], CPT (ANL) [47], SHITRAP (GSI) [48], TITAN (TRIUMF) [49]
- Storage ring: ESR (GSI) [50]

Time-of-flight mass spectrometry:

- Single turn: SPEG (GANIL) [51], TOF (NSCL) [52]
- Multi turn:
  - Storage ring: ESR (GSI) [50], CSRe (IMP) [53], Rare-RI ring (RIKEN) [54]
  - MR-TOF (ISOLDE [55], GSI [56], RIKEN [57])

We give a short overview of the various direct mass measurement techniques in the following.

1.3.1 Frequency-based mass spectrometry

Penning-trap mass spectrometry

Penning-trap mass spectrometry [58] has an unmatched resolving power and precision, and is the most widely used technique for measuring masses of unstable nuclei. Ions are inserted into a trap at low velocities with the isotope separation on-line (ISOL) method. The Penning trap is commonly carried out by the time-of-flight ion-cyclotron-resonance (TOF-ICR) method, in which the ionic motion for ions with a mass-to-charge ratio m/q is excited by applying the radio-frequency quadrupolar field at the cyclotron frequency

$$f_c = \frac{1}{2\pi}\frac{q}{m}B, \tag{1.3}$$

where B is the magnetic field strength. The resonant frequency is converted into a mass of the ion of interest trapped in a volume of $\sim$1 cm^3 by comparison with the resonant frequency of an

atom or atomic cluster with known mass. Accessible half-lives of exotic nuclei to be studied are typically more than a few hundred milliseconds. The limit can be down to on the order of 10 ms only for some gases and alkaline elements [59]. Typically, a relative precision of $\delta m/m \sim 10^{-7}$ can be achieved with more than a hundred ions [58].

Schottky mass spectrometry

The complementary devices for high-precision mass spectrometry to the Penning traps are the storage rings. In the storage-ring mass spectrometry, the relative difference in revolution frequencies $\Delta f/f$ is expressed as

$$\frac{\Delta f}{f} = -\frac{1}{\gamma_T^2}\frac{\Delta(m/q)}{m/q} + \left(1 - \frac{\gamma^2}{\gamma_T^2}\right)\frac{\Delta v}{v}. \tag{1.4}$$

Here, $\Delta(m/q)/(m/q)$ is the relative difference between the mass-to-charge ratios of two ion species, $\Delta v/v$ is that between the velocities, $\gamma = 1/\sqrt{1-(v/c)^2}$ is the Lorentz factor, and γ_T^2 is the so-called transition point given by

$$\gamma_T^2 = \frac{\delta(p/q)/(p/q)}{\delta C/C}, \tag{1.5}$$

where p/q is the magnetic rigidity, and C is the orbit circumference. To eliminate the second term in Eq. (1.4), which is dependent on the velocity spread, two techniques have been developed: Schottky mass spectrometry (SMS) based on frequency measurement and isochronous mass spectrometry (IMS) based on time-of-flight measurement.

In SMS, an electron cooler is used to reduce the velocity spread ($\Delta v/v \to 0$). The revolution frequencies are measured by detecting the induced image currents of the circulating ions on a non-destructive Schottky probe, and the masses of the nuclei of interest are determined from Eq. (1.4) by comparing their Schottky peak positions to those of the well-known masses. Since the electron cooling process takes a few seconds, SMS can measure only the long-lived exotic nuclei with half-lives of $T_{1/2} \gtrsim 10$ s. A recent SMS experiment achieved the mass precision of $\delta m/m = 6 \times 10^{-7}$ [60].

1.3.2 Time-of-flight mass spectrometry

TOF–$B\rho$ mass spectrometry

TOF–$B\rho$ mass spectrometry (TOF-MS) is the focus of this thesis. This technique requires a precise measurement of the time-of-flight and the magnetic rigidity of the ion. The flight length is 116 m and 59 m for the GANIL and NSCL setups, respectively. The mass-to-charge ratio m/q of the ion is derived from the equation of motion:

$$\frac{m}{q} = \frac{B\rho}{\gamma L/t}, \tag{1.6}$$

where $B\rho$ is the magnetic rigidity, L is the flight length, t is the time-of-flight, and γ is the Lorentz factor. The time-of-flight of a fragment, typically of the order of 1 μs, is measured

by two fast-timing detectors, and its typical resolution was $\delta t/t \sim 2 \times 10^{-4}$ in the previous measurements at SPEG/GANIL [51]. The magnetic rigidity is measured by detecting the position of each ion at a large dispersive focus, and the achieved momentum resolution has been commonly $\delta B\rho/B\rho \sim 10^{-4}$ [51].

TOF-MS offers an advantage that it can provide the masses of a large number of isotopes in a single measurement, which allows to map a wide region of the nuclear mass surface. Thus, TOF-MS enables us to study the systematic trends in the mass surface. Another distinct advantage is its short measurement time, which is on the order of 1 μs. Owing to this, TOF-MS can access the short-lived nuclei very far from the β-stability. However, a mass resolution in TOF-MS is limited compared with other techniques such as Penning-trap and storage-ring mass spectrometry, and the mass resolution of $\sigma_m/m = 2\text{–}4 \times 10^{-4}$ has been obtained. The final mass uncertainty is determined by the number of detected ions, and it is typically ∼100 keV (∼1 MeV) for thousands (tens) of events. The achievable relative mass precision is $\delta m/m \sim 10^{-5}$.

Isochronous mass spectrometry

In the storage-ring mass spectrometry, the other complementary technique to SMS is the isochronous mass spectrometry (IMS). In IMS, the velocity dependent term in Eq. (1.4) is minimized by the isochronous mode operation where the condition of $\gamma_T = \gamma$ is achieved. The different velocities of the circulating ions are compensated by the lengths of the orbits, and all ions in a given nuclide have the same revolution frequency. The masses of the nuclides of interest are determined by directly measuring the flight time in the ring with fast-timing time-pickup detectors. IMS can access the short-lived fragments with a half-life as short as a few ten microseconds because no cooling is required unlike SMS. A recent IMS experiment achieved the mass precision of $\delta m/m = 5 \times 10^{-6}$ [61].

MR-TOF mass spectrometry

Multiple-reflection time-of-flight (MR-TOF) mass spectrometry (MR-TOF-MS) is a new approach to high-precision mass measurements of exotic nuclei, and the MR-TOF devices have been commissioned at several facilities in the last few years [55–57]. In MR-TOF-MS, the ions flight in a device many times by electrostatic ion mirrors, and the flight path is extended by several orders of magnitude over the conventional TOF mass spectrometers. MR-TOF-MS has a high resolution, which is orders of magnitude larger than the resolving power achievable in the conventional single-pass TOF mass spectrometry, while retaining its advantages. MR-TOF-MS can access the short-lived nuclei with half-lives of several milliseconds, and has achieved a mass resolution of $\sigma_m/m = 1.7 \times 10^{-6}$ and a relative mass precision of $\delta m/m \sim 10^{-7}$ [56].

1.3.3 Comparison of the various techniques

The required mass precision depends on the investigated physics. Table 1.1 summarizes the precisions and the associated physics that can be probed [62]. For the discussion of the shell effects, which are typically of the order of a few MeV, a mass precision of 10^{-5} is required. To investigate the shell openings and closures in exotic nuclei, a mass precision of 10^{-6} is needed.

Table 1.1: Relative mass uncertainties $\delta m/m$ required to investigate the physical topics [62].

Relative precisions	Physics investigated
10^{-5}	astrophysics, shells
10^{-6}	subshells, pairing
10^{-7}	pairing, halos
10^{-8}	weak interaction

These effects can be discussed using the TOF mass measurement technique with the almost highest precision ever achieved.

To compare the performance of the various mass measurement techniques, we employ the two-dimensional plot of the experimental mass uncertainty and the isobaric distance from stability [62]. The isobaric distance from stability represents the distance between the measured nuclide with Z protons and $(A - Z)$ neutrons and the nuclide in the β-stability with the same mass number. Thus, it is a measure of difficulty to access the nucleus. The isobaric distance from stability is defined by $Z_0 - Z$, where Z_0, the proton number of the most stable isotope in the isobaric chain with mass number A, is given by

$$Z_0 = \frac{A}{1.98 + 0.0155A^{2/3}}. \tag{1.7}$$

Figure 1.4 shows the plot of the relative mass uncertainty and the isobaric distance from stability for the mass measurements of $Z < 28$ nuclei. One can see that TOF mass measurements (SPEG, NSCL, and TOFI) can access more neutron-rich region with moderate uncertainties relative to other mass measurements with traps. For the most exotic nuclides, the TOF approach is the only direct method to progress towards the drip line and investigate the more exotic shell effects.

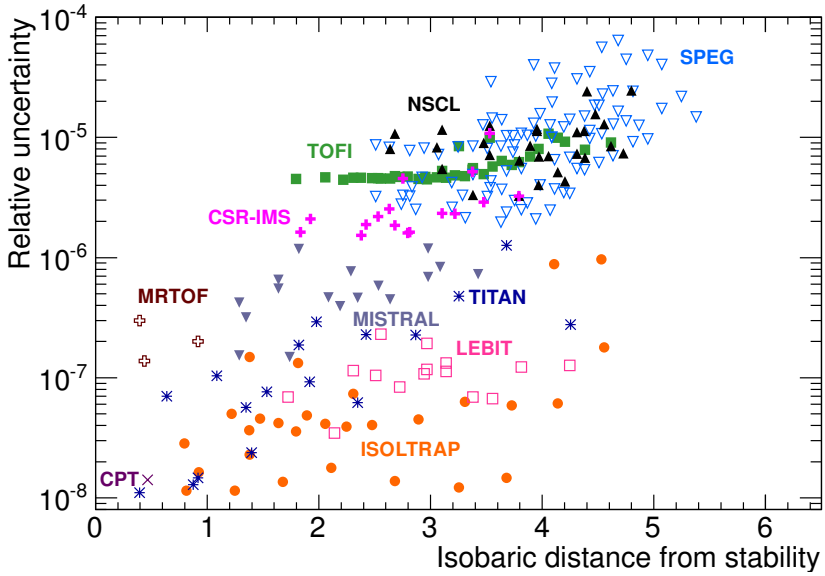

Figure 1.4: Relative mass uncertainty versus isobaric distance from stability ($Z_0 - Z$) for different nuclear mass measurement facilities. Only the mass measurements of the nuclei of $Z < 28$ are plotted. Experimental facilities that are not mentioned in the text are included in this figure: TOFI, which was in operation from 1987 to 1998, is a single-pass TOF method at Los Alamos National Laboratory [63]. MISTRAL, which is one of the frequency-based facilities, is the radio-frequency (RF) transmission spectrometer at ISOLDE [64].

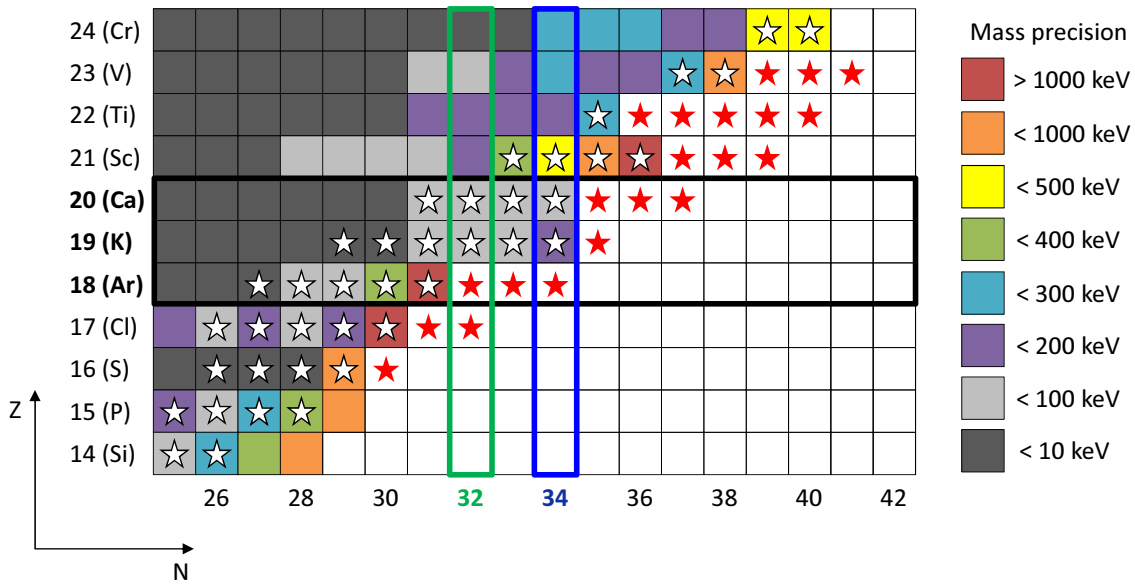

Figure 1.5: Nuclear chart in the vicinity of neutron-rich Ca isotopes. Filled colors show the mass uncertainties in the literature. Stars represent the nuclei whose masses are measured in the present experiment. Filled red stars indicate the nuclei with unknown masses. Mass uncertainties are taken from the AME2012 database [65] except for ^{64}Cr [66], ^{56,57}Sc [67], ^{53,54}Ca [27], ^{52,53}K [28], ^{48}Ar [68], and ^{47}Cl [69].

1.4 Thesis objectives

In this thesis, we present the first direct mass measurements of neutron-rich isotopes in the vicinity of calcium, including $^{55-57}$Ca, ^{55}K, and $^{50-52}$Ar, by the TOF–$B\rho$ technique. Figure 1.5 shows the nuclear chart near the neutron-rich Ca isotopes. Stars represent the nuclei observed in the present experiment, and filled red stars indicate the nuclei whose masses are measured for the first time. Mass measurements of neutron-rich nuclei in the region near $N = 32$ and 34 provide direct and pivotal information for discussing the shell evolution at $N = 32$ and 34. The purpose of the present work is to investigate the presence of the subshell gaps at $N = 34$ in the Ca and K isotopes, and at $N = 32$ in the Ar isotopes, through mass measurements with uncertainties of a few hundred keV.

Mass measurements of the nuclei far from stability are challenging due to the low production yields and the short half-lives. In the present work, we have developed the TOF–$B\rho$ mass measurement technique at the RIKEN Radioactive Ion Beam Factory (RIBF) to measure the masses of exotic nuclei at once. The masses of the nuclei of interest in the present work can be measured only by the TOF–$B\rho$ mass technique as they are very short-lived: For instance, the half-lives of $^{55-57}$Ca, ^{55}K, and $^{50-52}$Ar are 22 ms, 11 ms, >620 ns, >360 ns, 85 ms, >200 ns, and >620 ns, respectively, which are taken from the NNDC database [70]. The mass measurements were performed at RIBF using the high-resolution spectrometer SHARAQ. The TOF of ions was measured by the newly developed diamond detectors with outstanding time resolutions. The dispersion-matched operation of SHARAQ allowed the high-precision measurements of the beam momenta.

The author joined entire preparation and experiment, and was responsible for the analysis of the data. In particular, the author played a central role in preparing and operating the diamond detector, which is one of the most important detectors for the present mass measurements. The author also made a large contribution to preparing other beam-line detectors, such as the low-pressure multi-wire drift chambers and the silicon strip detectors.

The thesis is organized as follows: In Chapter 2, the details on the experimental setup are described. In Chapter 3, the procedure of the data analysis is explained in detail. In Chapter 4, the experimental results, including the deduced mass values, are provided. In Chapter 5, discussions from the obtained results are given. Finally, the conclusion of the thesis is presented in Chapter 6.

Chapter 2

Experiment

The experiment was performed at the Radioactive Isotope Beam Factory (RIBF) at RIKEN [71], which is operated by RIKEN Nishina Center and Center for Nuclear Study, University of Tokyo. This is the first in-flight mass measurement using the TOF–$B\rho$ technique in RIBF. Owing to the high yields of unstable isotopes available at RIBF, masses of very exotic nuclei far from stability can be studied.

This chapter describes the setup in the present experiment in detail. First, Sec. 2.1 presents an overview of the present TOF mass measurements. Sec. 2.2 describes the experimental facilities. Sec. 2.3 explains the ion optics in the experiment. Sec. 2.4 gives the detailed descriptions of the detectors used in the experiment. Sec. 2.5 explains the data acquisition system in the present experiment. Finally, Sec. 2.6 summarizes the experimental conditions.

2.1 Experimental overview

In this section, an overview of the present TOF mass measurements is described. First, a brief overview of the experimental setup is given. Details of the setup are explained in the following sections. Subsequently, the expected mass resolution and uncertainty in the present mass measurements are discussed.

2.1.1 Overview of the experimental setup

Masses were measured directly by the TOF–$B\rho$ technique, which was introduced in Sec. 1.3.2. Neutron-rich isotopes including the nuclei of interest in the vicinity of ^{54}Ca were produced by fragmentation of a ^{70}Zn primary beam at 345 MeV/u. The fragments were transported in the BigRIPS separator (Sec. 2.2.2) and the High-Resolution Beam Line to the SHARAQ spectrometer (Sec. 2.2.3). Figure 2.1 shows a schematic view of the beam line to SHARAQ in RIBF.

The TOF was measured using a pair of newly developed diamond detectors placed at an achromatic focus of BigRIPS (F3) and the final focal plane of SHARAQ (S2). The flight path length between the two diamond detectors is ∼105 m along the central trajectory, which corresponds to the TOF of ∼540 ns. The magnetic rigidity $B\rho$ was measured by a parallel-plate

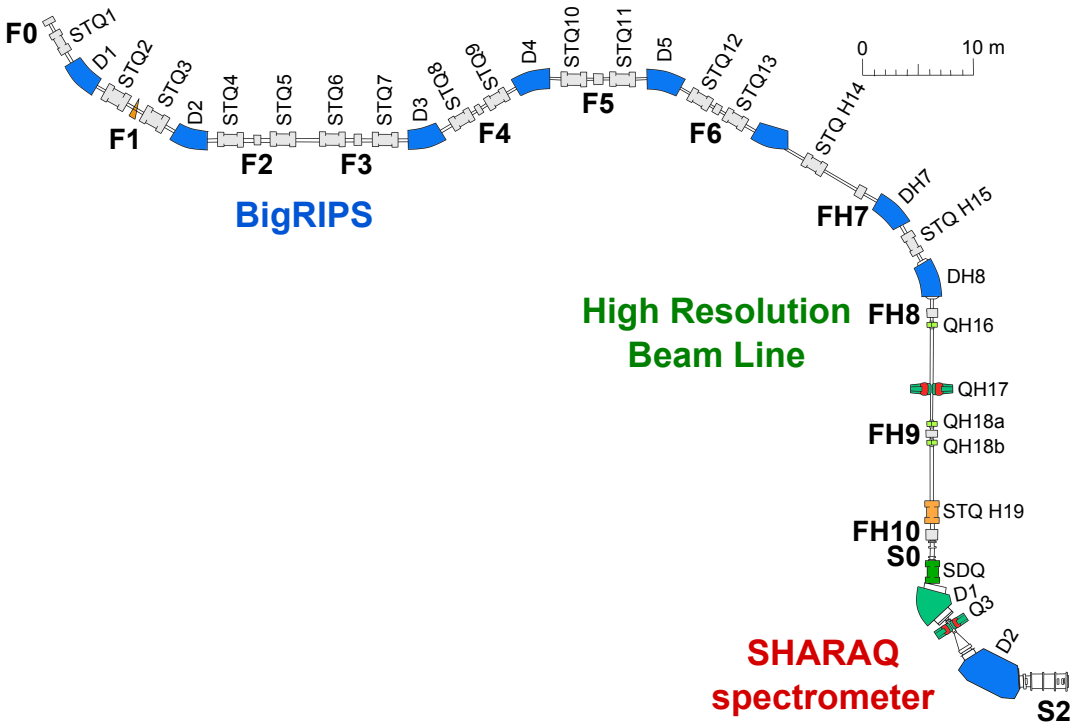

Figure 2.1: Schematic view of the BigRIPS separator, the High-Resolution Beam Line, and the SHARAQ spectrometer.

avalanche counter (PPAC) located at S0, which is the dispersive focus at the target location of SHARAQ.

To correct the flight path lengths with the tracking information on an event-by-event basis, two low-pressure multi-wire drift chambers (LP-MWDCs) were installed at both F3 and S2 in addition to the diamond detectors. At the final focal plane of SHARAQ (S2), two silicon strip detectors were placed as energy loss detectors, which allowed unambiguous particle identification of exotic nuclides with similar mass-to-charge ratios. Details of these beam-line detectors are described in Sec. 2.4.1.

2.1.2 Expected mass uncertainty

The mass resolution is deduced from Eq. (1.6):

$$\frac{\sigma_m}{m} = \sqrt{\left(\frac{\sigma_{B\rho}}{B\rho}\right)^2 + \gamma^4 \left[\left(\frac{\sigma_L}{L}\right)^2 + \left(\frac{\sigma_t}{t}\right)^2\right]}. \tag{2.1}$$

In the present experiment, the Lorentz factor is $\gamma \sim 1.3$. The momentum resolution of 1/14700 (FWHM) can be achieved in the dispersion-matching mode of the beam line and SHARAQ [72].

As mentioned above, the flight length of an ion is corrected by the LP-MWDCs, which have typical position resolutions of 300 μm [73]. The predictive power of the flight path length was evaluated from the beam position and angle at F3 by the transport calculation with the expected detector resolutions in which up to the fifth-order aberrations were taken into consideration. The estimated precision of the flight length is $\sigma_L/L = 5.8 \times 10^{-5}$. Diamond detectors are known to have quite high time resolutions. The newly developed diamond detector used in the present experiment had a time resolution of 30 ps in the previous measurement [74]. Thus, the TOF precision of $\sigma_t/t = 8.0 \times 10^{-5}$ is expected to be achieved. Based on these evaluations, the expected mass resolution is $\sigma_m/m = 1.4 \times 10^{-4}$.

The mass uncertainty δm is dependent on the number of events of the ion, N. The statistical uncertainty is determined by $\delta_{\text{stat}} = \sigma_m/\sqrt{N}$. The systematic uncertainty is typically $\delta_{\text{syst}}/m \sim 2 \times 10^{-6}$ in the previous TOF mass measurements [52]. Assuming that the mass uncertainty is determined by the statistical and systematic ones, the relative mass uncertainty is evaluated as

$$\left(\frac{\delta m}{m}\right)^2 = \left(\frac{\delta_{\text{stat}}}{m}\right)^2 + \left(\frac{\delta_{\text{syst}}}{m}\right)^2. \tag{2.2}$$

The evaluated mass uncertainties for different numbers of events are summarized in Table 2.1. Based on the evaluation, more than 1000 events are required to achieve the mass uncertainty of $\delta m < 300$ keV ($\delta m/m = 4.8 \times 10^{-6}$) for the nuclei in the vicinity of ^{55}Ca.

Table 2.1: Expected mass uncertainties for different numbers of events. The δm values in the bottom row are calculated for ^{55}Ca.

N	10000	5000	1000	500	100	50
$\delta m/m$	2.4×10^{-6}	2.8×10^{-6}	4.8×10^{-6}	6.5×10^{-6}	1.4×10^{-5}	2.0×10^{-5}
δm	140 keV	160 keV	300 keV	400 keV	880 keV	1200 keV

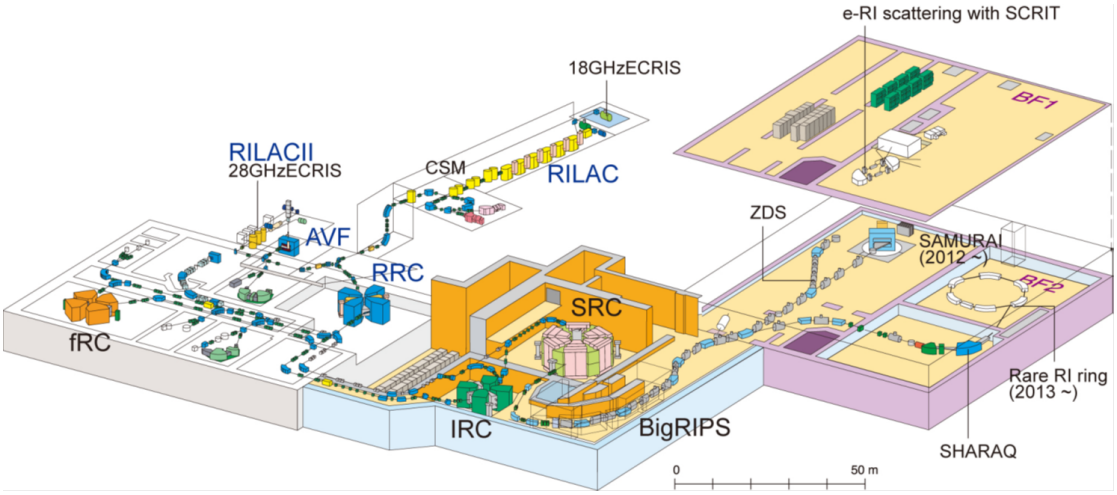

Figure 2.2: Overview of the RIBF facility.

2.2 Experimental facilities

In this section, the experimental facilities consisting of the accelerators, the BigRIPS fragment separator, the High-Resolution Beam Line, and the SHARAQ spectrometer are described. The layout of the RIBF facility is shown in Fig. 2.2.

2.2.1 Accelerators

In the present experiment, the RILAC injector equipped with an 18-GHz electron cyclotron resonance (ECR) ion source was used. A primary ^{70}Zn beam was accelerated up to 345 MeV/u by the three booster cyclotrons, RIKEN Ring Cyclotron (RRC, K = 540 MeV), Intermediate-stage Ring Cyclotron (IRC, K = 980 MeV), and Superconducting Ring Cyclotron (SRC, K = 2600 MeV). The maximum intensity of the primary ^{70}Zn beam was 130 pnA during the experiment.

2.2.2 BigRIPS fragment separator

The BigRIPS separator is the superconducting in-flight RI beam separator at RIKEN [75]. A schematic view of BigRIPS is shown in Fig. 2.1. A wedge-shaped aluminum degrader with a thickness of 1 mm was inserted at the momentum-dispersive focus F1, and a collimator was placed at F2 to decrease background light particles. The secondary beams emitted from the production target installed at the starting point of the BigRIPS separator (F0) were achromatically focused at F3.

In the present experiment, the ^{70}Zn primary beam at an energy of 345 MeV/u bombarded a ^{9}Be production target at F0, yielding the secondary beam containing neutron-rich isotopes by projectile fragmentation. Thicknesses of the production target were 8 mm and 12 mm to produce the cocktail beam in the vicinity of ^{52}Ca and ^{55}Ca, respectively. Hereafter, the experimental setting producing the beam in the vicinity of ^{55}Ca (^{52}Ca) is referred to as the ^{55}Ca (^{52}Ca) setting. Physics runs in the present experiment were taken predominantly in the

^{55}Ca setting. The secondary beam was separated in BigRIPS and transported through BigRIPS and the High-Resolution Beam Line to the SHARAQ spectrometer.

2.2.3 High-Resolution Beam Line and SHARAQ spectrometer

The High-Resolution Beam Line (HRB) is the dedicated beam line for the SHARAQ spectrometer [72, 76]. A schematic view of the HRB and SHARAQ is shown in Fig. 2.1. The HRB and SHARAQ are designed to satisfy the lateral and angular dispersion-matching conditions [77]. In the dispersion-matching transport mode, the whole system is achromatic so that the momentum spread of the beam emitted from the starting point of the beam line (F3) is canceled out at the final focal plane (S2), and the beam is momentum dispersed at the target position of SHARAQ (S0). The dispersion-matched operation of SHARAQ allows high-precision measurements of the beam momenta. Details of the ion optics are described in Sec. 2.3. Ion-optical design of the HRB in the dispersion-matching mode is summarized in Table 2.2. The design momentum resolution is $\delta p/p = 1/14700$ from a first-order ion-optical calculation.

The SHARAQ spectrometer consists of three quadrupole magnets (Q) and two dipole magnets (D) in a configuration of Q1-Q2-D1-Q3-D2. The first two quadrupole magnets (Q1 and Q2) are superconducting (SDQ). Specifications of the SHARAQ spectrometer are summarized in Table 2.3.

Table 2.2: Ion-optical design of the HRB in the dispersion-matching mode.

Momentum acceptance	±0.3%
Horizontal acceptance	±10 mrad
Vertical acceptance	±30 mrad
Maximum dispersion	14.7 m (at S0)
Momentum resolution	1/14700

Table 2.3: Specifications of the SHARAQ spectrometer.

Maximum rigidity	6.8 Tm
Momentum dispersion (D)	5.86 m
Horizontal magnification (M_x)	0.40
D/M_x	14.7 m
Resolving power (for image size of 1 mm)	14700
Vertical magnification	0.0
Angular resolution	$<$ 1 mrad
Momentum acceptance	±1%
Vertical acceptance	±50 mrad
Horizontal acceptance	±17 mrad (dispersion-matching mode)
Solid angle	2.7 mstr (dispersion-matching mode)

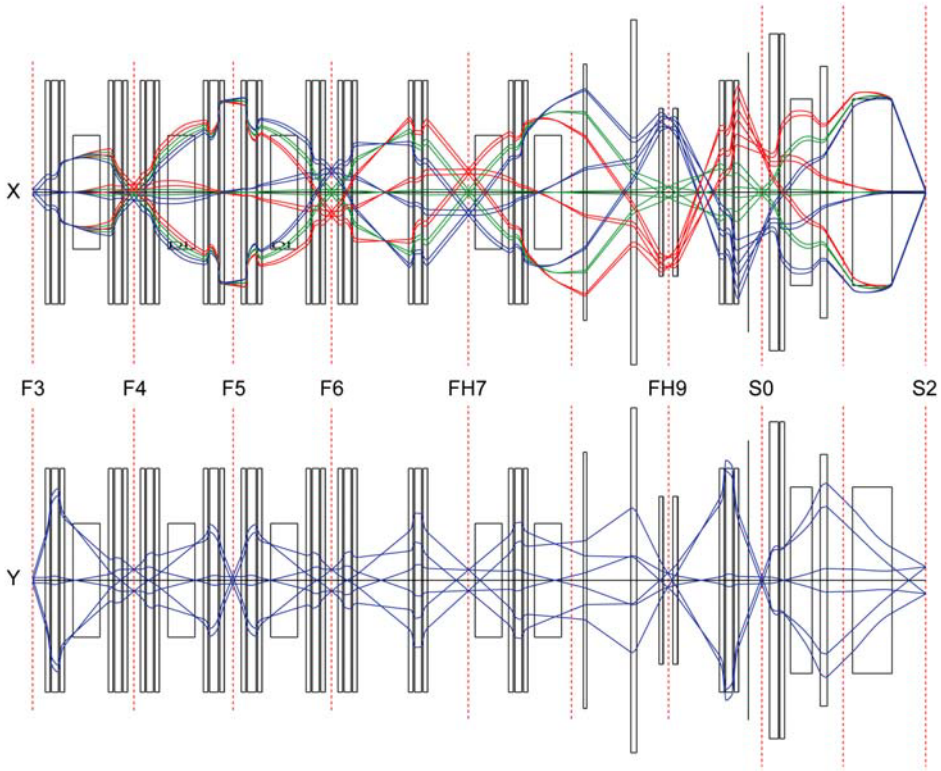

Figure 2.3: Dispersion-matching beam transport from F3 to S2. In the X (Y) plane, the beam trajectories at the initial angles of a_{F3} (b_{F3}) = ±10 (±30) mrad and 0 mrad, are displayed. In the X plane, blue, green, and red lines show the beam trajectories at $\delta p/p = +0.3\%$, 0%, and −0.3%, respectively.

2.3 Ion optics

In the present experiment, SHARAQ was operated in the dispersion-matching transport mode. Figure 2.3 shows the beam transport in the dispersion-matching mode calculated with the code COSY INFINITY [78]. The upper figure shows the beam trajectories in the horizontal direction with the angular deviation from the central ray of ±10 mrad. Each colored line shows a beam trajectory at the fractional momentum deviation of $\delta p/p = \pm 0.3\%$. The lower figure shows those in the vertical direction with the angular deviation of ±30 mrad. In the present experiment, the focus point at S0 is 200 mm downstream from the standard ion optics for optimization of the transport efficiency in the SHARAQ spectrometer, and the focus at S2 is moved 315 mm downstream to obtain the small image size at the stopper surrounded by the γ-ray detectors placed downstream of S2, which are described in Sec. 2.4.2. Furthermore, the vertical magnification in the SHARAQ spectrometer was set to −2.5 to achieve the small image at S2 relative to the diamond detector, while the design value is 0.0 (see Table 2.3).

The transport from the starting point of the beam line to the focal plane of the spectrometer is described using the transport matrices of the beam line ($\boldsymbol{T}_B$) and the spectrometer ($\boldsymbol{T}_S$) as

follows:

$$\begin{pmatrix} x_{\rm fp} \\ \theta_{\rm fp} \\ \delta_{\rm fp} \end{pmatrix} = \boldsymbol{T}_S \boldsymbol{T}_B \begin{pmatrix} x_0 \\ \theta_0 \\ \delta_0 \end{pmatrix} \tag{2.3}$$

$$= \begin{pmatrix} (x|x)_S & (x|a)_S & (x|\delta)_S \\ (a|x)_S & (a|a)_S & (a|\delta)_S \\ 0 & 0 & 1 \end{pmatrix} \begin{pmatrix} (x|x)_B & (x|a)_B & (x|\delta)_B \\ (a|x)_B & (a|a)_B & (a|\delta)_B \\ 0 & 0 & 1 \end{pmatrix} \begin{pmatrix} x_0 \\ \theta_0 \\ \delta_0 \end{pmatrix} \tag{2.4}$$

$$\equiv \begin{pmatrix} s_{11} & s_{12} & s_{16} \\ s_{21} & s_{22} & s_{26} \\ 0 & 0 & 1 \end{pmatrix} \begin{pmatrix} b_{11} & b_{12} & b_{16} \\ b_{21} & b_{22} & b_{26} \\ 0 & 0 & 1 \end{pmatrix} \begin{pmatrix} x_0 \\ \theta_0 \\ \delta_0 \end{pmatrix}, \tag{2.5}$$

where x_0, θ_0, and $\delta_0 \equiv \delta p/p$ are the horizontal position, angle, and fractional momentum deviation from the central trajectory at the starting point of the beam line, and $x_{\rm fp}$, $\theta_{\rm fp}$, and $\delta_{\rm fp}$ are those at the focal plane at the spectrometer. Therefore, $x_{\rm fp}$ and $\theta_{\rm fp}$ are given by

$$x_{\rm fp} = (s_{11}b_{11} + s_{12}b_{21})x_0 + (s_{11}b_{12} + s_{12}b_{22})\theta_0 + (s_{11}b_{16} + s_{12}b_{26} + s_{16})\delta_0, \tag{2.6}$$

$$\theta_{\rm fp} = (s_{21}b_{11} + s_{22}b_{21})x_0 + (s_{21}b_{12} + s_{22}b_{22})\theta_0 + (s_{21}b_{16} + s_{22}b_{26} + s_{26})\delta_0. \tag{2.7}$$

When the momentum dependent terms in Eqs. (2.6) and (2.7) vanish as

$$s_{11}b_{16} + s_{12}b_{26} + s_{16} = 0, \tag{2.8}$$

$$s_{21}b_{16} + s_{22}b_{26} + s_{26} = 0, \tag{2.9}$$

the lateral and angular dispersion-matching conditions are satisfied. The transfer matrix of the SHARAQ spectrometer from S0 to S2 is summarized in Table 2.4. From Eqs. (2.8) and (2.9) with the transfer matrix elements of the SHARAQ spectrometer, those of the beam line in the dispersion-matching condition are determined:

$$b_{16} = (x|\delta)_B = -15.1, \tag{2.10}$$

$$b_{26} = (a|\delta)_B = +3.18. \tag{2.11}$$

The transfer matrix elements of the beam line from F3 to S0 and those of the whole system from F3 to S2 are summarized in Tables 2.5 and 2.6, respectively.

Table 2.4: Transfer matrix of the SHARAQ spectrometer from S0 to S2.

$(x\|x)_S$	−0.383	$(x\|a)_S$	−0.051
$(a\|x)_S$	−0.526	$(a\|a)_S$	−2.683
$(y\|y)_S$	−2.500	$(y\|b)_S$	0.000
$(b\|y)_S$	−0.258	$(b\|b)_S$	−0.400
$(x\|\delta)_S$	−5.625	$(a\|\delta)_S$	0.573

Table 2.5: Transfer matrix of the beam line from F3 to S0.

$(x\|x)_B$	-1.060	$(x\|a)_B$	0.000
$(a\|x)_B$	0.206	$(a\|a)_B$	-0.943
$(y\|y)_B$	1.227	$(y\|b)_B$	0.000
$(b\|y)_B$	-0.088	$(b\|b)_B$	0.815
$(x\|\delta)_B$	-15.121	$(a\|\delta)_B$	3.176

Table 2.6: Transfer matrix of the whole system from F3 to S2.

$(x\|x)$	0.395	$(x\|a)$	0.048
$(a\|x)$	0.005	$(a\|a)$	2.530
$(y\|y)$	-3.067	$(y\|b)$	0.000
$(b\|y)$	-0.282	$(b\|b)$	-0.326
$(x\|\delta)$	0.000	$(a\|\delta)$	0.000

2.4 Detectors

2.4.1 Beam-line detectors

In this section, the detailed descriptions of the detectors installed in the beam line are given. Table 2.7 shows a list of the beam-line detectors used in the present experiment. The layouts of the beam-line detectors at the focal planes F3 and S2 are displayed in Fig. 2.4.

Table 2.7: List of the beam-line detectors used in the present experiment.

Focal plane	Detector	Type	Name	Sensitive area (X mm $\times$ Y mm)	Used during physics runs
F3	Diamond	200 μm^{t}	F3Dia	28×28	✓
	Plastic	0.5 mm^{t}	F3Pla	120×100	✓
	LP-MWDC	T20-half	DC31	80×80	✓
	LP-MWDC	T21	DC32	80×80	✓
FH7	Plastic	3 mm^{t}	FH7Pla	220×150	
	LP-MWDC	Type A	DC71	216×144	
	LP-MWDC	Type A	DC72	216×144	
FH9	Plastic	3 mm^{t}	FH9Pla	220×150	
	LP-MWDC	Type A	DC91	216×144	
FH10	Plastic	3 mm^{t}	FH10Pla	220×150	
	LP-MWDC	Type B	DCX1	216×144	
	LP-MWDC	Type B	DCX2	216×144	
S0	PPAC	Single	S0PPAC	240×150	✓
S2	Diamond	200 μm^{t}	S2Dia	28×28	✓
	Plastic	10 mm^{t}	S2Pla	50×50	✓
	LP-MWDC	Type C	DCS1	216×144	✓
	LP-MWDC	Type C	DCS2	216×144	✓
	SSD	500 μm^{t}	S2Si1	90.6×90.6	✓
	SSD	500 μm^{t}	S2Si2	90.6×90.6	✓

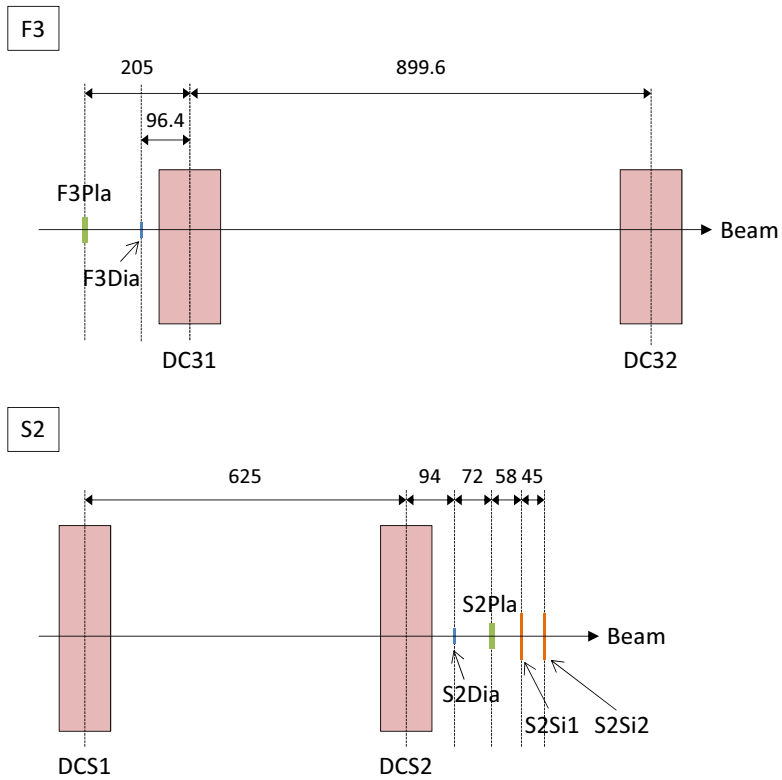

Figure 2.4: Layouts of the beam-line detectors in the F3 and S2 chambers from the top view.

Diamond detector

Diamond detectors were installed at F3 and S2 for the TOF measurement. The detectors are based on polycrystalline diamond produced by chemical vapor deposition (CVD). Details of the diamond detectors are found in Ref. [74].

Thanks to the outstanding properties of diamond, particle detectors using diamond show a quite fast response and excellent radiation hardness. Properties of diamond are summarized in Table 2.8 as well as those of silicon, which is typical semiconductor material and commonly used in nuclear physics experiment. Diamond is semiconductor material with a band-gap of 5.5 eV. One of the noteworthy features of diamond is its high charge carrier mobility, which leads to the fast rise time of detector signals and extremely good time resolution of the detector. In the previous measurement, the time resolution of 27 ps (σ) was achieved for the 32-MeV α particles, energy loss of which corresponds to that of 320-MeV/u ^{12}N isotopes [74]. Another distinct feature of diamond is its high displacement energy. Since a high energy is needed to remove a carbon atom from a lattice, a diamond detector is extremely radiation hard, and can be operated even under high-intensity heavy ion beams.

Figure 2.5 shows a picture and a schematic view of the diamond detector. The size and thickness of the diamond crystal is 30×30 mm^2 and 200 μm, respectively. The size of the sensitive area is 28×28 mm^2. The detector consists of an anode pad (Side A), and a cathode (Side B), which is divided into four strips. The widths of the strips are 9 mm for the top and bottom ones (Strip 1 and Strip 4), and 5 mm for the two central ones (Strip 2 and Strip 3).

Table 2.8: Comparison of diamond and silicon properties.

Physical properties at 300 K	Diamond	Silicon
Band gap (eV)	5.5	1.12
Breakdown field (V/m)	10^7	3×10^5
Resistivity (Ωcm)	$> 10^{11}$	2.3×10^5
Electron mobility (cm^2/V/s)	1800	1500
Hole mobility (cm^2/V/s)	1200	600
Saturation velocity (km/s)	220	82
Dielectric constant	5.7	11.9
Displacement Energy (eV/atom)	43	13–20
Energy to create an e-h pair (eV)	13	3.6
Thermal conductivity (W/cm/K)	20	1.27
Lattice constant (Å)	3.57	5.43

Cathode signals are read from the readouts on both sides of each strip to correct for the position dependence in the timing and charge measurements. An anode signal is read from one of the readouts at the corners in the pad. In the present experiment, only two strips at the bottom (Strip 3 and Strip 4) in the diamond detector at F3 (F3Dia) were read because of the small beam spot size at the achromatic focus F3, while all the strips in the detector at S2 (S2Dia) were read out. The applied voltage was −220 V in the present experiment.

Figure 2.6 shows the electronic circuit for the diamond detector. Signals from both the anode and the cathode strips were amplified by low-noise current amplifiers (Cividec C2 Broadband Amplifier, 2 GHz, 40 dB) or high frequency preamplifiers (Fuji diamond Co., Ltd. Fast Pulse Preamplifier 1107). Table 2.9 summarizes the preamplifiers used in the experiment. The amplified signals were divided into two branches. One was processed by a high-speed leading-edge discriminator (IWATSU UFD4), which is designed to obtain extremely fast response with a time resolution of 10 ps using a ultra-high-speed comparator. The discriminated signal was transfered through an optical cable with a length of ∼150 m, and delivered into a single-hit Time-to-Digital Converter (TDC) (Agilent Technologies TC842), which has a time resolution of 5 ps. The jitter in the transfer system was estimated to be 11.7 ps (σ) [74]. The other signal was for the charge measurement. For the charge measurement, we employed a Charge-to-Time Converter (QTC) module (Iwatsu CLC101EF), which integrates the input analogue signal and provides the charge information by the time-over-threshold method as well as the timing information. The output signal of the QTC was delivered into a multi-hit TDC (CAEN V1190).

Plastic scintillator

In the beam line, plastic scintillators were placed at F3, FH7, FH9, FH10, and S2. The plastic scintillators at F3 and S2 were employed throughout the experiment while those at FH7, FH9, and FH10 were used only during the beam tuning. Figure 2.7 shows the electronic circuit for each plastic scintillator. Light output from each scintillator was read by the photomultiplier tubes (PMTs) on both sides of the scintillator, and sent into a TDC (CAEN V1190) through a

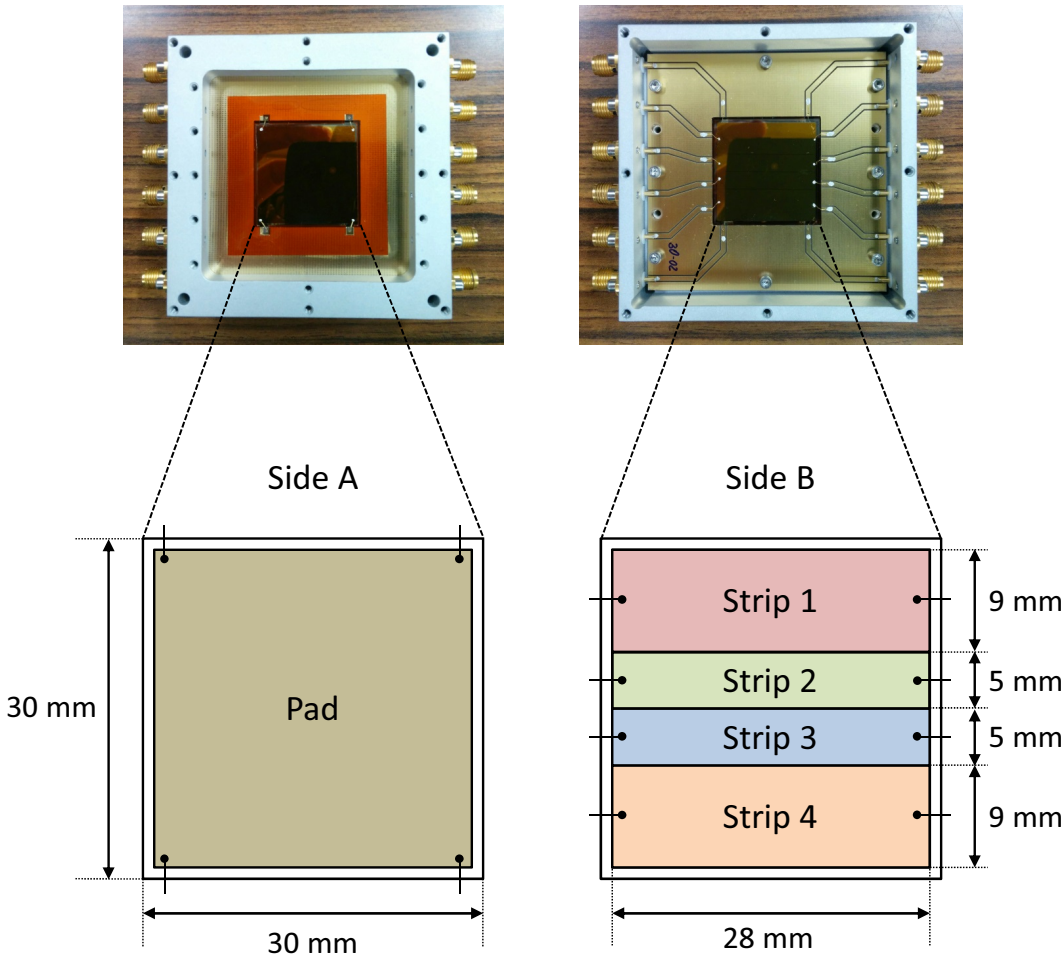

Figure 2.5: Picture and schematic view of the diamond detector used in the present experiment.

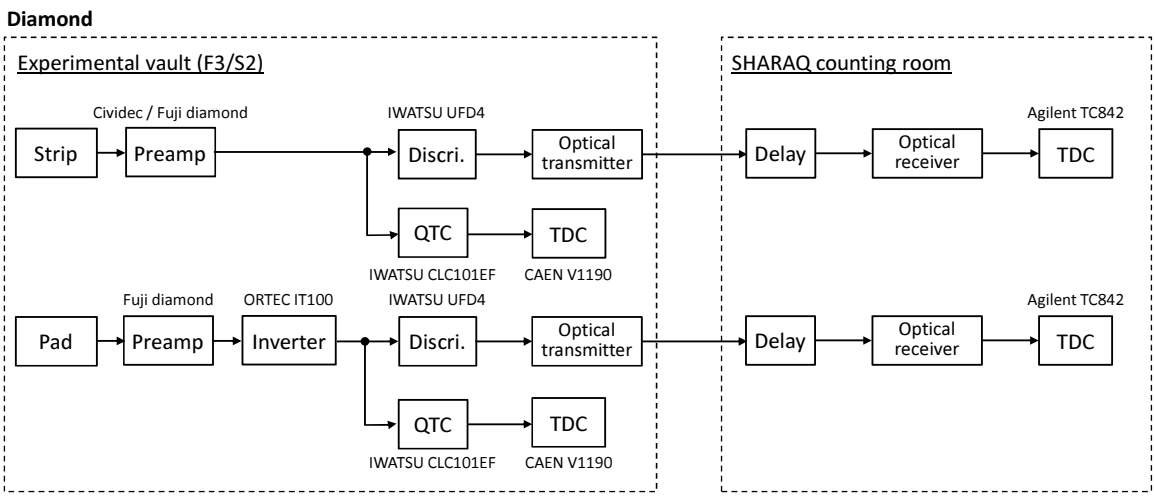

Figure 2.6: Electronic circuit for the diamond detector.

Table 2.9: Readouts in the diamond detectors and used preamplifiers.

Focal plane	Readout	Preamp
F3	Strip 1	–
	Strip 2	–
	Strip 3	Cividec
	Strip 4	Cividec
	Pad	Fuji diamond
S2	Strip 1	Fuji diamond
	Strip 2	Cividec
	Strip 3	Cividec
	Strip 4	Cividec
	Pad	Fuji diamond

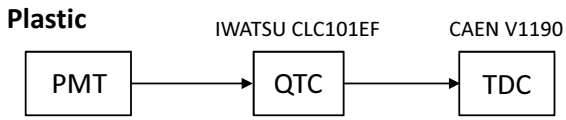

Figure 2.7: Electronic circuit for the plastic scintillator.

QTC for the timing and charge measurements. The PMTs of the plastic scintillators at F3 and S2 were Hamamatsu H1949-51, while those of the scintillators at FH7, FH9, and FH10 were Hamamatsu R7600.

Low-pressure multi-wire drift chamber (LP-MWDC)

Low-pressure multi-wire drift chambers (LP-MWDCs) provide the information on particle tracking. Details of the LP-MWDCs are found in Ref. [73]. Two LP-MWDCs were installed at the focal planes F3, FH7, FH10, and S2, while one was installed at FH9. We refer to those at F3, FH7, FH9, FH10, and S2 as DC31/32, DC71/72, DC91, DCX1/X2, and DCS1/S2, respectively.

Figure 2.8 shows a typical structure of the LP-MWDC, which consists of three anode planes and four cathode planes. An anode plane is sandwiched between two cathode planes. The configuration of the LP-MWDC is characterized by the direction of wires in each anode plane. U-, V-, and Y-axes are defined as those inclined by 30°, −45°, and 90° against the X-axis, respectively. For example, the LP-MWDC shown in Fig. 2.8 has an XUY configuration. The configurations of the LP-MWDCs used in the experiment are summarized in Table 2.10. DC31/32 have XX′YY′, DC71/72 and DC91 have XUY, DCX1/X2 have XUV, and DCS1/S2 have VUU′V′ configurations. The LP-MWDCs were operated in pure isobutane (i-C_4H_{10}) gas at a pressure of ∼10 kPa.

Figure 2.9 shows the electronic circuit for the LP-MWDC. An anode signal was amplified and discriminated by a preamplifier (REPIC RPA-130/131). The timings of leading and trailing edges of the signal were recorded by a TDC (CAEN V1190). Since the pulse width of the logic signal is related to the pulse height of the anode signal, it provides the energy loss information in the LP-MWDC.

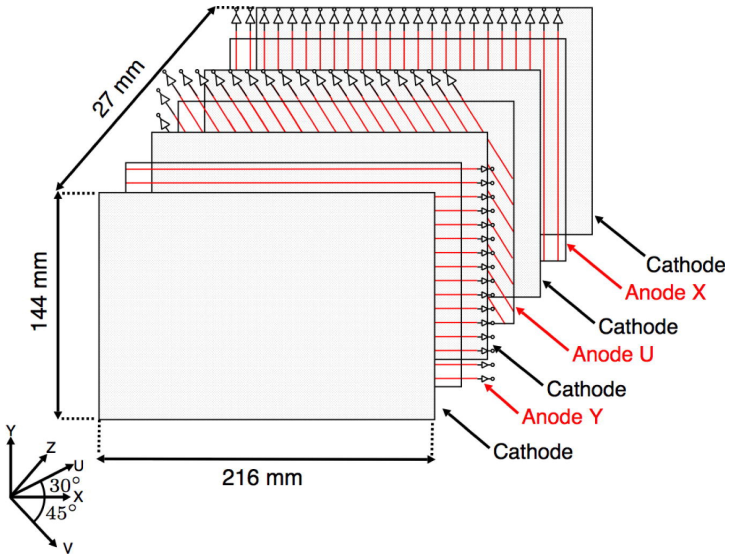

Figure 2.8: Schematic view of the LP-MWDC (XUY configuration) [73].

Table 2.10: Specifications of the LP-MWDCs used in the present experiment.

Name	DC31	DC32	DC71/72 DC91	DCX1/X2	DCS1/S2
Type	T20-half	T21	Type A	Type B	Type C
Sensitive area	80×80 mm^2	80×80 mm^2	216×144 mm^2	216×144 mm^2	216×144 mm^2
Cell size	5×4.8 mm^2	5×4.8 mm^2	9×9 mm^2	9×9 mm^2	9×9 mm^2
Configuration	XX′YY′	XX′YY′	XUY	XUV	VUU′V′
#Ch	16×4	16×4	$24 + 24 + 16$	$24 + 24 + 16$	24×4
Anode wire	Au-W 12.5 μm$^{\phi}$			Au-W 20 μm$^{\phi}$	
Potential wire			Cu-W 75 μm$^{\phi}$		
Cathode foil			Myler 1.5 μm^{t}		
Gas fill			Pure isobutane (i-C_4H_{10}), 10 kPa		
Window foil			25 μm^{t}		
Voltage			~ -1 kV		

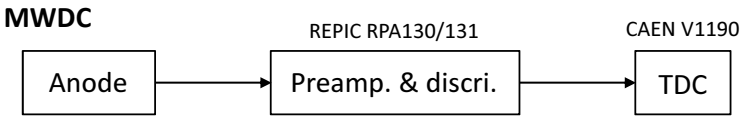

Figure 2.9: Electronic circuit for the LP-MWDC.

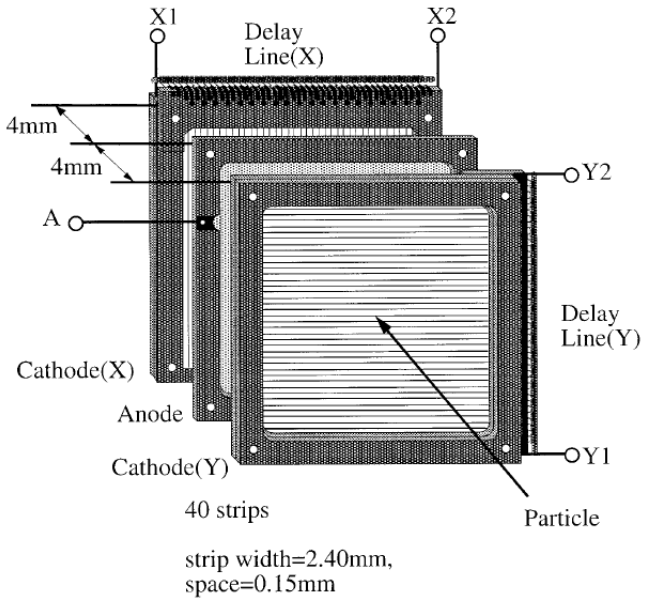

Figure 2.10: Schematic view of the PPAC [79].

Parallel-plate avalanche counter (PPAC)

In the present experiment, a parallel-plate avalanche counter (PPAC) was installed at the dispersive focal plane S0, which is the target position of SHARAQ, to measure the $B\rho$ value. Details of the PPACs are found in Ref. [79]. Figure 2.10 shows a schematic view of the PPAC. An anode plate is located between two cathodes plates, of which every two neighboring strips are connected with each other by delay lines. An active area of the PPAC used in the experiment was 240×150 mm^2. The PPAC was operated in isobutane (i-C_4H_{10}) gas at a pressure of $\sim$10 Torr (= 1.33 kPa).

Figure 2.11 shows the electronic circuit for the PPAC. Analogue signals from the anode plates (X_1, X_2, Y_1, and Y_2) were amplified by a timing filter amplifier (TFA), and split into two branches for the timing and charge measurements. The signals for the timing measurement were sent to a constant fraction discriminator (CFD), and read by a TDC (CAEN V1190), while those for the charge measurement were processed with a QTC and a TDC (CAEN V1190). The hit position on the PPAC in the X (Y) direction was calculated from the time difference between X_1 (Y_1) and X_2 (Y_2).

Silicon strip detector

Two silicon strip detectors (SSDs) (Hamamatsu S10938-9340(X)) were placed at S2 for the energy measurement to identify the proton numbers of fragments. Figure 2.12 shows a schematic

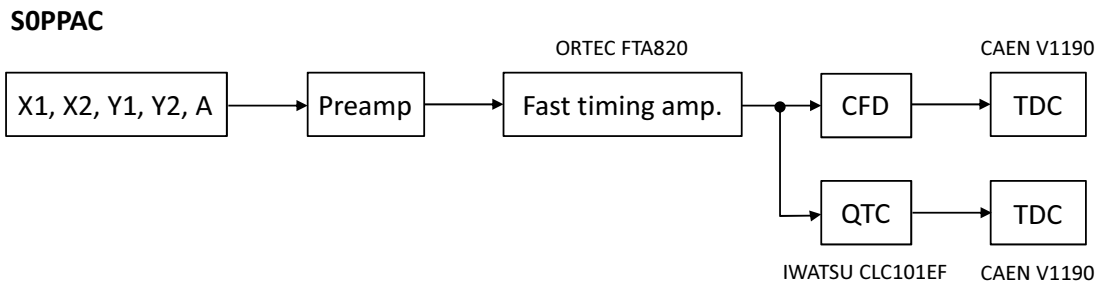

Figure 2.11: Electronic circuit for the PPAC.

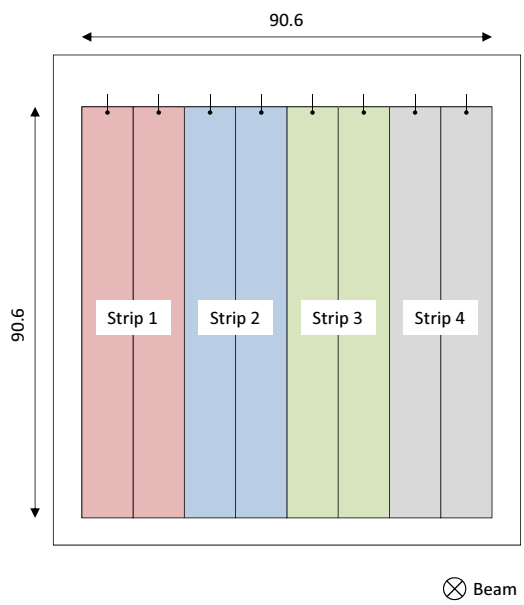

Figure 2.12: Schematic view of the SSD used in the present experiment. Signals from two neighboring strips shown in the same color were read together.

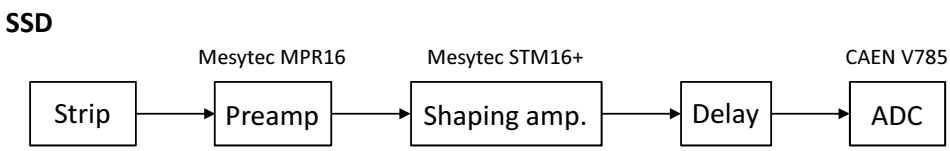

Figure 2.13: Electronic circuit for the SSD.

view of the SSD. Each SSD has an active area of 90.6×90.6 mm^2, which is segmented into 11.3-mm-width strips in the vertical direction, and a thickness of 500 μm. In the present experiment, signals from two neighboring strips were read together.

Figure 2.13 shows the electronic circuit for the SSD. The charge signal from each SSD was firstly amplified by a charge sensitive preamplifier (Mesytec MPR16), and delivered into a shaping amplifier (Mesytec STM16+). After the shaping, the output signal was recorded by a peak-sensitive ADC (CAEN V785) for the energy measurement. The applied voltage was -100 V.

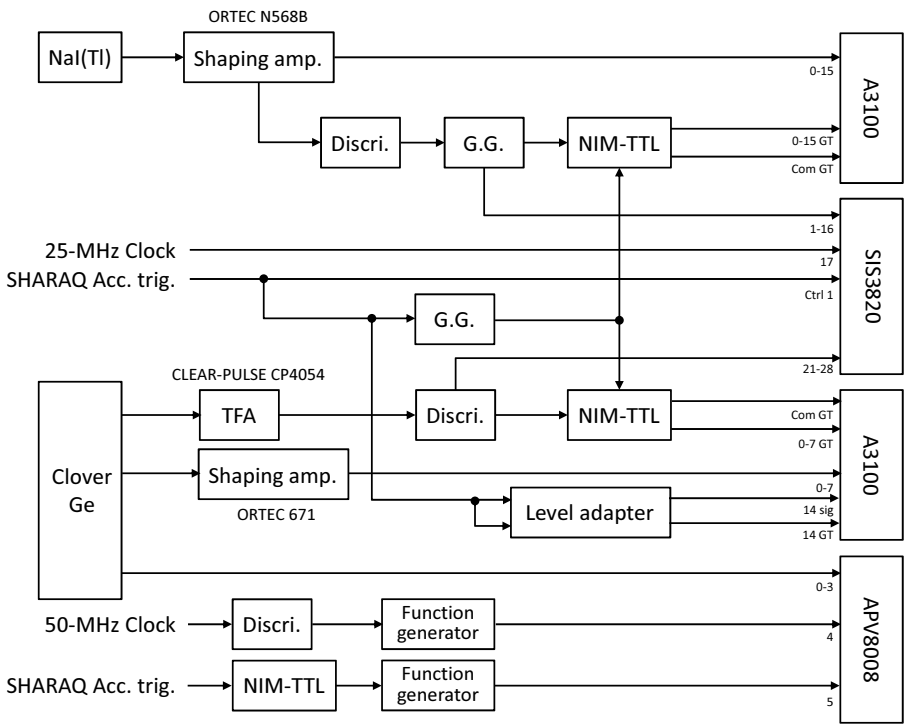

Figure 2.14: Electronic circuit for the γ-ray detector array.

2.4.2 Gamma-ray detector array

A γ-ray detector array consisting of 2 HPGe clover and 16 NaI(Tl) detectors were installed downstream of S2 in the air in order to confirm the particle identification by identifying isomeric states, which lead to a systematic shift towards higher masses in the mass measurements. Details of the γ-ray detector system can be found in Ref. [80]. Figure 2.14 shows the electronic circuit for the γ-ray detector array.

Figure 2.15 shows the experimental setup downstream of S2, which is referred to as S2+, and Fig. 2.16 shows the setup at S2 and S2+ from the top view. A 20-mm-thick plastic was placed as a beam stopper at the center of the detector array. An aluminum degrader was installed upstream of the array to adjust the stopping range of the nuclei of interest. Four degraders with thicknesses of 12 mm, 14 mm, 16 mm, and 18 mm were prepared, and the thickness was changed during the experiment. Two veto scintillators were installed downstream of the array to reject the events in which the nuclei penetrated the stopper.

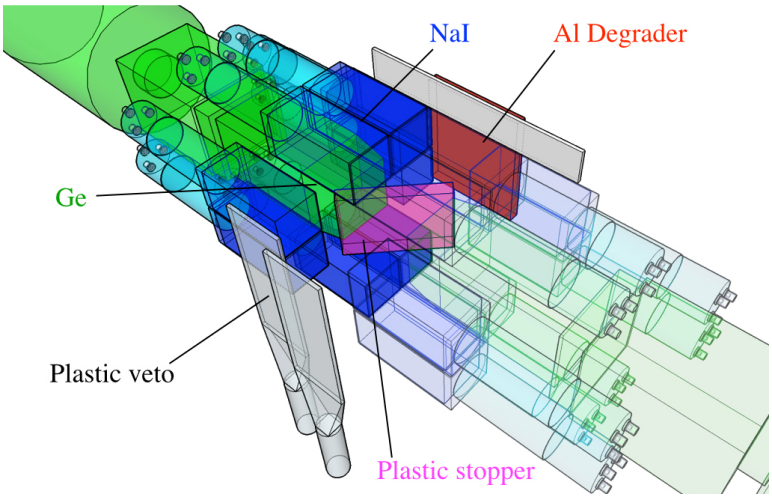

Figure 2.15: Experimental setup at S2+ [80].

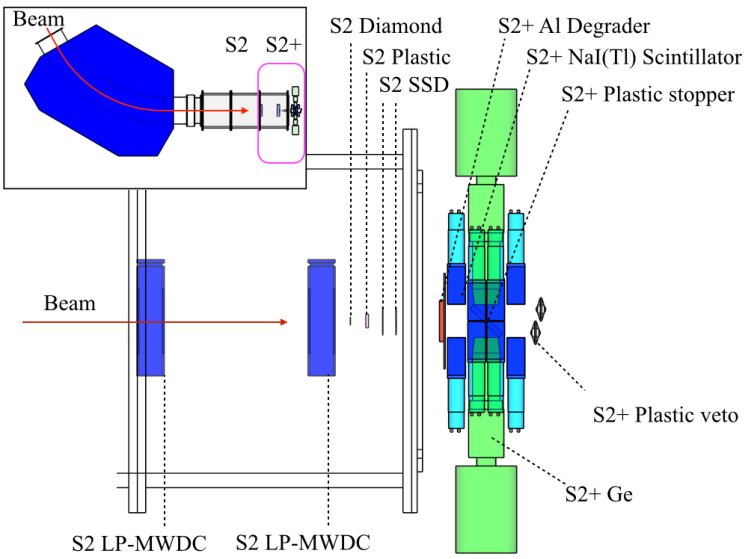

Figure 2.16: Experimental setup at S2 and S2+ from the top view [80].

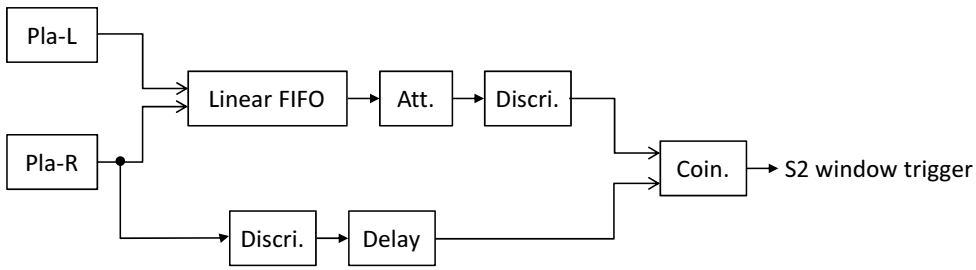

Figure 2.17: Schematic diagram of the electronics for the S2 window trigger.

2.5 Data acquisition

2.5.1 Data acquisition system

The data acquisition (DAQ) was performed by the RIBF-DAQ system [81], which is designed to carry out network-distributed data processing, hierarchical event building, and parallel readout. The system is versatile and scalable so that it can satisfy the various requirements for the experiments performed at RIBF. The DAQ system can be divided into a sub-DAQ system for each detector segment, and each sub-DAQ can locally perform the event build in parallel.

In the present experiment, a sub-DAQ system was placed at each focal plane. For the beam-line detectors, an event fragment in each sub-DAQ system was sent to the event building server, and integrated into a complete event. The DAQ system for the γ-ray detectors was separated from that for the beam-line detectors, and operated with single triggers from the γ-ray detectors. The data in each DAQ system are labeled by a common timestamp so that the γ-ray data can be combined with that from the beam-line detectors. Details of the DAQ system for the γ-ray detectors are presented in Ref. [80].

2.5.2 Triggers

In the present experiment, the following trigger conditions are defined for an event:

- The F3 downscale trigger is generated when the plastic scintillator at F3 (F3Pla) is fired. The trigger events are reduced by a factor of 1/20 (1/100) in the ^{55}Ca (^{52}Ca) setting.
- The FH10 trigger is generated when the plastic scintillator at FH10 (FH10Pla) is fired.
- The S2 trigger is generated when the plastic scintillator at S2 (S2Pla) is fired.
- The S2 window trigger is generated when the plastic scintillator at S2 (S2Pla) is fired, and the energy loss in the plastic is larger than that of the $Z = 10$ isotopes (Ne).

The F3 and FH10 triggers were used in the calibration runs for the LP-MWDCs and the ion-optical tuning. The S2 window trigger, which was prepared in order to reduce the trigger rate at S2 by rejecting the events caused by light ions, was used mainly in the physics measurements. The typical rate of the S2 window trigger was ∼150 cps while that of the S2 trigger was ∼2.5 kcps. The diagram of the S2 window trigger is shown in Fig. 2.17.

2.6 Summary of experimental conditions

The data sets taken in the present experiment are summarized in Table 2.11. During the physics runs, two types of data, those in the ^{55}Ca and ^{52}Ca settings, were taken. The data of the present mass measurements were taken primarily in the ^{55}Ca setting while the ^{52}Ca setting provided complementary data. Data for the calibration of the beam-line detectors and the tuning of the beam transport were taken with the beams in the vicinity of ^{52}Ca.

The experimental conditions are summarized in Table 2.12. The settings of the magnets along the beam line were the same in the ^{55}Ca and ^{52}Ca settings.

Table 2.11: List of the data sets stored in the present experiment.

Data set	Trigger condition
^{55}Ca setting	S2 window $\vee$ F3 downscale
^{52}Ca setting	S2 window $\vee$ F3 downscale
Calibration runs (^{52}Ca)	F3 or FH10

Table 2.12: Summary of the experimental conditions.

Primary beam	^{70}Zn
Energy of the primary beam	345 MeV/u
Intensity of the primary beam	130 pnA (max)
Production target (F0)	Be 12 mm^{t} (for ^{55}Ca setting)
	Be 8 mm^{t} (for ^{52}Ca setting)
$B\rho$ (F0–F1)	7.1328 Tm
$B\rho$ (F1–F2)	7.0459 Tm
$B\rho$ (F2–F3)	7.0377 Tm
$B\rho$ (F3–F4)	6.9946 Tm
$B\rho$ (F4–F5)	6.9605 Tm
$B\rho$ (F5–F6)	6.9605 Tm
$B\rho$ (F6–FH7)	6.9605 Tm
$B\rho$ (FH7–FH8)	6.9726 Tm
$B\rho$ (FH8–FH9)	6.9605 Tm
$B\rho$ (FH9–S0)	6.9605 Tm
$B\rho$ (SHARAQ D1)	6.9836 Tm
$B\rho$ (SHARAQ D2)	6.9836 Tm
F1 slit	L: 12.6 mm, R: 12.6 mm
F2 slit	L: 10.0 mm, R: 15.0 mm (^{55}Ca setting)
	L: 120.0 mm, R: 120.0 mm (^{52}Ca setting)
F2 collimator	In
F5 slit	L: 120 mm, R: 120 mm
S2+ degrader	Al 12 mm^{t}, 14 mm^{t}, 16 mm^{t}, or 18 mm^{t}
Count rate at F3	∼3 kcps (^{55}Ca setting)
	∼14 kcps (^{52}Ca setting)
Count rate at S2	∼2 kcps (^{55}Ca setting)
	∼3 kcps (^{52}Ca setting)
S2 window trigger rate	∼300 cps (^{55}Ca setting)
	∼1 kcps (^{52}Ca setting)
Gated trigger rate	∼300 cps (^{55}Ca setting)
	∼1 kcps (^{52}Ca setting)

Chapter 3

Data analysis

本章については、5 年以内に雑誌等で刊行予定のため、非公開。

Chapter 4

Results

本章については、5 年以内に雑誌等で刊行予定のため、非公開。

Chapter 5

Discussion

本章については、5 年以内に雑誌等で刊行予定のため、非公開。

Chapter 6

Conclusion

本章については、5 年以内に雑誌等で刊行予定のため、非公開。

Appendix A

Time resolution of the TOF measurement system

We give details of the evaluation of the time resolution of the TOF measurement system ($\delta t_{\mathrm{system}}$) described in Sec. 3.2.3. The jitter in a long optical-fiber signal-transfer line was measured [74]. The resolutions of the measured jitters were 11.7 ps (σ) and 13.2 ps (σ) at transfer lengths (L) of 312 m and 460 m, respectively. Here, the following two models are considered:

- The jitter is proportional to the transfer length: $\delta t_{\mathrm{system}} \propto L$.
- The jitter is proportional to the square root of the transfer length: $\delta t_{\mathrm{system}} \propto L^{1/2}$.

In Fig. A.1, two colored lines obtained by fitting based on the above assumptions are shown with the measured jitter values. The green and blue lines show the functions proportional to L and $L^{1/2}$, respectively. At a length of 155 m in the present experiment, the estimated time resolution of the system is $\delta t_{\mathrm{system}} \sim 10$ ps (σ).

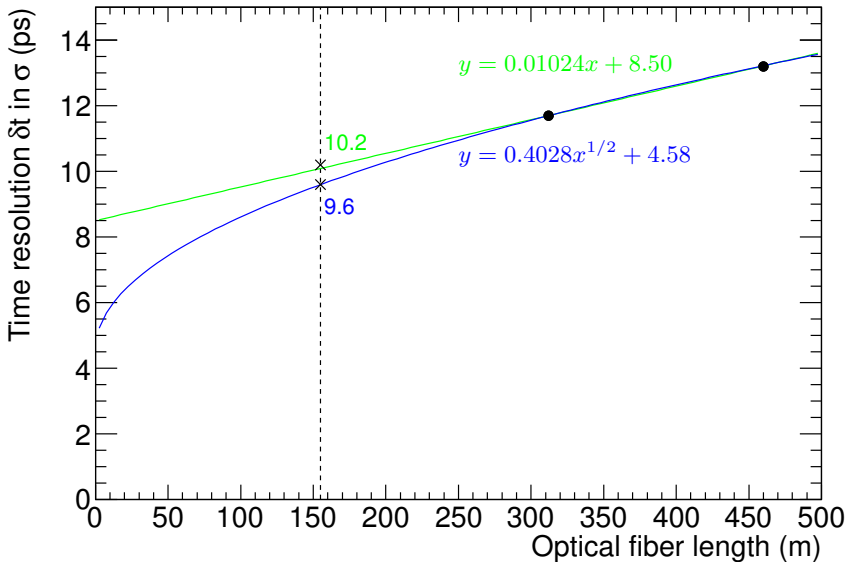

Figure A.1: Measured time resolution of the TOF measurement system versus length of the optical fiber.

Appendix B

Atomic and nuclear masses

In TOF mass measurements, nuclear masses are obtained directly because beams are full-striped in most cases, whereas masses are usually tabulated as atomic rather than nuclear ones. Therefore, one has to know the relation between nuclear and atomic masses.

The nuclear mass $m(A, Z)$ of a nucleus with the mass number A and the proton number Z is given by

$$m(A, Z) = M(A, Z) - Zm_e + B_e(Z), \tag{B.1}$$

where $M(A, Z)$ is the atomic mass, m_e is the electron mass, and $B_e(Z)$ is the total electron binding energy in the atom. The approximate value of $B_e(Z)$ can be obtained using the empirical formula [62]:

$$B_e(Z) = 14.4381 \cdot Z^{2.39} + 1.55468 \times 10^{-6} \cdot Z^{5.35} \text{ [eV]}. \tag{B.2}$$

Figure B.1 shows the B_e values as a function of Z. In the $Z \sim 20$ region, $B_e(Z) \sim 10$–20 keV. While the correction for electron binding energies is quite small relative to nuclear binding energies, it has to be considered because it is comparable to the mass uncertainties in the present mass measurements ($\gtrsim 100$ keV).

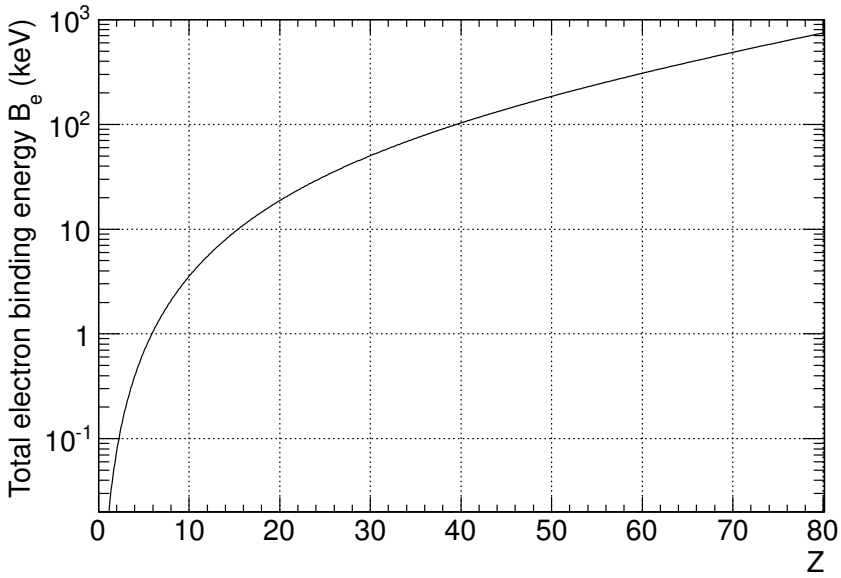

Figure B.1: Total electron binding energy B_e as a function of proton number Z.

Appendix C

Derivation of the mass fitting functions

In this chapter, we derive the mass fitting functions described in Sec. 3.3.3. After the preliminaries given below, derivation of the mass fitting functions, Eqs. (3.28) and (3.29), is provided.

From the equation of motion for a charged particle through a magnetic system, the magnetic rigidity $B\rho$ is given by

$$B\rho = \frac{\gamma m \beta c}{q}, \tag{C.1}$$

where $\beta = L/ct$, $\gamma = 1/\sqrt{1-\beta^2}$, L is the flight length, and t is the time-of-flight (TOF). From this relationship, the mass-to-charge ratio is expressed by

$$\frac{m}{q} = \frac{B\rho}{c}\sqrt{\left(\frac{ct}{L}\right)^2 - 1}, \tag{C.2}$$

and the TOF is given by

$$t = \frac{L}{c}\sqrt{1 + \left(\frac{mc}{qB\rho}\right)^2}. \tag{C.3}$$

We denote the beam parameters at the focal plane F3 as $\mathbf{X_3} \equiv (x_3, a_3, y_3, b_3, \delta_3)$. In addition, we define the magnetic rigidity and the flight length corresponding to the central ray in the beam line as $B\rho_0$ and L_0, respectively. We then obtain

$$L = (1 + \tilde{\ell}(\mathbf{X_3}))L_0, \tag{C.4}$$

$$B\rho = (1 + \delta_3)B\rho_0. \tag{C.5}$$

As the horizontal position at the dispersive focus S0 (x_0) is related to the momentum δ_3, δ_3

depends on $\mathbf{x_3} \equiv (x_3, a_3, y_3, b_3, x_0)$ as $\delta_3 = \tilde{\delta}_3(\mathbf{x_3})$. Then, Eqs. (C.4) and (C.5) lead to

$$L = (1 + \tilde{\ell}(\mathbf{x_3}))L_0, \tag{C.6}$$

$$B\rho = (1 + \tilde{\delta}_3(\mathbf{x_3}))B\rho_0. \tag{C.7}$$

C.1 Derivation of Eq. (3.28)

The square of the mass-to-charge ratio is given by

$$\left(\frac{m}{q}\right)^2 = \left(\frac{B\rho_0}{cL_0}\right)^2 \left[\left(\frac{1 + \tilde{\delta}_3(\mathbf{x_3})}{1 + \tilde{\ell}(\mathbf{x_3})}\right)^2 (ct)^2 - L_0^2(1 + \tilde{\delta}_3(\mathbf{x_3}))\right], \tag{C.8}$$

and can be expanded around $\tilde{\delta}_3 = \tilde{\ell} = 0$ by the Taylor series. Since $\tilde{\delta}_3(\mathbf{x_3})$ and $\tilde{\ell}(\mathbf{x_3})$ are the functions of $\mathbf{x_3} \equiv (x_3, a_3, y_3, b_3, x_0)$, $(m/q)^2$ can be expanded by x_3, a_3, y_3, b_3, and x_0 as

$$\left(\frac{m}{q}\right)^2 \approx t^2 \sum_{i_5+\cdots+i_4=0}^{n} \tilde{C}^{(2)}_{(i_1,\ldots,i_4)} \cdot x_3^{i_1} a_3^{i_2} y_3^{i_3} b_3^{i_4} x_0^{i_5} + \sum_{k_1+\cdots+k_4=0}^{n} \tilde{C}^{(0)}_{(k_1,\ldots,k_5)} \cdot x_3^{k_1} a_3^{k_2} y_3^{k_3} b_3^{k_4} x_0^{k_5}. \tag{C.9}$$

Now, let t_0 be the measured TOF value before being added to the offset t_{offset}. By substituting $t = t_0 + t_{\text{offset}}$ into Eq. (C.9), we obtain

$$\begin{aligned}\left(\frac{m}{q}\right)^2 = {} & t_0^2 \sum_{i_1+\cdots+i_5=0}^{n} C^{(2)}_{(i_1,\ldots,i_4)} \cdot x_3^{i_1} a_3^{i_2} y_3^{i_3} b_3^{i_4} x_0^{i_5} + t_0 \sum_{j_1+\cdots+j_5=0}^{n} C^{(1)}_{(j_1,\ldots,j_4)} \cdot x_3^{j_1} a_3^{j_2} y_3^{j_3} b_3^{j_4} x_0^{j_5} \\ & + \sum_{k_1+\cdots+k_5=0}^{n} C^{(0)}_{(k_1,\ldots,k_4)} \cdot x_3^{k_1} a_3^{k_2} y_3^{k_3} b_3^{k_4} x_0^{k_5}.\end{aligned} \tag{C.10}$$

C.2 Derivation of Eq. (3.29)

Next, let us consider the flight path divided into two parts. The flight length between F3 to S2 (L) is divided into that between F3 and S0 ($L_{\text{F3-S0}}$) and that between S0 and S2 ($L_{\text{S0-S2}}$), which are given by

$$L_{\text{F3-S0}} = (1 + \tilde{\ell}_1(\mathbf{x_3}))L_1, \; L_{\text{S0-S2}} = (1 + \tilde{\ell}_2(\mathbf{x_2}))L_2, \tag{C.11}$$

where $\mathbf{x_2}$ is defined by $\mathbf{x_2} \equiv (x_2, a_2, y_2, b_2, x_0)$. The magnetic rigidity for each path is

$$B\rho_{\text{F3-S0}} = (1 + \tilde{\delta}_1(\mathbf{x_3}))B\rho_1, \; B\rho_{\text{S0-S2}} = (1 + \tilde{\delta}_2(\mathbf{x_2}))B\rho_2. \tag{C.12}$$

The TOF between F3 and S0 (t_1) and between S0 and S2 (t_2) are given by

$$t_1 = \frac{L_1(1 + \tilde{\ell}_1(\mathbf{x_3}))}{c} \sqrt{1 + \left(\frac{mc}{qB\rho_1}\right)^2 \left(\frac{1}{1 + \tilde{\delta}_1(\mathbf{x_3})}\right)^2}, \tag{C.13}$$

$$t_2 = \frac{L_2(1 + \tilde{\ell}_2(\mathbf{x_2}))}{c} \sqrt{1 + \left(\frac{mc}{qB\rho_2}\right)^2 \left(\frac{1}{1 + \tilde{\delta}_2(\mathbf{x_2})}\right)^2}. \tag{C.14}$$

From the relation $t_0 + t_{\text{offset}} = t = t_1 + t_2$, Eqs. (C.13) and (C.14) lead to

$$\begin{aligned} t_0 + t_{\text{offset}} &= \frac{L_1(1+\tilde{\ell}_1(\mathbf{x_3}))}{c}\sqrt{1+\left(\frac{m}{q}\right)^2\left(\frac{c}{B\rho_1}\right)^2\left(\frac{1}{1+\tilde{\delta}_1(\mathbf{x_3})}\right)^2} \\ &\quad + \frac{L_2(1+\tilde{\ell}_2(\mathbf{x_2}))}{c}\sqrt{1+\left(\frac{m}{q}\right)^2\left(\frac{c}{B\rho_2}\right)^2\left(\frac{1}{1+\tilde{\delta}_2(\mathbf{x_2})}\right)^2}. \end{aligned} \tag{C.15}$$

To simplify Eq. (C.15), we define the following quantities:

$$\mu \equiv \left(\frac{m}{q}\right)^2, \tag{C.16}$$

$$A_1 \equiv \left(\frac{L_1(1+\tilde{\ell}_1(\mathbf{x_3}))}{c}\right)^2, \; A_2 \equiv \left(\frac{L_2(1+\tilde{\ell}_2(\mathbf{x_2}))}{c}\right)^2, \tag{C.17}$$

$$B_1 \equiv \left(\frac{c}{B\rho_1(1+\tilde{\delta}_1(\mathbf{x_3}))}\right)^2, \; B_2 \equiv \left(\frac{c}{B\rho_2(1+\tilde{\delta}_2(\mathbf{x_2}))}\right)^2. \tag{C.18}$$

Then, Eq. (C.15) simplifies to

$$t = \sqrt{A_1}\sqrt{1+\mu B_1} + \sqrt{A_2}\sqrt{1+\mu B_2}. \tag{C.19}$$

By raising Eq. (C.19) to the second power, we obtain a quadratic equation of μ:

$$(A_1B_1 - A_2B_2)^2\mu^2 - 2(A_1B_1 + A_2B_2)(t^2 - A_1 - A_2)\mu + \left[(t^2 - A_1 - A_2)^2 - 4A_1A_2\right] = 0. \tag{C.20}$$

The solutions of Eq. (C.20) are

$$\mu = \frac{\zeta\eta \pm 2\sqrt{A_1A_2}\sqrt{\zeta^2 + \eta^2 B_1B_2 - 4A_1A_2B_1B_2}}{\zeta^2 - 4A_1B_1A_2B_2}, \tag{C.21}$$

where ζ and η are defined by

$$\zeta \equiv A_1B_1 + A_2B_2, \; \eta \equiv t^2 - A_1 - A_2. \tag{C.22}$$

We have two possible solutions of μ (+ or − signs in Eq. (C.21)). By substituting the realistic value to each parameter, we constrain the signs in Eq. (C.21):

$$\mu = \left(\frac{m}{q}\right)^2 \approx \left(\frac{55 \times 1.6 \times 10^{-27}}{20 \times 1.6 \times 10^{-19}}\right)^2 = 7.6 \times 10^{-16}\ [\mathrm{A}^{-2}\mathrm{M}^2\mathrm{T}^{-2}], \tag{C.23}$$

$$t^2 = (t_0 + t_{\mathrm{offset}})^2 \approx (500 \times 10^{-9})^2 = 2.5 \times 10^{-13}\ [\mathrm{T}^2], \tag{C.24}$$

$$A_1 = \left(\frac{L_1(1+\tilde{\ell}_1(\mathbf{x_3}))}{c}\right)^2 \approx \left(\frac{80}{3.0 \times 10^8}\right)^2 = 7.1 \times 10^{-14}\ [\mathrm{T}^2], \tag{C.25}$$

$$A_2 = \left(\frac{L_2(1+\tilde{\ell}_2(\mathbf{x_2}))}{c}\right)^2 \approx \left(\frac{20}{3.0 \times 10^8}\right)^2 = 4.4 \times 10^{-15}\ [\mathrm{T}^2], \tag{C.26}$$

$$B_1 = \left(\frac{c}{B\rho_1(1+\tilde{\delta}_1(\mathbf{x_3}))}\right)^2 \approx \left(\frac{3.0 \times 10^8}{7.0}\right)^2 = 1.8 \times 10^{15}\ [\mathrm{A}^2\mathrm{M}^{-2}\mathrm{T}^2], \tag{C.27}$$

$$B_2 = \left(\frac{c}{B\rho_2(1+\tilde{\delta}_2(\mathbf{x_2}))}\right)^2 \approx \left(\frac{3.0 \times 10^8}{7.0}\right)^2 = 1.8 \times 10^{15}\ [\mathrm{A}^2\mathrm{M}^{-2}\mathrm{T}^2], \tag{C.28}$$

$$\zeta = A_1B_1 + A_2B_2 \approx 1.35 \times 10^2\ [\mathrm{A}^2\mathrm{M}^{-2}\mathrm{T}^4], \tag{C.29}$$

$$\eta = t^2 - A_1 - A_2 \approx 1.75 \times 10^{-13}\ [\mathrm{T}^2]. \tag{C.30}$$

Here, the units are in the MKSA system. Then, we have

$$(\text{RHS in Eq. (C.21)}) \approx \begin{cases} 2.54 \times 10^{-15} & (+) \\ 8.84 \times 10^{-16} & (-) \end{cases}. \tag{C.31}$$

We adopt the minus sign in Eq. (C.21), which produces the closer value to $\mu \approx 7.6 \times 10^{-16}$:

$$\mu = \frac{\zeta\eta - 2\sqrt{A_1A_2}\sqrt{\zeta^2 + \eta^2 B_1B_2 - 4A_1A_2B_1B_2}}{\zeta^2 - 4A_1B_1A_2B_2}. \tag{C.32}$$

Next, we define T_0 as the mean value of the TOF, and rewrite the TOF as follows:

$$t = t_0 + t_{\mathrm{offset}} = T_0(1+\tau). \tag{C.33}$$

Then, τ ($\ll 1$) is given by

$$\tau = \frac{t_0}{T_0} + \left(\frac{t_{\mathrm{offset}}}{T_0} - 1\right). \tag{C.34}$$

Eq. (C.32) can be expressed with τ as

$$\mu = A(1+\tau)^2 + B - \sqrt{C(1+\tau)^4 + D(1+\tau)^2 + E}, \tag{C.35}$$

where A, B, C, D, and E are the functions of $\mathbf{x_3}$ and $\mathbf{x_2}$, but not dependent on τ. Eq. (C.35)

can be expanded by τ as

$$\begin{aligned}
\mu &= \mu|_{\tau=0} + \tau \frac{\mathrm{d}\mu}{\mathrm{d}\tau}\bigg|_{\tau=0} + \frac{\tau^2}{2}\frac{\mathrm{d}^2\mu}{\mathrm{d}\tau^2}\bigg|_{\tau=0} + \frac{\tau^3}{6}\frac{\mathrm{d}^3\mu}{\mathrm{d}\tau^3}\bigg|_{\tau=0} + \cdots \qquad \text{(C.36)}\\
&= \left[A + B - \sqrt{C+D+E}\right] + \tau\left[2A - \frac{2C+D}{\sqrt{C+D+E}}\right]\\
&\quad + \frac{\tau^2}{2}\left[2A - \frac{6C+D}{(C+D+E)^{1/2}} + \frac{(2C+D)^2}{(C+D+E)^{3/2}}\right]\\
&\quad + \frac{\tau^3}{6}\left[-\frac{4C}{(C+D+E)^{1/2}} + \frac{(2C+D)(6C+D)}{(C+D+E)^{3/2}} - \frac{(2C+D)^3}{(C+D+E)^{5/2}}\right]\\
&\quad + \frac{\tau^4}{24}\Bigg[-\frac{12C}{(C+D+E)^{1/2}} + \frac{3(6C+D)^2 + 48C(2C+D)}{(C+D+E)^{3/2}} - \frac{18(2C+D)^2(6C+D)}{(C+D+E)^{5/2}}\\
&\qquad\qquad + \frac{16(2C+D)^4}{(C+D+E)^{7/2}}\Bigg]\\
&\quad + \frac{\tau^5}{120}\Bigg[\frac{120C(6C+D) + 60C(2C+D)}{(C+D+E)^{3/2}} - \frac{45C(2C+D)(6C+D)^2 + 180C(2C+D)^2}{(C+D+E)^{5/2}}\\
&\qquad\qquad + \frac{150(2C+D)^3(6C+D)}{(C+D+E)^{7/2}} - \frac{105(2C+D)^5}{(C+D+E)^{9/2}}\Bigg]\\
&\quad + \cdots . \qquad \text{(C.37)}
\end{aligned}$$

The coefficient of each term can be expanded by $\mathbf{x_3}$ and $\mathbf{x_2}$, and τ is related by the linear combination of t_0 in Eq. (C.34). Consequently, we obtain the following simple expression:

$$\begin{aligned}
\mu &\approx \sum_{j_0+\cdots+j_9=0}^{n} \tilde{C}_{(j_0,\ldots,j_9)} \tau^{j_0} x_3^{j_1} a_3^{j_2} y_3^{j_3} b_3^{j_4} x_0^{j_5} x_2^{j_6} a_2^{j_7} y_2^{j_8} b_2^{j_9} \qquad \text{(C.38)}\\
&\approx \sum_{j_0+\cdots+j_9=0}^{n} C_{(j_0,\ldots,j_9)} t_0^{j_0} x_3^{j_1} a_3^{j_2} y_3^{j_3} b_3^{j_4} x_0^{j_5} x_2^{j_6} a_2^{j_7} y_2^{j_8} b_2^{j_9} . \qquad \text{(C.39)}
\end{aligned}$$

Appendix D

Shape of the mass distribution

As mentioned in Sec. 3.3.4, a shape of the deduced mass spectrum is distorted from a Gaussian distribution (or normal distribution). The mass value is calculated by the polynomial of the observables expected to follow Gaussian distributions (see Eq. (3.29)). However, the distribution of the deduced mass does not follow a Gaussian distribution. We discuss this issue in the following.

Let $p(x)$ be the probability density function of a normal distribution

$$p(x) = \frac{1}{\sqrt{2\pi}\sigma}\exp\left(-\frac{(x-\mu)^2}{2\sigma^2}\right), \tag{D.1}$$

where μ and σ are the mean and standard deviation of the distribution, respectively. Then, the probability distribution of $z \equiv x^n$ $(n = 0, 1, 2, \dots)$ is given by

$$f_n(z) = \int_{-\infty}^{\infty} p(x)\delta(z - x^n)\mathrm{d}x, \tag{D.2}$$

where $\delta(x)$ is the Dirac delta function. In the calculation of Eq. (D.2), the following formulae of the Dirac delta are employed:

$$\delta(x^{2n} - a^{2n}) = \frac{1}{2n|a|^{2n-1}}[\delta(x - |a|) + \delta(x + |a|)], \tag{D.3}$$

$$\delta(x^{2n+1} - a^{2n+1}) = \frac{1}{(2n+1)|a|^{2n}}\delta(x - |a|). \tag{D.4}$$

Eq. (D.2) is calculated for $n = 2$, 3 and 4 as follows:

$$
\begin{aligned}
f_2(z) &= \frac{1}{\sqrt{2\pi}\sigma}\int_{-\infty}^{\infty}\frac{\delta(x-\sqrt{z})+\delta(x+\sqrt{z})}{2\sqrt{z}}\exp\left(-\frac{(x-\mu)^2}{2\sigma^2}\right)\mathrm{d}x && \text{(D.5)}\\
&= \frac{1}{2\sqrt{2\pi}\sigma}\frac{1}{\sqrt{z}}\left[\exp\left(-\frac{(\sqrt{z}-\mu)^2}{2\sigma^2}\right)+\exp\left(-\frac{(\sqrt{z}+\mu)^2}{2\sigma^2}\right)\right] \quad (z \geqq 0), && \text{(D.6)}\\
f_3(z) &= \frac{1}{\sqrt{2\pi}\sigma}\int_{-\infty}^{\infty}\frac{\delta(x-\sqrt[3]{z})}{3\sqrt[3]{z^2}}\exp\left(-\frac{(x-\mu)^2}{2\sigma^2}\right)\mathrm{d}x && \text{(D.7)}\\
&= \frac{1}{3\sqrt{2\pi}\sigma}\frac{1}{\sqrt[3]{z^2}}\exp\left(-\frac{(\sqrt[3]{|z|}-\mu)^2}{2\sigma^2}\right), && \text{(D.8)}\\
f_4(z) &= \frac{1}{\sqrt{2\pi}\sigma}\int_{-\infty}^{\infty}\frac{\delta(x-\sqrt[4]{z})+\delta(x+\sqrt[4]{z})}{4\sqrt[4]{z^3}}\exp\left(-\frac{(x-\mu)^2}{2\sigma^2}\right)\mathrm{d}x && \text{(D.9)}\\
&= \frac{1}{4\sqrt{2\pi}\sigma}\frac{1}{\sqrt[4]{z^3}}\left[\exp\left(-\frac{(\sqrt[4]{z}-\mu)^2}{2\sigma^2}\right)+\exp\left(-\frac{(\sqrt[4]{z}+\mu)^2}{2\sigma^2}\right)\right] \quad (z \geqq 0). && \text{(D.10)}
\end{aligned}
$$

Distributions of $f_1(x)$, $f_2(x)$, $f_3(x)$, and $f_4(x)$ with $\mu = 1.0$ and $\sigma = 0.1$ are shown in Fig. D.1. The distribution of $f_n(x)$ $(n \geq 2)$ is not a Gaussian distribution, and has skewness and kurtosis. For this reason, the mass spectrum, which is calculated by the several observables expected to follow Gaussian distributions, has skewness and kurtosis.

Since the distribution of $f_n(x)$ $(n \geq 2)$ has skewness, the maximum value of the distribution is not equal to the mean value. The mean of a distribution $f_n(x)$ is given by

$$E_n = \int_{-\infty}^{\infty} x f_n(x)\mathrm{d}x. \tag{D.11}$$

For $n = 2$, 3 and 4, we obtain

$$
\begin{aligned}
E_2 &= \sigma^2 + \mu^2, && \text{(D.12)}\\
E_3 &= 3\mu\sigma^2 + \mu^3, && \text{(D.13)}\\
E_4 &= 3\sigma^4 + 6\mu^2\sigma^2 + \mu^4. && \text{(D.14)}
\end{aligned}
$$

In Fig. D.1, the mean of each distribution is drawn by a dashed line.

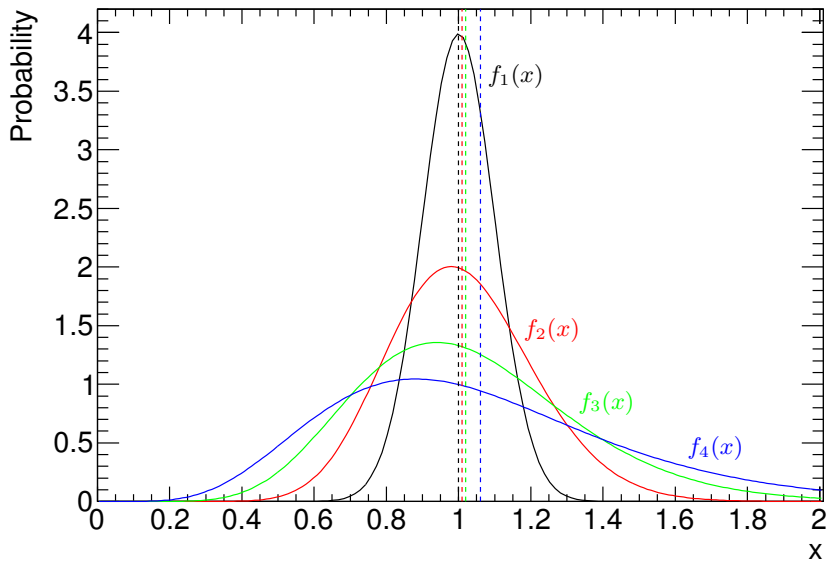

Figure D.1: Distributions of the probability density functions $f_1(x)$ (black), $f_2(x)$ (red), $f_3(x)$ (green), and $f_4(x)$ (blue) with $\mu = 1.0$ and $\sigma = 0.1$. The expected value of each distribution is shown in the dashed line with the same color.

Appendix E

Shift of deduced mass values

Here, we discuss the shift of the deduced masses mentioned in Sec. 3.3.4. Figure E.1 shows the TOF shift for ^{45}Cl. To select fragments with the similar trajectories, the TOF spectrum for ^{45}Cl was gated by $|x_3 - 6.0| < 1$ mm, $|a_3 - 3.0| < 1$ mrad, and $|x_0 - 55.0| < 10$ mm. The TOF shift shows the similar behavior to those of the deduced masses shown in Fig. 3.25, and this suggests that the mass shift was caused by the TOF shift. During the experiment, we measured temperature with several thermometers in the experimental vault and the counting room, and magnetic field values of the dipole and quadrupole magnets along the beam line. We discuss below the effects of the changes in temperature and magnetic field on the mass shift or TOF shift.

First, let us consider the temperature. Figure E.2 shows the shift of the temperature in the SHARAQ counting room varying by $\sim$1°C throughout the experiment. The temperature change is similar to the shift of the deduced masses in Fig. 3.25, and the other thermometers except for those located near the SHARAQ counting room do not show such a trend. This implies that the shift of the masses is related to the temperature variation in the counting area. In the counting area, there are the TDC module for the TOF measurement and optical fiber cables in which the timing signals are transferred (see Fig. 2.6). Thus, the temperature dependence of the apparatus for the TOF measurement located in the counting area can be a possible source of the mass shift. However, since the shift due to the thermal extension of an optical fiber cable is at most a few picoseconds, the temperature dependence of the optical fiber cable is not so large to cause the TOF shift by $\sim$30 ps shown in Fig. E.1. The TOF shift cannot be accounted for only by the response of the timing electronics due to the temperature variation.

Another possible reason of the mass shift is the magnetic field variation. Figure E.3 shows the shift of the magnetic field of SD2, the second dipole magnet of SHARAQ (see Fig. 2.1). The magnetic field changes just before the run #364 and after #393, and the trend of its variation agrees with the shift of the deduced masses. The other dipole and quadrupole magnets do not show such a trend. It is therefore suggested that the magnetic field variation at SD2 caused the change of the flight length or TOF of an ion, and the shift of its deduced mass.

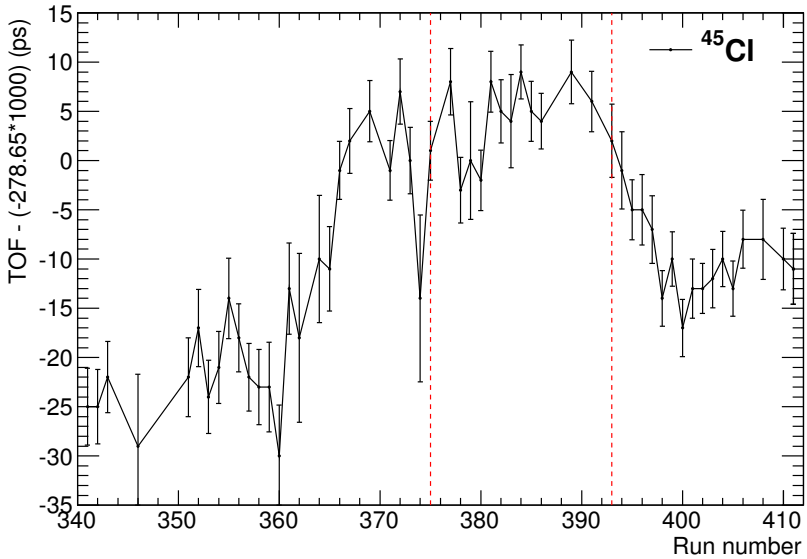

Figure E.1: Shift of the TOF values for ^{45}Cl as a function of the run number in the experiment. The TOF value is the mean of the TOF spectrum gated by $|x_3 - 6.0| < 1$ mm, $|a_3 - 3.0| < 1$ mrad, and $|x_0 - 55.0| < 10$ mm. The TOF values subtracted by -278.65 ns are plotted.

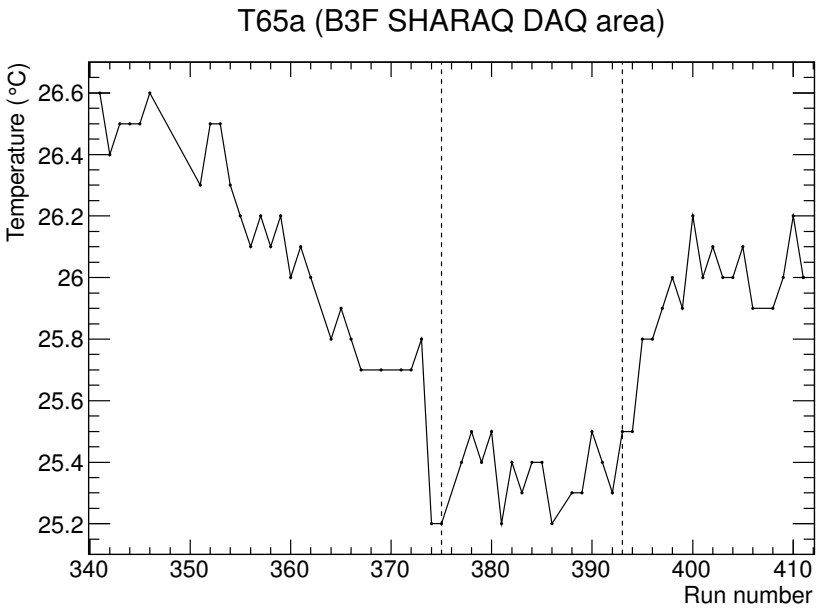

Figure E.2: Temperature change in the SHARAQ DAQ area as a function of the run number in the experiment.

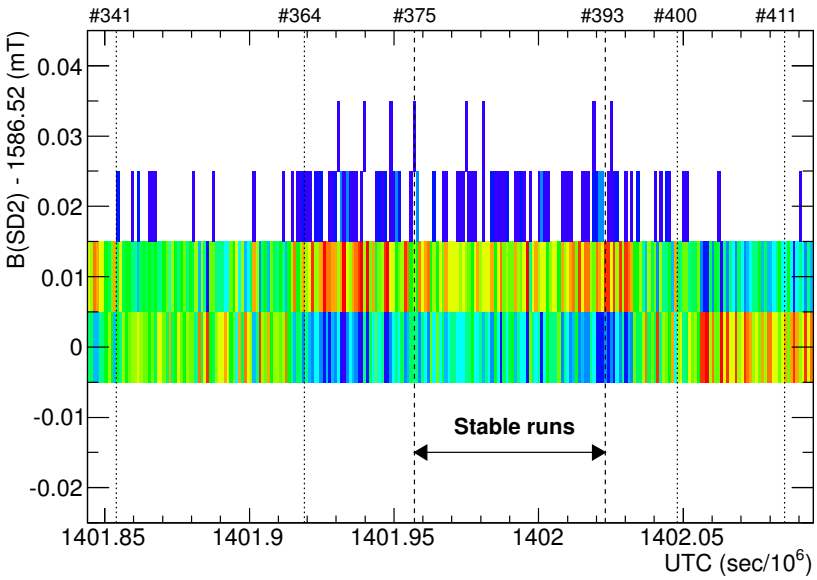

Figure E.3: Change in the magnetic field at SD2. The vertical axis shows the value subtracted by 1586.52 mT. The horizontal axis represents the Unix time (UTC).

Appendix F

Uncertainties related to the fitting

Here, we describe in detail the uncertainty related to the mass fitting δ_{fit}, which was introduced in Sec. 3.3.6.

F.1 Expression of δ_{fit}

Discussion in this section is based on Ref. [103]. We define the calibration function by

$$y = f(x) \equiv \sum_j a_j h_j(x), \tag{F.1}$$

where a_j is the fitting parameters. The uncertainty δ_{fit} is calculated from the error propagation equation for $f(x)$ as

$$\begin{aligned} \delta_{\text{fit}}^2 &= \sum_j \left[\sigma_{a_j}^2 \left(\frac{\partial f(x)}{\partial a_j} \right)^2 \right] + \sum_{j \neq k} \left[\sigma_{a_j a_k}^2 \frac{\partial f(x)}{\partial a_j} \frac{\partial f(x)}{\partial a_k} \right] \\ &= \sum_j \left[\sigma_{a_j}^2 \left(h_j(x) \right)^2 \right] + \sum_{j \neq k} \left[\sigma_{a_j a_k}^2 h_j(x) h_k(x) \right], \end{aligned} \tag{F.2}$$

where $\sigma_{a_j}^2$ and $\sigma_{a_j a_k}^2$ are variances and covariances of the fit parameters, respectively. The covariance of the two parameters a_j and a_k, $\sigma_{a_j a_k}$, which also gives the variance for $j = k$, is given by

$$\sigma_{a_j a_k}^2 = \sum_i \left[\sigma_i^2 \frac{\partial a_j}{\partial y_i} \frac{\partial a_k}{\partial y_i} \right] \tag{F.3}$$

$$= (\boldsymbol{V}^{-1})_{jk}, \tag{F.4}$$

where y_i is the i-th data point corresponding to $x = x_i$, σ_i is the uncertainty of y_i, and $\boldsymbol{V}$ is the covariance matrix defined by

$$\boldsymbol{V}_{jk} \equiv \sum_i \left[\frac{1}{\sigma_i^2} h_j(x) h_k(x) \right]. \tag{F.5}$$

Here, we briefly show the derivation of Eq. (F.4). The χ^2 value is defined by

$$\chi^2 = \sum_i \left[\frac{1}{\sigma_i} \left(y_i - \sum_{j=1}^{m} a_j h_j(x_i) \right) \right]^2 . \tag{F.6}$$

Since the least-squares method requires that we minimize χ^2, we obtain

$$\frac{\partial \chi^2}{\partial a_l} = -2 \sum_i \left[\frac{h_l(x_i)}{\sigma_i^2} \left(y_i - \sum_{j=1}^{m} a_j h_j(x_i) \right) \right] = 0. \tag{F.7}$$

To express Eq. (F.7) in matrix form, we define the row matrix $\boldsymbol{\beta}$, the symmetric matrix $\boldsymbol{\alpha}$, and the row matrix $\boldsymbol{a}$ as follows:

$$\boldsymbol{\beta}_k \equiv \sum_i \left[\frac{1}{\sigma_i^2} y_i h_k(x_i) \right], \tag{F.8}$$

$$\boldsymbol{\alpha}_{lk} \equiv \sum_i \left[\frac{1}{\sigma_i^2} h_l(x_i) h_k(x_i) \right], \tag{F.9}$$

$$\boldsymbol{a} \equiv (a_1, \ldots, a_m). \tag{F.10}$$

The matrix $\boldsymbol{\alpha}$ is identical to the matrix $\boldsymbol{V}$ defined in Eq. (F.5). Eq. (F.7) leads to

$$\boldsymbol{\beta} = \boldsymbol{a}\boldsymbol{\alpha}. \tag{F.11}$$

Therefore, the parameters of the fit are expressed as

$$a_l = \sum_{j=1}^{m} \left[(\boldsymbol{\alpha}^{-1})_{jl} \sum_i \left(\frac{1}{\sigma_i^2} y_i h_j(x_i) \right) \right], \tag{F.12}$$

and the derivatives of a_l with respect to y_i are written as

$$\frac{\partial a_l}{\partial y_i} = \sum_{j=1}^{m} \left[(\boldsymbol{\alpha}^{-1})_{jl} \frac{1}{\sigma_i^2} h_j(x_i) \right]. \tag{F.13}$$

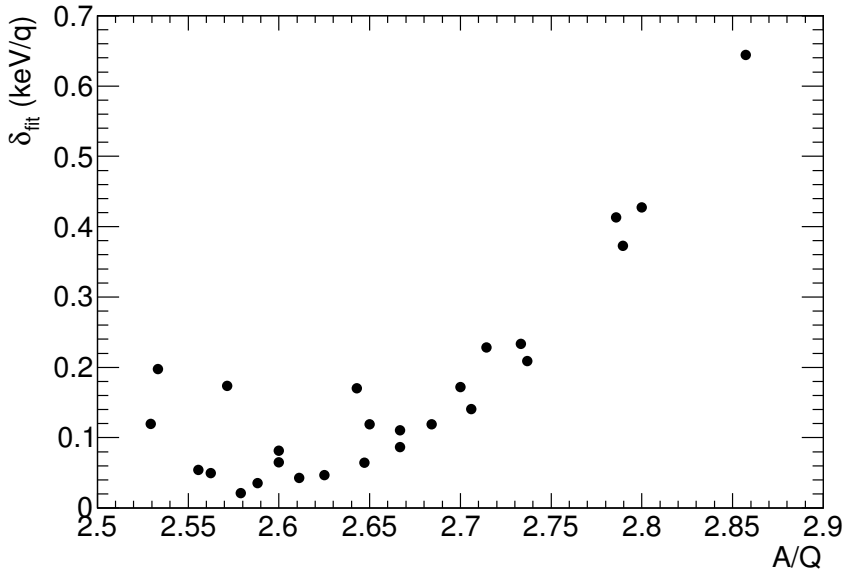

Figure F.1: Evaluated $\delta_{\rm fit}$ values as a function of A/Q.

Substituting these derivatives into Eq. (F.3), we obtain Eq. (F.4) as follows:

$$\begin{aligned}
\sigma^2_{a_j a_k} &= \sum_i \left[\sigma_i^2 \frac{\partial a_j}{\partial y_i} \frac{\partial a_k}{\partial y_i} \right] \\
&= \sum_i \left[\sigma_i^2 \sum_{p=1}^{m} \left((\boldsymbol{\alpha}^{-1})_{pj} \frac{1}{\sigma_i^2} h_p(x_i) \right) \sum_{q=1}^{m} \left((\boldsymbol{\alpha}^{-1})_{qk} \frac{1}{\sigma_i^2} h_q(x_i) \right) \right] \\
&= \sum_{p=1}^{m} \left((\boldsymbol{\alpha}^{-1})_{pj} \sum_{q=1}^{m} \left[(\boldsymbol{\alpha}^{-1})_{qk} \sum_i \left(\frac{1}{\sigma_i^2} h_p(x_i) h_q(x_i) \right) \right] \right) \\
&= \sum_{p=1}^{m} \left((\boldsymbol{\alpha}^{-1})_{pj} \sum_{q=1}^{m} \left[(\boldsymbol{\alpha}^{-1})_{qk} \cdot \boldsymbol{\alpha}_{pq} \right] \right) \\
&= \sum_{p=1}^{m} \left((\boldsymbol{\alpha}^{-1})_{pj} \cdot \mathbf{1}_{pk} \right) \\
&= (\boldsymbol{\alpha}^{-1})_{kj}. \qquad \text{(F.14)}
\end{aligned}$$

F.2 Evaluation of $\delta_{\rm fit}$ values in the present measurements

We evaluated the $\delta_{\rm fit}$ values for the reference nuclei in the mass calibration using Eq. (F.2). Figure F.1 shows the evaluated $\delta_{\rm fit}$ values as a function of A/Q.

Next, we evaluate the contribution of $\delta_{\rm fit}$ to the total uncertainty of the deduced mass, which consists of $\delta_{\rm stat}$, $\delta_{\rm syst}$, $\delta_{Z\rm cor}$, and $\delta_{\rm fit}$. As described in Sec. 3.3.6, $\delta_{\rm syst} = 6.1$ keV/q has the majority in the total uncertainty. On the other hand, $\delta_{\rm fit}$, which is less than 0.7 keV/q, is

much smaller than $\delta_{\rm syst}$. Then, the following inequality is obtained:

$$\begin{aligned}
\frac{\delta^2_{\rm stat}+\delta^2_{\rm syst}+\delta^2_{Z{\rm cor}}+\delta^2_{\rm fit}}{\delta^2_{\rm stat}+\delta^2_{\rm syst}+\delta^2_{Z{\rm cor}}} &= 1+\frac{\delta^2_{\rm fit}}{\delta^2_{\rm stat}+\delta^2_{\rm syst}+\delta^2_{Z{\rm cor}}} && \text{(F.15)}\\
&< 1+\frac{\delta^2_{\rm fit}}{\delta^2_{\rm syst}} && \text{(F.16)}\\
&< 1+\frac{0.7^2}{6.1^2} && \text{(F.17)}\\
&= 1.013. && \text{(F.18)}
\end{aligned}$$

Therefore, the contribution of $\delta_{\rm fit}$ to the total uncertainty is evaluated as

$$\frac{\left(\delta^2_{\rm stat}+\delta^2_{\rm syst}+\delta^2_{Z{\rm cor}}+\delta^2_{\rm fit}\right)^{1/2}}{\left(\delta^2_{\rm stat}+\delta^2_{\rm syst}+\delta^2_{Z{\rm cor}}\right)^{1/2}} < \sqrt{1.013} = 1.007. \tag{F.19}$$

The uncertainty $\delta_{\rm fit}$ is negligible as it accounts for at most 0.7% of the total uncertainty. Noted that $\delta_{\rm fit}$ is negligible even for the nuclei whose masses are determined by extrapolation.

Appendix G

Uncertainties related to the Z correction

In this chapter, derivation of the uncertainties originating from the Z correction is described. As described in Sec. 3.3.5, the following function was employed in the Z correction:

$$f(Z) \equiv \left(\frac{m}{q}\right)_{\text{exp}} - \left(\frac{m}{q}\right)_{\text{ref}} = p_0(Z-p_1)^2 + p_2, \tag{G.1}$$

where $(m/q)_{\text{exp}}$ is the deduced mass-to-charge ratio, $(m/q)_{\text{ref}}$ is the literature one, and p_0, p_1, and p_2 are the fitting parameters. Using the covariance matrix $\boldsymbol{V}$ of the parameters, p_0, p_1, and p_2, the uncertainty in the calculated value of $f(Z)$, $\delta f(Z)$, is given by

$$\begin{aligned}
(\delta f(Z))^2 &= \left(\frac{\partial f}{\partial p_0}\right)^2 \boldsymbol{V}_{00} + \left(\frac{\partial f}{\partial p_1}\right)^2 \boldsymbol{V}_{11} + \left(\frac{\partial f}{\partial p_2}\right)^2 \boldsymbol{V}_{22} \\
&\quad +2\left(\frac{\partial f}{\partial p_0}\right)\left(\frac{\partial f}{\partial p_1}\right)\boldsymbol{V}_{01} + 2\left(\frac{\partial f}{\partial p_0}\right)\left(\frac{\partial f}{\partial p_2}\right)\boldsymbol{V}_{02} + 2\left(\frac{\partial f}{\partial p_1}\right)\left(\frac{\partial f}{\partial p_2}\right)\boldsymbol{V}_{12} \\
&= (Z-p_1)^4\boldsymbol{V}_{00} + 4p_0^2(Z-p_1)^2\boldsymbol{V}_{11} + \boldsymbol{V}_{22} \\
&\quad -4p_0(Z-p_1)^3\boldsymbol{V}_{01} + 2(Z-p_1)^2\boldsymbol{V}_{02} - 4p_0(Z-p_1)\boldsymbol{V}_{12}.
\end{aligned} \tag{G.2}$$

Tables G.1 and G.2 summarize the uncertainty originating from the Z correction, $\delta_{Z\text{cor}}$, for each Z in the ^{55}Ca and ^{52}Ca settings, respectively.

Table G.1: Uncertainties originating from the Z correction for each Z number in the ^{55}Ca setting.

Z	$\delta f(Z)$ (keV/q)	$\delta_{Z\mathrm{cor}}$ (keV)
23	13.3	305
22	9.08	200
21	5.72	120
20	3.26	65
19	1.96	37
18	1.85	33
17	1.95	33
16	1.68	27
15	1.31	20
14	2.26	32

Table G.2: Uncertainties originating from the Z correction for each Z number in the ^{52}Ca setting.

Z	$\delta f(Z)$ (keV/q)	$\delta_{Z\mathrm{cor}}$ (keV)
24	7.98	191
23	5.38	124
22	4.50	99
21	4.51	95
20	4.36	87
19	3.68	70
18	2.85	51
17	3.74	63

Appendix H

A/Q spectrum for each Z

The A/Q spectrum deduced from the present experiment for each isotopic chain is presented. Figures H.1 and H.2 show the spectra in the ^{55}Ca setting for the isotopes from $Z = 23$ (V) to $Z = 14$ (Si), while Figs. H.3 and H.4 show those in the ^{52}Ca setting for the isotopes from $Z = 24$ (Cr) to $Z = 17$ (Cl).

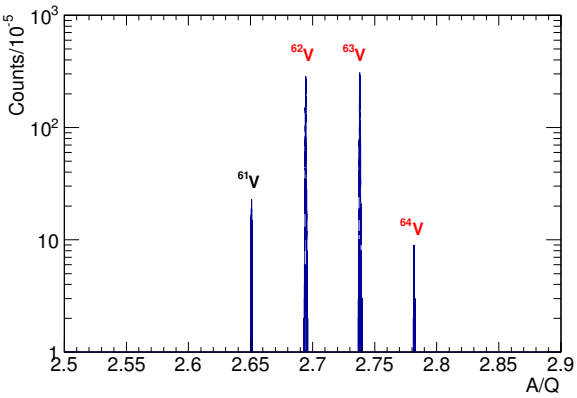

(a) $Z = 23$ (V)

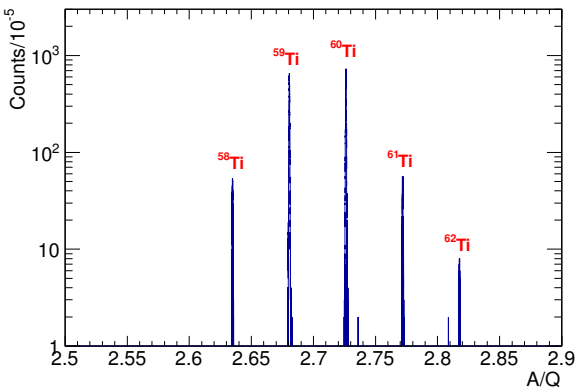

(b) $Z = 22$ (Ti)

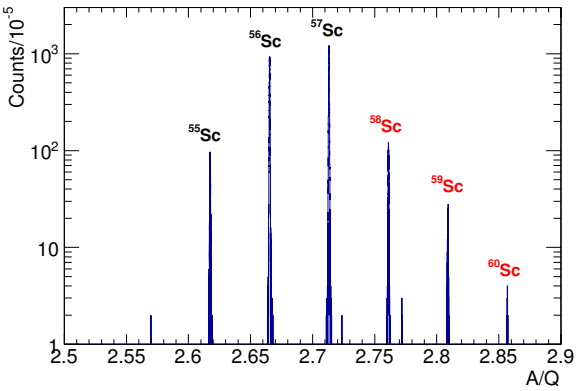

(c) $Z = 21$ (Sc)

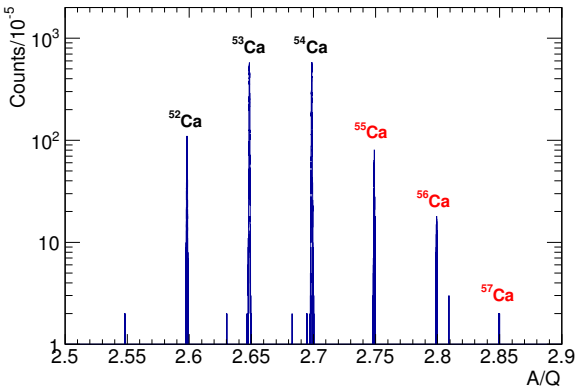

(d) $Z = 20$ (Ca)

Figure H.1: A/Q spectrum deduced from the present experiment in the ^{55}Ca setting from $Z = 20$ (Ca) to $Z = 23$ (V) isotopes. Nuclei whose masses have not been measured previously are indicated with red letters.

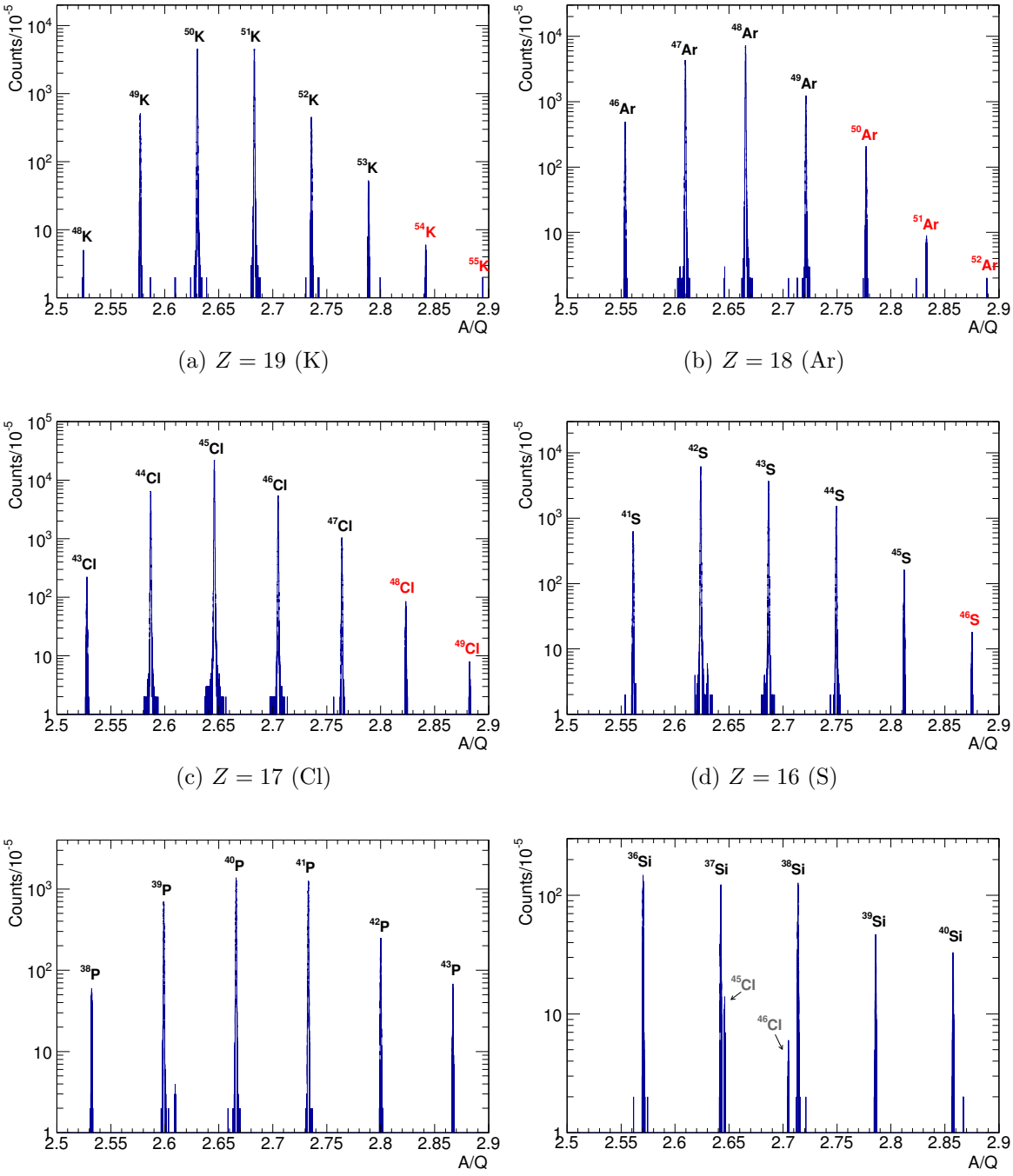

(a) $Z = 19$ (K)

(b) $Z = 18$ (Ar)

(c) $Z = 17$ (Cl)

(d) $Z = 16$ (S)

(e) $Z = 15$ (P)

(f) $Z = 14$ (Si)

Figure H.2: The same as Fig. H.1, but from $Z = 14$ (Si) to $Z = 19$ (K) isotopes.

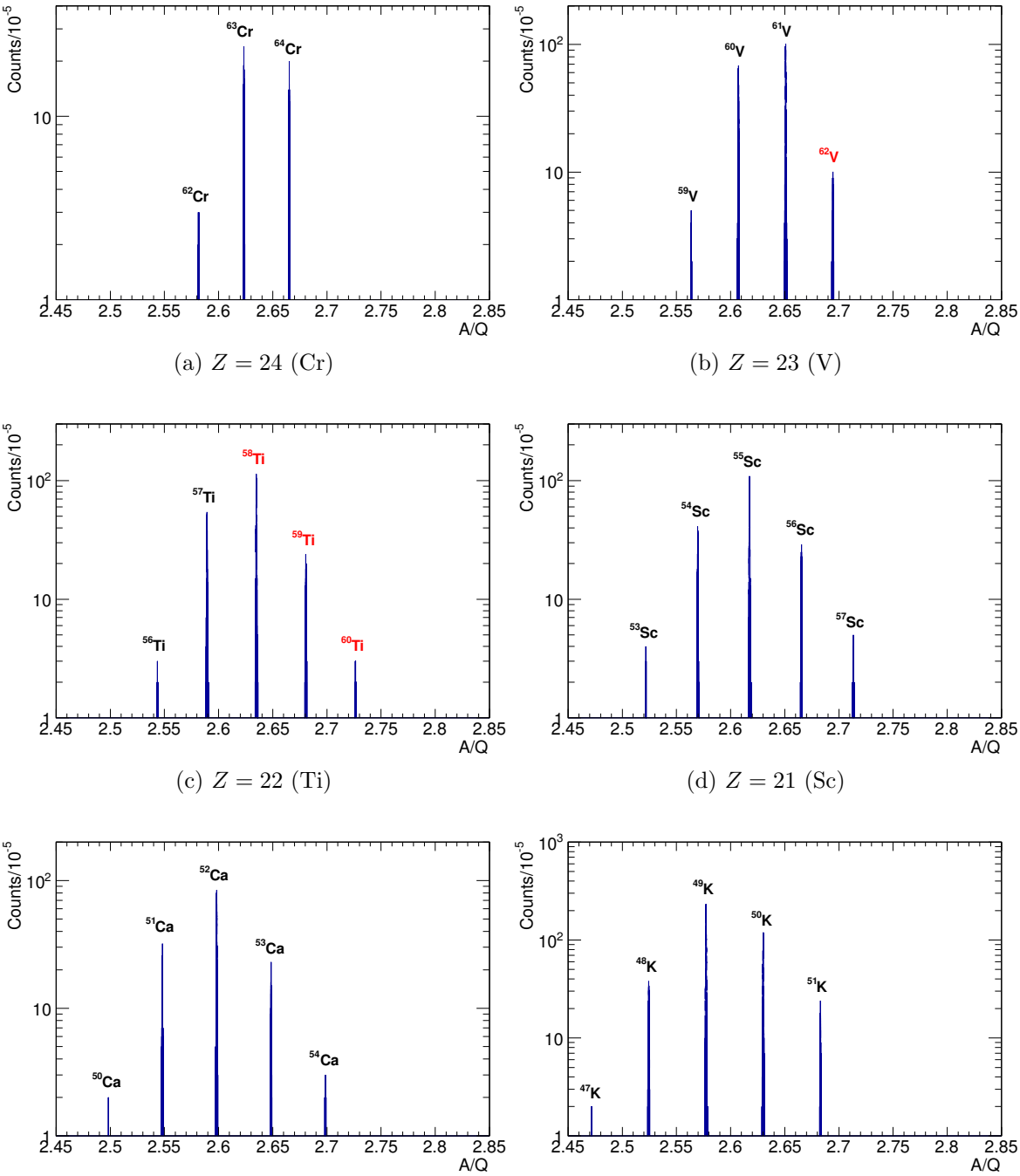

(a) $Z = 24$ (Cr)

(b) $Z = 23$ (V)

(c) $Z = 22$ (Ti)

(d) $Z = 21$ (Sc)

(e) $Z = 20$ (Ca)

(f) $Z = 19$ (K)

Figure H.3: A/Q spectrum deduced from the present experiment in the ^{52}Ca setting from $Z = 20$ (Ca) to $Z = 23$ (V) isotopes. Nuclei whose masses have not been measured previously are indicated with red letters.

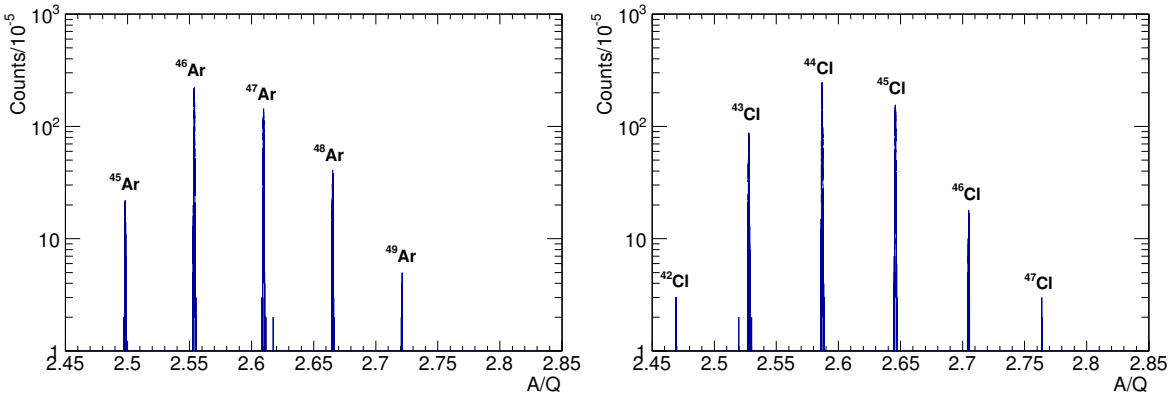

(a) $Z = 18$ (Ar) (b) $Z = 17$ (Cl)

Figure H.4: The same as Fig. H.3, but from $Z = 20$ (Ca) to $Z = 23$ (V) isotopes.

Bibliography

[1] A. Einstein, "Ist die Trägheit eines Körpers von seinem Energieinhalt abhängig?", Annalen der Physik **323**, 639 (1905).

[2] F. W. Aston, "Isotopes and Atomic Weights", Nature **105**, 617 (1920).

[3] W. M. Elsasser, "Sur le principe de Pauli dans les noyaux", Journal de Physique et Le Radium **4**, 549 (1933).

[4] M. G. Mayer, "On Closed Shells in Nuclei", Physical Review **74**, 235 (1948).

[5] M. G. Mayer, "On Closed Shells in Nuclei. II", Physical Review **75**, 1969 (1949).

[6] O. Haxel, J. H. D. Jensen, and H. E. Suess, "On the "Magic Numbers" in Nuclear Structure", Physical Review **75**, 1766 (1949).

[7] O. Sorlin and M.-G. Porquet, "Nuclear magic numbers: New features far from stability", Progress in Particle and Nuclear Physics **61**, 602 (2008).

[8] T. Otsuka, "Exotic nuclei and nuclear forces", Physica Scripta **T152**, 014007 (2013).

[9] A. Navin, D. W. Anthony, T. Aumann, T. Baumann, D. Bazin, Y. Blumenfeld, B. A. Brown, T. Glasmacher, P. G. Hansen, R. W. Ibbotson, P. A. Lofy, V. Maddalena, K. Miller, T. Nakamura, B. V. Pritychenko, B. M. Sherrill, E. Spears, M. Steiner, J. A. Tostevin, J. Yurkon, and A. Wagner, "Direct evidence for the breakdown of the $N = 8$ shell closure in ^{12}Be", Physical Review Letters **85**, 266 (2000).

[10] H. Iwasaki, T. Motobayashi, H. Akiyoshi, Y. Ando, N. Fukuda, H. Fujiwara, Z. Fülöp, K. I. Hahn, Y. Higurashi, M. Hirai, I. Hisanaga, N. Iwasa, T. Kijima, T. Minemura, T. Nakamura, M. Notani, S. Ozawa, H. Sakurai, S. Shimoura, S. Takeuchi, T. Teranishi, Y. Yanagisawa, and M. Ishihara, "Quadrupole deformation of ^{12}Be studied by proton inelastic scattering", Physics Letters B **481**, 7 (2000).

[11] H. Iwasaki, T. Motobayashi, H. Akiyoshi, Y. Ando, N. Fukuda, H. Fujiwara, Z. Fülöp, K. I. Hahn, Y. Higurashi, M. Hirai, I. Hisanaga, N. Iwasa, T. Kijima, A. Mengoni, T. Minemura, T. Nakamura, M. Notani, S. Ozawa, H. Sagawa, H. Sakurai, S. Shimoura, S. Takeuchi, T. Teranishi, Y. Yanagisawa, and M. Ishihara, "Low-lying intruder 1^- state in ^{12}Be and the melting of the $N = 8$ shell closure", Physics Letters B **491**, 8 (2000).

[12] S. Shimoura, A. Saito, T. Minemura, Y. U. Matsuyama, H. Baba, H. Akiyoshi, N. Aoi, T. Gomi, Y. Higurashi, K. Ieki, N. Imai, N. Iwasa, H. Iwasaki, S. Kanno, S. Kubono, M. Kunibu, S. Michimasa, T. Motobayashi, T. Nakamura, H. Sakurai, M. Serata, E. Takeshita, S. Takeuchi, T. Teranishi, K. Ue, K. Yamada, Y. Yanagisawa, M. Ishihara, and N. Itagaki, "Isomeric 0^+ state in ^{12}Be", Physics Letters B **560**, 31 (2003).

[13] T. Motobayashi, Y. Ikeda, K. Ieki, M. Inoue, N. Iwasa, T. Kikuchi, M. Kurokawa, S. Moriya, S. Ogawa, H. Murakami, S. Shimoura, Y. Yanagisawa, T. Nakamura, Y. Watanabe, M. Ishihara, T. Teranishi, H. Okuno, and R. Casten, "Large deformation of the very neutron-rich nucleus ^{32}Mg from intermediate-energy Coulomb excitation", Physics Letters B **346**, 9 (1995).

[14] E. K. Warburton, J. A. Becker, and B. A. Brown, "Mass systematics for $A = 29$–44 nuclei: The deformed $A \sim 32$ region", Physical Review C **41**, 1147 (1990).

[15] B. Bastin, S. Grévy, D. Sohler, O. Sorlin, Z. Dombrádi, N. Achouri, J. Angélique, F. Azaiez, D. Baiborodin, R. Borcea, C. Bourgeois, A. Buta, A. Bürger, R. Chapman, J. Dalouzy, Z. Dlouhy, A. Drouard, Z. Elekes, S. Franchoo, S. Iacob, B. Laurent, M. Lazar, X. Liang, E. Liénard, J. Mrazek, L. Nalpas, F. Negoita, N. Orr, Y. Penionzhkevich, Z. Podolyák, F. Pougheon, P. Roussel-Chomaz, M. Saint-Laurent, M. Stanoiu, I. Stefan, F. Nowacki, and A. Poves, "Collapse of the $N = 28$ Shell Closure in ^{42}Si", Physical Review Letters **99**, 022503 (2007).

[16] S. Takeuchi, M. Matsushita, N. Aoi, P. Doornenbal, K. Li, T. Motobayashi, H. Scheit, D. Steppenbeck, H. Wang, H. Baba, D. Bazin, L. Càceres, H. Crawford, P. Fallon, R. Gernhäuser, J. Gibelin, S. Go, S. Grévy, C. Hinke, C. R. Hoffman, R. Hughes, E. Ideguchi, D. Jenkins, N. Kobayashi, Y. Kondo, R. Krücken, T. Le Bleis, J. Lee, G. Lee, A. Matta, S. Michimasa, T. Nakamura, S. Ota, M. Petri, T. Sako, H. Sakurai, S. Shimoura, K. Steiger, K. Takahashi, M. Takechi, Y. Togano, R. Winkler, and K. Yoneda, "Well developed deformation in ^{42}Si", Physical Review Letters **109**, 182501 (2012).

[17] R. Kanungo, C. Nociforo, A. Prochazka, T. Aumann, D. Boutin, D. Cortina-Gil, B. Davids, M. Diakaki, F. Farinon, H. Geissel, R. Gernhäuser, J. Gerl, R. Janik, B. Jonson, B. Kindler, R. Knöbel, R. Krücken, M. Lantz, H. Lenske, Y. Litvinov, B. Lommel, K. Mahata, P. Maierbeck, A. Musumarra, T. Nilsson, T. Otsuka, C. Perro, C. Scheidenberger, B. Sitar, P. Strmen, B. Sun, I. Szarka, I. Tanihata, Y. Utsuno, H. Weick, and M. Winkler, "One-Neutron Removal Measurement Reveals ^{24}O as a New Doubly Magic Nucleus", Physical Review Letters **102**, 152501 (2009).

[18] C. Hoffman, T. Baumann, D. Bazin, J. Brown, G. Christian, D. Denby, P. DeYoung, J. Finck, N. Frank, J. Hinnefeld, S. Mosby, W. Peters, W. Rogers, A. Schiller, A. Spyrou, M. Scott, S. Tabor, M. Thoennessen, and P. Voss, "Evidence for a doubly magic ^{24}O", Physics Letters B **672**, 17 (2009).

[19] D. Suzuki, H. Iwasaki, D. Beaumel, L. Nalpas, E. Pollacco, M. Assié, H. Baba, Y. Blumenfeld, N. De Séréville, A. Drouart, S. Franchoo, A. Gillibert, J. Guillot, F. Hammache, N. Keeley, V. Lapoux, F. Maréchal, S. Michimasa, X. Mougeot, I. Mukha, H. Okamura, H. Otsu, A. Ramus, P. Roussel-Chomaz, H. Sakurai, J. A. Scarpaci, O. Sorlin, I. Stefan,

and M. Takechi, "Breakdown of the $Z = 8$ shell closure in unbound ^{12}O and its mirror symmetry", Physical Review Letters **103**, 152503 (2009).

[20] A. Huck, G. Klotz, A. Knipper, C. Miehé, C. Richard-Serre, G. Walter, A. Poves, H. L. Ravn, and G. Marguier, "Beta decay of the new isotopes ^{52}K, ^{52}Ca, and ^{52}Sc; a test of the shell model far from stability", Physical Review C **31**, 2226 (1985).

[21] A. Gade, R. V. F. Janssens, D. Bazin, R. Broda, B. A. Brown, C. M. Campbell, M. P. Carpenter, J. M. Cook, A. N. Deacon, D. C. Dinca, B. Fornal, S. J. Freeman, T. Glasmacher, P. G. Hansen, B. P. Kay, P. F. Mantica, W. F. Mueller, J. R. Terry, J. A. Tostevin, and S. Zhu, "Cross-shell excitation in two-proton knockout: Structure of ^{52}Ca", Physical Review C **74**, 021302(R) (2006).

[22] R. V. F. Janssens, B. Fornal, P. F. Mantica, B. A. Brown, R. Broda, P. Bhattacharyya, M. P. Carpenter, M. Cinausero, P. J. Daly, A. D. Davies, T. Glasmacher, Z. W. Grabowski, D. E. Groh, M. Honma, F. G. Kondev, W. Królas, T. Lauritsen, S. N. Liddick, S. Lunardi, N. Marginean, T. Mizusaki, D. J. Morrissey, A. C. Morton, W. F. Mueller, T. Otsuka, T. Pawlat, D. Seweryniak, H. Schatz, A. Stolz, S. L. Tabor, C. A. Ur, G. Viesti, I. Wiedenhöver, and J. Wrzesiński, "Structure of ^{52,54}Ti and shell closures in neutron-rich nuclei above ^{48}Ca", Physics Letters B **546**, 55 (2002).

[23] D.-C. Dinca, R. V. F. Janssens, A. Gade, D. Bazin, R. Broda, B. A. Brown, C. M. Campbell, M. P. Carpenter, P. Chowdhury, J. M. Cook, A. N. Deacon, B. Fornal, S. J. Freeman, T. Glasmacher, M. Honma, F. G. Kondev, J.-L. Lecouey, S. N. Liddick, P. F. Mantica, W. F. Mueller, H. Olliver, T. Otsuka, J. R. Terry, B. A. Tomlin, and K. Yoneda, "Reduced transition probabilities to the first 2^+ state in ^{52,54,56}Ti and development of shell closures at $N = 32, 34$", Physical Review C **71**, 041302(R) (2005).

[24] J. Prisciandaro, P. Mantica, B. Brown, D. Anthony, M. Cooper, A. Garcia, D. Groh, A. Komives, W. Kumarasiri, P. Lofy, A. Oros-Peusquens, S. Tabor, and M. Wiedeking, "New evidence for a subshell gap at $N = 32$", Physics Letters B **510**, 17 (2001).

[25] A. Bürger, T. R. Saito, H. Grawe, H. Hübel, P. Reiter, J. Gerl, M. Górska, H. J. Wollersheim, A. Al-Khatib, A. Banu, T. Beck, F. Becker, P. Bednarczyk, G. Benzoni, A. Bracco, S. Brambilla, P. Bringel, F. Camera, E. Clément, P. Doornenbal, H. Geissel, A. Görgen, J. Grebosz, G. Hammond, M. Hellström, M. Honma, M. Kavatsyuk, O. Kavatsyuk, M. Kmiecik, I. Kojouharov, W. Korten, N. Kurz, R. Lozeva, A. Maj, S. Mandal, B. Million, S. Muralithar, A. Neußer, F. Nowacki, T. Otsuka, Z. Podolyák, N. Saito, A. K. Singh, H. Weick, C. Wheldon, O. Wieland, M. Winkler, and RISING Collaboration, "Relativistic Coulomb excitation of neutron-rich ^{54,56,58}Cr: On the pathway of magicity from $N = 40$ to $N = 32$", Physics Letters B **622**, 29 (2005).

[26] A. T. Gallant, J. C. Bale, T. Brunner, U. Chowdhury, S. Ettenauer, A. Lennarz, D. Robertson, V. V. Simon, A. Chaudhuri, J. D. Holt, A. A. Kwiatkowski, E. Mané, J. Menéndez, B. E. Schultz, M. C. Simon, C. Andreoiu, P. Delheij, M. R. Pearson, H. Savajols, A. Schwenk, and J. Dilling, "New precision mass measurements of neutron-rich calcium and potassium isotopes and three-nucleon forces", Physical Review Letters **109**, 032506 (2012).

[27] F. Wienholtz, D. Beck, K. Blaum, C. Borgmann, M. Breitenfeldt, R. B. Cakirli, S. George, F. Herfurth, J. D. Holt, M. Kowalska, S. Kreim, D. Lunney, V. Manea, J. Menéndez, D. Neidherr, M. Rosenbusch, L. Schweikhard, A. Schwenk, J. Simonis, J. Stanja, R. N. Wolf, and K. Zuber, "Masses of exotic calcium isotopes pin down nuclear forces", Nature **498**, 346 (2013).

[28] M. Rosenbusch, P. Ascher, D. Atanasov, C. Barbieri, D. Beck, K. Blaum, C. Borgmann, M. Breitenfeldt, R. B. Cakirli, A. Cipollone, S. George, F. Herfurth, M. Kowalska, S. Kreim, D. Lunney, V. Manea, P. Navrátil, D. Neidherr, L. Schweikhard, V. Somà, J. Stanja, F. Wienholtz, R. N. Wolf, and K. Zuber, "Probing the $N = 32$ Shell Closure below the Magic Proton Number $Z = 20$: Mass Measurements of the Exotic Isotopes ^{52,53}K", Physical Review Letters **114**, 202501 (2015).

[29] D. Steppenbeck, S. Takeuchi, N. Aoi, P. Doornenbal, M. Matsushita, H. Wang, Y. Utsuno, H. Baba, S. Go, J. Lee, K. Matsui, S. Michimasa, T. Motobayashi, D. Nishimura, T. Otsuka, H. Sakurai, Y. Shiga, N. Shimizu, P.-A. Söderström, T. Sumikama, R. Taniuchi, J. J. Valiente-Dobón, and K. Yoneda, "Low-Lying Structure of ^{50}Ar and the $N = 32$ Subshell Closure", Physical Review Letters **114**, 252501 (2015).

[30] T. Otsuka, R. Fujimoto, Y. Utsuno, B. A. Brown, M. Honma, and T. Mizusaki, "Magic Numbers in Exotic Nuclei and Spin-Isospin Properties of the NN Interaction", Physical Review Letters **87**, 082502 (2001).

[31] M. Honma, T. Otsuka, B. A. Brown, and T. Mizusaki, "Effective interaction for pf-shell nuclei", Physical Review C **65**, 061301(R) (2002).

[32] S. N. Liddick, P. F. Mantica, R. V. F. Janssens, R. Broda, B. A. Brown, M. P. Carpenter, B. Fornal, M. Honma, T. Mizusaki, A. C. Morton, W. F. Mueller, T. Otsuka, J. Pavan, A. Stolz, S. L. Tabor, B. E. Tomlin, and M. Wiedeking, "Lowest Excitations in ^{56}Ti and the Predicted $N = 34$ Shell Closure", Physical Review Letters **92**, 072502 (2004).

[33] R. V. F. Janssens, "Elusive magic numbers", Nature **435**, 897 (2005).

[34] M. Rejmund, S. Bhattacharyya, A. Navin, W. Mittig, L. Gaudefroy, M. Gelin, G. Mukherjee, F. Rejmund, P. Roussel-Chomaz, and C. Theisen, "Shell evolution and the $N = 34$ "magic number"", Physical Review C **76**, 021304(R) (2007).

[35] H. L. Crawford, R. V. F. Janssens, P. F. Mantica, J. S. Berryman, R. Broda, M. P. Carpenter, N. Cieplicka, B. Fornal, G. F. Grinyer, N. Hoteling, B. P. Kay, T. Lauritsen, K. Minamisono, I. Stefanescu, J. B. Stoker, W. B. Walters, and S. Zhu, "β Decay and isomeric properties of neutron-rich Ca and Sc isotopes", Physical Review C **82**, 014311 (2010).

[36] D. Steppenbeck, S. Takeuchi, N. Aoi, P. Doornenbal, M. Matsushita, H. Wang, H. Baba, N. Fukuda, S. Go, M. Honma, J. Lee, K. Matsui, S. Michimasa, T. Motobayashi, D. Nishimura, T. Otsuka, H. Sakurai, Y. Shiga, P.-A. Söderström, T. Sumikama, H. Suzuki, R. Taniuchi, Y. Utsuno, J. J. Valiente-Dobón, and K. Yoneda, "Evidence for a new nuclear 'magic number' from the level structure of ^{54}Ca", Nature **502**, 207 (2013).

[37] T. Otsuka, T. Suzuki, R. Fujimoto, H. Grawe, and Y. Akaishi, "Evolution of Nuclear Shells due to the Tensor Force", Physical Review Letters **95**, 232502 (2005).

[38] T. Otsuka, T. Suzuki, J. D. Holt, A. Schwenk, and Y. Akaishi, "Three-body forces and the limit of oxygen isotopes", Physical Review Letters **105**, 14 (2010).

[39] G. Hagen, M. Hjorth-Jensen, G. R. Jansen, R. MacHleidt, and T. Papenbrock, "Continuum Effects and Three-Nucleon Forces in Neutron-Rich Oxygen Isotopes", Physical Review Letters **108**, 242501 (2012).

[40] G. Hagen, G. R. Jansen, R. Machleidt, and T. Papenbrock, "Evolution of Shell Structure in Neutron-Rich Calcium Isotopes", Physical Review Letters **032502**, 032502 (2012).

[41] J. D. Holt, J. Menéndez, J. Simonis, and A. Schwenk, "Three-nucleon forces and spectroscopy of neutron-rich calcium isotopes", Physical Review C **90**, 024312 (2014).

[42] J. D. Holt, T. Otsuka, A. Schwenk, and T. Suzuki, "Three-body forces and shell structure in calcium isotopes", Journal of Physics G: Nuclear and Particle Physics **39**, 85111 (2012).

[43] J. J. Thomson, "Bakerian Lecture: Rays of Positive Electricity", Proceedings of the Royal Society of London A: Mathematical, Physical and Engineering Sciences **89**, 1 (1913).

[44] M. Mukherjee, D. Beck, K. Blaum, G. Bollen, J. Dilling, S. George, F. Herfurth, A. Herlert, A. Kellerbauer, H. J. Kluge, S. Schwarz, L. Schweikhard, and C. Yazidjian, "ISOLTRAP: An on-line Penning trap for mass spectrometry on short-lived nuclides", European Physical Journal A **35**, 1 (2008).

[45] G. Bollen, S. Schwarz, D. Davies, P. Lofy, D. Morrissey, R. Ringle, P. Schury, T. Sun, and L. Weissman, "Beam cooling at the low-energy-beam and ion-trap facility at NSCL/MSU", Nuclear Instruments and Methods in Physics Research, Section A: Accelerators, Spectrometers, Detectors and Associated Equipment **532**, 203 (2004).

[46] V. S. Kolhinen, S. Kopecky, T. Eronen, U. Hager, J. Hakala, J. Huikari, A. Jokinen, A. Nieminen, S. Rinta-Antila, J. Szerypo, and J. Äystö, "JYFLTRAP: A cylindrical Penning trap for isobaric beam purification at IGISOL", Nuclear Instruments and Methods in Physics Research, Section A: Accelerators, Spectrometers, Detectors and Associated Equipment **528**, 776 (2004).

[47] G. Savard, J. C. Wang, K. S. Sharma, H. Sharma, J. A. Clark, C. Boudreau, F. Buchinger, J. E. Crawford, J. P. Greene, S. Gulick, A. A. Hecht, J. K. P. Lee, A. F. Levand, N. D. Scielzo, W. Trimble, J. Vaz, and B. J. Zabransky, "Studies of neutron-rich isotopes with the CPT mass spectrometer and the CARIBU project", International Journal of Mass Spectrometry **251**, 252 (2006).

[48] M. Block, D. Ackermann, K. Blaum, A. Chaudhuri, Z. Di, S. Eliseev, R. Ferrer, D. Habs, F. Herfurth, F. P. Heßberger, S. Hofmann, H. J. Kluge, G. Maero, A. Martín, G. Marx, M. Mazzocco, M. Mukherjee, J. B. Neumayr, W. R. Plaß, W. Quint, S. Rahaman, C. Rauth, D. Rodríguez, C. Scheidenberger, L. Schweikhard, P. G. Thirolf, G. Vorobjev, and C. Weber, "Towards direct mass measurements of nobelium at SHIPTRAP", European Physical Journal D **45**, 39 (2007).

[49] M. Brodeur, V. L. Ryjkov, T. Brunner, S. Ettenauer, A. T. Gallant, V. V. Simon, M. J. Smith, A. Lapierre, R. Ringle, P. Delheij, M. Good, D. Lunney, and J. Dilling, "Verifying the accuracy of the TITAN Penning-trap mass spectrometer", International Journal of Mass Spectrometry **310**, 20 (2012).

[50] B. Franzke, "The heavy ion storage and cooler ring project ESR at GSI", Nuclear Instruments and Methods in Physics Research Section B: Beam Interactions with Materials and Atoms **24-25**, 18 (1987).

[51] H. Savajols, "The SPEG Mass Measurement Program at GANIL", Hyperfine Interactions **132**, 245 (2001).

[52] M. Matoš, A. Estradé, H. Schatz, D. Bazin, M. Famiano, A. Gade, S. George, W. G. Lynch, Z. Meisel, M. Portillo, A. Rogers, D. Shapira, A. Stolz, M. Wallace, and J. Yurkon, "Time-of-flight mass measurements of exotic nuclei", Nuclear Instruments and Methods in Physics Research, Section A: Accelerators, Spectrometers, Detectors and Associated Equipment **696**, 171 (2012).

[53] H. S. Xu, Y. H. Zhang, and Y. A. Litvinov, "Accurate mass measurements of exotic nuclei with the CSRe in Lanzhou", International Journal of Mass Spectrometry **349-350**, 162 (2013).

[54] A. Ozawa, T. Uesaka, and M. Wakasugi, "The rare-RI ring", Progress of Theoretical and Experimental Physics **2012**, 03C009 (2012).

[55] R. N. Wolf, D. Beck, K. Blaum, C. Böhm, C. Borgmann, M. Breitenfeldt, F. Herfurth, A. Herlert, M. Kowalska, S. Kreim, D. Lunney, S. Naimi, D. Neidherr, M. Rosenbusch, L. Schweikhard, J. Stanja, F. Wienholtz, and K. Zuber, "On-line separation of short-lived nuclei by a multi-reflection time-of-flight device", Nuclear Instruments and Methods in Physics Research, Section A: Accelerators, Spectrometers, Detectors and Associated Equipment **686**, 82 (2012).

[56] W. R. Plaß, T. Dickel, and C. Scheidenberger, "Multiple-reflection time-of-flight mass spectrometry", International Journal of Mass Spectrometry **349-350**, 134 (2013).

[57] P. Schury, M. Wada, Y. Ito, F. Arai, S. Naimi, T. Sonoda, H. Wollnik, V. A. Shchepunov, C. Smorra, and C. Yuan, "A high-resolution multi-reflection time-of-flight mass spectrograph for precision mass measurements at RIKEN/SLOWRI", Nuclear Instruments and Methods in Physics Research, Section B: Beam Interactions with Materials and Atoms **335**, 39 (2014).

[58] K. Blaum, J. Dilling, and W. Nörtershäuser, "Precision atomic physics techniques for nuclear physics with radioactive beams", Physica Scripta **T152**, 14017 (2013).

[59] M. Smith, M. Brodeur, T. Brunner, S. Ettenauer, A. Lapierre, R. Ringle, V. L. Ryjkov, F. Ames, P. Bricault, G. W. F. Drake, P. Delheij, D. Lunney, F. Sarazin, and J. Dilling, "First penning-trap mass measurement of the exotic halo nucleus ^{11}Li", Physical Review Letters **101**, 202501 (2008).

[60] L. Chen, W. R. Plaß, H. Geissel, R. Knöbel, C. Kozhuharov, Y. A. Litvinov, Z. Patyk, C. Scheidenberger, K. Siegień-Iwaniuk, B. Sun, H. Weick, K. Beckert, P. Beller, F. Bosch, D. Boutin, L. Caceres, J. J. Carroll, D. M. Cullen, I. J. Cullen, B. Franzke, J. Gerl, M. Górska, G. A. Jones, A. Kishada, J. Kurcewicz, S. A. Litvinov, Z. Liu, S. Mandal, F. Montes, G. Münzenberg, F. Nolden, T. Ohtsubo, Z. Podolyák, R. Propri, S. Rigby, N. Saito, T. Saito, M. Shindo, M. Steck, P. M. Walker, S. Williams, M. Winkler, H. J. Wollersheim, and T. Yamaguchi, "New results on mass measurements of stored neutron-rich nuclides in the element range from Pt to U with the FRS-ESR facility at 360–400 MeV/u", Nuclear Physics A **882**, 71 (2012).

[61] B. Sun, R. Knöbel, Y. A. Litvinov, H. Geissel, J. Meng, K. Beckert, F. Bosch, D. Boutin, C. Brandau, L. Chen, I. J. Cullen, C. Dimopoulou, B. Fabian, M. Hausmann, C. Kozhuharov, S. A. Litvinov, M. Mazzocco, F. Montes, G. Münzenberg, A. Musumarra, S. Nakajima, C. Nociforo, F. Nolden, T. Ohtsubo, A. Ozawa, Z. Patyk, W. R. Plaß, C. Scheidenberger, M. Steck, T. Suzuki, P. M. Walker, H. Weick, N. Winckler, M. Winkler, and T. Yamaguchi, "Nuclear structure studies of short-lived neutron-rich nuclei with the novel large-scale isochronous mass spectrometry at the FRS-ESR facility", Nuclear Physics A **812**, 1 (2008).

[62] D. Lunney, J. M. Pearson, and C. Thibault, "Recent trends in the determination of nuclear masses", Reviews of Modern Physics **75**, 1021 (2003).

[63] J. M. Wouters, D. J. Vieira, H. Wollnik, G. W. Butler, R. H. Kraus, Jr., and K. Vaziri, "The Time-Of-Flight Isochronous (TOFI) spectrometer for direct mass measurements of exotic light nuclei", Nuclear Instruments and Methods in Physics Research Section B: Beam Interactions with Materials and Atoms **26**, 286 (1987).

[64] D. Lunney, G. Audi, H. Doubre, S. Henry, C. Monsanglant, M. de Saint Simon, C. Thibault, C. Toader, C. Borcea, and G. Bollen (ISOLDE Collaboration), "Precision mass measurements of very short-lived, neutron-rich Na isotopes using a radio-frequency spectrometer", Physical Review C **64**, 543111 (2001).

[65] G. Audi, M. Wang, A. Wapstra, F. Kondev, M. MacCormick, X. Xu, and B. Pfeiffer, "The AME2012 Atomic Mass Evaluation", Chinese Physics C **36**, 1287 (2012).

[66] Z. Meisel, S. George, S. Ahn, D. Bazin, B. A. Brown, J. Browne, J. F. Carpino, H. Chung, R. H. Cyburt, A. Estradé, M. Famiano, A. Gade, C. Langer, M. Matoš, W. Mittig, F. Montes, D. J. Morrissey, J. Pereira, H. Schatz, J. Schatz, M. Scott, D. Shapira, K. Sieja, K. Smith, J. Stevens, W. Tan, O. Tarasov, S. Towers, K. Wimmer, J. R. Winkelbauer, J. Yurkon, and R. G. T. Zegers, "Time-of-flight mass measurements of neutron-rich chromium isotopes up to $N = 40$ and implications for the accreted neutron star crust", Physical Review C **93**, 035805 (2016).

[67] Z. Meisel, S. George, S. Ahn, D. Bazin, B. A. Brown, J. Browne, J. F. Carpino, H. Chung, A. L. Cole, R. H. Cyburt, A. Estradé, M. Famiano, A. Gade, C. Langer, M. Matoš, W. Mittig, F. Montes, D. J. Morrissey, J. Pereira, H. Schatz, J. Schatz, M. Scott, D. Shapira, K. Smith, J. Stevens, W. Tan, O. Tarasov, S. Towers, K. Wimmer, J. R. Winkelbauer, J. Yurkon, and R. G. T. Zegers, "Mass Measurement of ^{56}Sc Reveals a Small $A = 56$

Odd-Even Staggering, Implying a Cooler Accreted Neutron Star Crust", Physical Review Letters **115**, 162501 (2015).

[68] Z. Meisel, S. George, S. Ahn, J. Browne, D. Bazin, B. A. Brown, J. F. Carpino, H. Chung, R. H. Cyburt, A. Estradé, M. Famiano, A. Gade, C. Langer, M. Mato, W. Mittig, F. Montes, D. J. Morrissey, J. Pereira, H. Schatz, J. Schatz, M. Scott, D. Shapira, K. Smith, J. Stevens, W. Tan, O. Tarasov, S. Towers, K. Wimmer, J. R. Winkelbauer, J. Yurkon, and R. G. T. Zegers, "Mass Measurements Demonstrate a Strong $N = 28$ Shell Gap in Argon", Physical Review Letters **022501**, 022501 (2015).

[69] B. Jurado, H. Savajols, W. Mittig, N. A. Orr, P. Roussel-Chomaz, D. Baiborodin, W. N. Catford, M. Chartier, C. E. Demonchy, Z. Dlouhý, A. Gillibert, L. Giot, A. Khouaja, A. Lépine-Szily, S. Lukyanov, J. Mrazek, Y. E. Penionzhkevich, S. Pita, M. Rousseau, and A. C. Villari, "Mass measurements of neutron-rich nuclei near the $N = 20$ and 28 shell closures", Physics Letters, Section B: Nuclear, Elementary Particle and High-Energy Physics **649**, 43 (2007).

[70] *National Nuclear Data Center*, `http://www.nndc.bnl.gov/`.

[71] Y. Yano, "The RIKEN RI Beam Factory Project: A status report", Nuclear Instruments and Methods in Physics Research, Section B: Beam Interactions with Materials and Atoms **261**, 1009 (2007).

[72] T. Uesaka, S. Shimoura, and H. Sakai, "The SHARAQ spectrometer", Progress of Theoretical and Experimental Physics **2012**, 03C007 (2012).

[73] H. Miya, S. Ota, T. Fujii, S. Kawase, Y. Kubota, C. S. Lee, H. Matsubara, K. Miki, A. Saito, S. Michimasa, T. Uesaka, H. Sakai, and S. Shimoura, "Development of low-pressure multi-wire drift chambers for high-resolution spectroscopy with radioactive isotope beams", Nuclear Instruments and Methods in Physics Research, Section B: Beam Interactions with Materials and Atoms **317**, 701 (2013).

[74] S. Michimasa, M. Takaki, M. Dozono, S. Go, H. Baba, E. Ideguchi, K. Kisamori, H. Matsubara, H. Miya, S. Ota, H. Sakai, S. Shimoura, A. Stolz, T. Tang, H. Tokieda, T. Uesaka, and R. G. T. Zegers, "Development of CVD diamond detector for time-of-flight measurements", Nuclear Instruments and Methods in Physics Research Section B: Beam Interactions with Materials and Atoms **317**, 710 (2013).

[75] T. Kubo, "In-flight RI beam separator BigRIPS at RIKEN and elsewhere in Japan", Nuclear Instruments and Methods in Physics Research, Section B: Beam Interactions with Materials and Atoms **204**, 97 (2003).

[76] S. Michimasa, M. Takaki, Y. Sasamoto, M. Dozono, T. Nishi, T. Kawabata, S. Ota, H. Baba, T. Baba, T. Fujii, S. Go, S. Kawase, Y. Kikuchi, K. Kisamori, M. Kobayashi, Y. Kubota, C. S. Lee, H. Matsubara, K. Miki, H. Miya, S. Noji, H. Tokieda, M. Tsumura, K. Yako, R. Yokoyama, H. Takeda, Y. Yanagisawa, T. Kubo, N. Inabe, N. Fukuda, D. Kameda, H. Suzuki, Y. Shimizu, H. Sato, T. Ichihara, A. Stolz, R. G. T. Zegers, H. Sakai, T. Uesaka, and S. Shimoura, "SHARAQ spectrometer for high-resolution studies

for RI-induced reactions", Nuclear Instruments and Methods in Physics Research Section B: Beam Interactions with Materials and Atoms **317**, 305 (2013).

[77] T. Kawabata, G. P. A. Berg, T. Kubo, H. Sakai, S. Shimoura, and T. Uesaka, "High resolution beam line for the SHARAQ spectrometer", Nuclear Instruments and Methods in Physics Research, Section B: Beam Interactions with Materials and Atoms **266**, 4201 (2008).

[78] K. Makino and M. Berz, "COSY INFINITY version 9", Nuclear Instruments and Methods in Physics Research, Section A: Accelerators, Spectrometers, Detectors and Associated Equipment **558**, 346 (2006).

[79] H. Kumagai, A. Ozawa, N. Fukuda, K. Sümmerer, and I. Tanihata, "Delay-line PPAC for high-energy light ions", Nuclear Instruments and Methods in Physics Research Section A: Accelerators, Spectrometers, Detectors and Associated Equipment **470**, 562 (2001).

[80] Y. Kiyokawa, "Isomer gamma-ray spectroscopy of neutron rich nuclei near $N = 40$", Master thesis, University of Tokyo (2016).

[81] H. Baba, T. Ichihara, T. Ohnishi, S. Takeuchi, K. Yoshida, Y. Watanabe, S. Ota, and S. Shimoura, "New data acquisition system for the RIKEN Radioactive Isotope Beam Factory", Nuclear Instruments and Methods in Physics Research, Section A: Accelerators, Spectrometers, Detectors and Associated Equipment **616**, 65 (2010).

[82] R. Grzywacz, R. Béraud, C. Borcea, A. Emsallem, M. Glogowski, H. Grawe, D. Guillemaud-Mueller, M. Hjorth-Jensen, M. Houry, M. Lewitowicz, A. Mueller, A. Nowak, A. Płochocki, M. Pfützner, K. Rykaczewski, M. Saint-Laurent, J. Sauvestre, M. Schaefer, O. Sorlin, J. Szerypo, W. Trinder, S. Viteritti, and J. Winfield, "New Island of μs Isomers in Neutron-Rich Nuclei around the $Z = 28$ and $N = 40$ Shell Closures", Physical Review Letters **81**, 766 (1998).

[83] S. N. Liddick, P. F. Mantica, R. Broda, B. A. Brown, M. P. Carpenter, A. D. Davies, B. Fornal, T. Glasmacher, D. E. Groh, M. Honma, M. Horoi, R. V. F. Janssens, T. Mizusaki, D. J. Morrissey, A. C. Morton, W. F. Mueller, T. Otsuka, J. Pavan, H. Schatz, A. Stolz, S. L. Tabor, B. E. Tomlin, and M. Wiedeking, "Development of shell closures at N=32,34. I. β decay of neutron-rich Sc isotopes", Physical Review C **70**, 064303 (2004).

[84] D. Kameda, T. Kubo, T. Ohnishi, K. Kusaka, A. Yoshida, K. Yoshida, M. Ohtake, N. Fukuda, H. Takeda, K. Tanaka, N. Inabe, Y. Yanagisawa, Y. Gono, H. Watanabe, H. Otsu, H. Baba, T. Ichihara, Y. Yamaguchi, M. Takechi, S. Nishimura, H. Ueno, A. Yoshimi, H. Sakurai, T. Motobayashi, T. Nakao, Y. Mizoi, M. Matsushita, K. Ieki, N. Kobayashi, K. Tanaka, Y. Kawada, N. Tanaka, S. Deguchi, Y. Satou, Y. Kondo, T. Nakamura, K. Yoshinaga, C. Ishii, H. Yoshii, Y. Miyashita, N. Uematsu, Y. Shiraki, T. Sumikama, J. Chiba, E. Ideguchi, A. Saito, T. Yamaguchi, I. Hachiuma, T. Suzuki, T. Moriguchi, A. Ozawa, T. Ohtsubo, M. A. Famiano, H. Geissel, A. S. Nettleton, O. B. Tarasov, D. Bazin, B. M. Sherrill, S. L. Manikonda, and J. A. Nolen, "Observation of new microsecond isomers among fission products from in-flight fission of 345 MeV/nucleon ^{238}U", Physical Review C **86**, 054319 (2012).

[85] W. R. Leo, *Techniques for Nuclear and Particle Physics Experiments: A How-to Approach* (Springer-Verlag, 1994).

[86] O. B. Tarasov and D. Bazin, "LISE++: Radioactive beam production with in-flight separators", Nuclear Instruments and Methods in Physics Research, Section B: Beam Interactions with Materials and Atoms **266**, 4657 (2008).

[87] A. K. Jain, B. Maheshwari, S. Garg, M. Patial, and B. Singh, "Atlas of Nuclear Isomers", Nuclear Data Sheets **128**, 1 (2015).

[88] Y. Kiyokawa, S. Michimasa, M. Kobayashi, R. Yokoyama, D. Nishimura, S. Ota, A. Mizukami, H. Oikawa, K. Kobayashi, H. Baba, G. P. A. Berg, M. Dozono, N. Fukuda, T. Furuno, E. Ideguchi, N. Inabe, T. Kawabata, S. Kawase, K. Kisamori, T. Kubo, Y. Kubota, C. S. Lee, M. Matsushita, H. Miya, H. Nagakura, H. Sakai, S. Shimoura, A. Stolz, H. Suzuki, M. Takaki, H. Takeda, S. Takeuchi, H. Tokieda, T. Uesaka, K. Yako, Y. Yamaguchi, Y. Yanagisawa, and K. Yoshida, "Isomer spectroscopy of neutron rich nuclei near $N = 40$", RIKEN Accelerator Progress Report **49** (to be published).

[89] X. Xu, M. Wang, Y.-H. Zhang, H.-S. Xu, P. Shuai, X.-L. Tu, Y. A. Litvinov, X.-H. Zhou, B.-H. Sun, Y.-J. Yuan, J.-W. Xia, J.-C. Yang, K. Blaum, R.-J. Chen, X.-C. Chen, C.-Y. Fu, Z. Ge, Z.-G. Hu, W.-J. Huang, D.-W. Liu, Y.-H. Lam, X.-W. Ma, R.-S. Mao, T. Uesaka, G.-Q. Xiao, Y.-M. Xing, T. Yamaguchi, Y. Yamaguchi, Q. Zeng, X.-L. Yan, H.-W. Zhao, T.-C. Zhao, W. Zhang, and W.-L. Zhan, "Direct mass measurements of neutron-rich ^{86}Kr projectile fragments and the persistence of neutron magic number N=32 in Sc isotopes", Chinese Physics C **39**, 104001 (2015).

[90] A. Poves, J. Sánchez-solano, E. Caurier, and F. Nowacki, "Shell model study of the isobaric chains $A = 50$, $A = 51$ and $A = 52$", Nuclear Physics A **694**, 157 (2001).

[91] N. Shimizu, *Private communication.*

[92] Y. Utsuno, T. Otsuka, B. A. Brown, M. Honma, T. Mizusaki, and N. Shimizu, "Tensor-force-driven Jahn-Teller effect and shape transitions in exotic Si isotopes", Physical Review C **86**, 051301 (2012).

[93] H.-W. Hammer, A. Nogga, and A. Schwenk, "Colloquium: Three-body forces: From cold atoms to nuclei", Reviews of Modern Physics **85**, 197 (2013).

[94] K. Tsukiyama, S. K. Bogner, and A. Schwenk, "In-medium similarity renormalization group for nuclei", Physical Review Letters **106**, 222502 (2011).

[95] H. Hergert, S. K. Bogner, S. Binder, A. Calci, J. Langhammer, R. Roth, and A. Schwenk, "In-medium similarity renormalization group with chiral two-plus three-nucleon interactions", Physical Review C **87**, 034307 (2013).

[96] S. R. Stroberg, A. Calci, H. Hergert, J. D. Holt, S. K. Bogner, R. Roth, and A. Schwenk, "A nucleus-dependent valence-space approach to nuclear structure", arXiv:1607.03229 **[nucl-th]** (2016).

[97] J. D. Holt, *Private communication.*

[98] W. Satuła, J. Dobaczewski, and W. Nazarewicz, "Odd-Even Staggering of Nuclear Masses: Pairing or Shape Effect?", Physical Review Letters **81**, 3599 (1998).

[99] J. Dobaczewski, P. Magierski, W. Nazarewicz, W. Satuła, and Z. Szymański, "Odd-even staggering of binding energies as a consequence of pairing and mean-field effects", Physical Review C **63**, 024308 (2001).

[100] B. Alex Brown, "Nuclear pairing gap: How low can it go?", Physical Review Letters **111**, 162502 (2013).

[101] Y. Utsuno, T. Otsuka, Y. Tsunoda, N. Shimizu, M. Honma, T. Togashi, and T. Mizusaki, "Recent Advances in Shell Evolution with Shell-Model Calculations", JPS Conference Proceedings **6**, 010007 (2015).

[102] B. Blank, M. Chartier, S. Czajkowski, J. Giovinazzo, M. S. Pravikoff, J.-C. Thomas, G. de France, F. de Oliveira Santos, M. Lewitowicz, C. Borcea, R. Grzywacz, Z. Janas, and M. Pfützner, "Discovery of Doubly Magic ^{48}Ni", Physical Review Letters **84**, 1116 (2000).

[103] P. R. Bevington and D. K. Ronbinson, *Data Reduction and Error Analysis* (McGraw-Hill, 2003).

Acknowledgments

First of all, I would like to express my sincere gratitude to my supervisor Prof. Susumu Shimoura for his continuous encouragement and lots of precious advice based on his profound insights into physics during the course of the study. I am really impressed by his attitude toward research.

I am deeply grateful to Dr. Shin'ichiro Michimasa, who supervised me the most during my Ph.D study. His profound understanding of physics and data analysis guided me at all stages of this study. He has always encouraged me to move forward with my research. Without his support, I could not complete this work.

I would like to express my appreciation to Mr. Yu Kiyokawa, with whom I performed the data analysis. His dedicated contribution to the γ-ray detector array is quite remarkable. Discussion with him reminded me what I overlooked and deepened my understanding.

This experiment was performed by the SHARAQ03 collaboration. Many thanks to all the SHARAQ03 collaborators: Dr. Shin'ichiro Michimasa, Mr. Yu Kiyokawa, Dr. Masanori Dozono, Dr. Shoichiro Kawase, Dr. Keiichi Kisamori, Dr. Yuki Kubota, Mr. CheongSoo Lee, Dr. Masafumi Matsushita, Mr. Hiroyuki Miya, Dr. Shinsuke Ota, Prof. Susumu Shimoura, Mr. Motonobu Takaki, Mr. Hiroshi Tokieda, Prof. Kentaro Yako, Dr. Rin Yokoyama (*Center for Nuclear Study, University of Tokyo*), Dr. Hidetada Baba, Dr. Naoki Fukuda, Mr. Naohito Inabe, Prof. Toshiyuki Kubo, Dr. Hideyuki Sakai, Dr. Hiroshi Suzuki, Dr. Hiroyuki Takeda, Dr. Satoshi Takeuchi, Dr. Tomohiro Uesaka, Dr. Yoshiyuki Yanagisawa, Dr. Koichi Yoshida (*RIKEN Nishina Center*), Prof. Georg P. A. Berg (*University of Notre Dame*), Mr. Tatsuya Furuno, Prof. Takahiro Kawabata (*Kyoto University*), Prof. Eiji Ideguchi (*Research Center for Nuclear Physics, Osaka University*), Mr. Kazuma Kobayashi, Mr. Hiroyasu Nagakura, Mr. Yuki Yamaguchi (*Rikkyo University*), Mr. Atsushi Mizukami, Dr. Daiki Nishimura, Mr. Hiroyuki Oikawa (*Tokyo University of Science*), and Prof. Andreas Stolz (*National Superconducting Cyclotron Laboratory, Michigan State University*). Without any work of the collaborators, I could not accomplish the experiment. Special thanks go to Prof. Georg P. A. Berg for his kind help to brush up this thesis. I would also like to express gratitude to the cyclotron staff members of the RIKEN Nishina Center for their operation of the accelerators during the experiment.

I am also indebted to all the members of the NUSPEQ (NUclear SPectroscopy for Extreme Quantum system) group in CNS: Prof. Susumu Shimoura, Dr. Shin'ichiro Michimasa, Dr. Masafumi Matsushita, Mr. Hiroyuki Miya, Dr. Keiichi Kisamori, Mr. Motonobu Takaki, Dr. Rin Yokoyama, Mr. Kazuma Kobayashi, Mr. Shoichiro Masuoka, Mr. Yuki Yamaguchi, Mr. Ryo Nakajima, Mr. Kosuke Maeba, and Mr. Ryunosuke Bannai. Discussion during the weekly meeting helped me understand better not only my research but also nuclear physics

itself. Besides research activities, eating and drinking with them were always very fun.

I wish to thank Prof. Noritaka Shimizu, Dr. Jason D. Holt, and Dr. Javier Menéndez for providing me with the results of the state-of-the-art theoretical calculations and many fruitful discussions.

I am thankful to Dr. Rin Yokoyama, Mr. Shoichiro Masuoka, Mr. Noritaka Kitamura, Mr. Keita Kawata, and Mr. Yuki Yamaguchi for being so friendly. While the daily conversation with them was stupid in many cases, it was indispensable to perform the research without any stress.

I express my thanks to my room-mates Dr. Yosuke Watanabe and Dr. Yoki Aramaki. I enjoyed daily discussion and conversation with them, and learned a lot of things from them.

I would like to express my gratitude to Prof. Hiroyoshi Sakurai, who is my second supervisor in the Advanced Leading Graduate Course for Photon Science (ALPS). He kindly took time for discussion with me while he was very busy, and gave me valuable comments on my research based on his wealth of experience.

I appreciate all the supports by the CNS secretaries, Mr. Mikio Oki, Mr. Hiroshi Yoshimura, Ms. Ikuko Yamamoto, Ms. Takako Endo, Ms. Yukino Kishi, and Ms. Yuko Soma. I wish to express my special thanks to all the members of CNS for creating a pleasant working atmosphere. I have really enjoyed the daily life in CNS.

I am obliged to the referees of the present thesis, Prof. Kyoichiro Ozawa, Prof. Takaharu Otsuka, Prof. Masashi Yokoyama, Prof. Nobuaki Imai, and Prof. Hidetoshi Yamaguchi for their helpful comments to improve this thesis.

I would like to thank all my friends. Finally, I would like to express my deepest gratitude to my family, especially my parents, for their continuous support and encouragement.

December, 2016
Motoki Kobayashi